PROBABILISTIC ASSESSMENT OF NON-DUCTILE REINFORCED CONCRETE FRAMES SUSCEPTIBLE TO MID-AMERICA GROUND MOTIONS

A Dissertation
Presented to
The Academic Faculty

By

Ozan Cem Celik

In Partial Fulfillment
Of the Requirements for the Degree
Doctor of Philosophy in the
School of Civil and Environmental Engineering

Georgia Institute of Technology

August 2007

PROBABILISTIC ASSESSMENT OF NON-DUCTILE REINFORCED CONCRETE FRAMES SUSCEPTIBLE TO MID-AMERICA GROUND MOTIONS

Approved by:

Dr. Bruce R. Ellingwood, Advisor
School of Civil and Environmental
Engineering
Georgia Institute of Technology

Dr. Reginald DesRoches
School of Civil and Environmental
Engineering
Georgia Institute of Technology

Dr. Steven P. French
School of City and Regional Planning
Georgia Institute of Technology

Dr. Glenn J. Rix
School of Civil and Environmental
Engineering
Georgia Institute of Technology

Dr. Abdul-Hamid Zureick
School of Civil and Environmental
Engineering
Georgia Institute of Technology

Date Approved: May 21, 2007

To my parents

ACKNOWLEDGEMENTS

made my life in Atlanta enjoyable and friends elsewhere in the world who have always

supported me.

TABLE OF CONTENTS

LIST OF TABLES

LIST OF FIGURES

SUMMARY

The infrequent nature of earthquakes in the Central and Eastern United States (CEUS), and the fact that none with intensity comparable to the New Madrid sequence of 1811–12 or the Charleston earthquake of 1886 has occurred in the past century, have caused the earthquake hazard in the region to be ignored until quite recently. The seismic performance of reinforced concrete (RC) frames in the CEUS, which have primarily been designed for gravity load effects, is expected to be deficient when subjected to earthquakes that are judged, in recent seismological research, as being plausible in the New Madrid Seismic Zone (NMSZ). The objective of this study is to develop a set of probability-based tools for efficient uncertainty analysis and seismic vulnerability and risk assessment of such gravity load designed (GLD) RC frames and to use these tools in evaluating the seismic vulnerability of RC frames that are representative of the building inventory in Memphis, TN — the largest population center close to the NMSZ.

Synthetic earthquake ground motions for the CEUS that are available from two different Mid-America Earthquake (MAE) Center projects were used in the finite element-based simulations for determining the seismic demand on the GLD RC frames by nonlinear time history analysis (NTHA). A beam-column joint model was developed to address the deficiencies in the joints of GLD frames and was incorporated in the finite element structural models. Seismic fragilities were derived for low-, mid-, and high-rise GLD RC frames. Various sources of uncertainty were propagated through the analysis, and their significance for fragility assessment was examined. These fragilities were used to evaluate the vulnerability of the RC frame inventory in Memphis, TN with regard to

performance-based design objectives, defined in terms of performance levels associated with reference earthquake hazard levels. This performance appraisal indicated that GLD RC frames do not meet the life safety and collapse prevention performance objectives that are found in recent building codes and guidelines for performance-based earthquake engineering.

CHAPTER 1

INTRODUCTION

1.1 Background

Earthquakes are paramount among the natural hazards impacting civil infrastructure worldwide. The direct economic losses (property losses) incurred in recent earthquakes were $7 billion in the 1989 Loma Prieta, $30 billion in the 1994 Northridge, and $200 billion in the 1995 Kobe earthquakes [Bertero and Bertero, 2002]. Such large losses, which are far greater when social impacts and indirect economic losses are considered, have prompted an interest in performance assessment of the built environment to future seismic events. Performance evaluations of buildings and other structures at multiple levels, beyond the traditional goal of life safety, are required to estimate expected losses. These evaluations require improved building performance and seismic risk assessment tools. Such tools would serve decision- and policy-makers not only in pre-earthquake planning to mitigate probable losses but also in post-earthquake planning to develop emergency response and recovery strategies.

Seismic vulnerability and risk assessment of buildings and other structures requires characterization of earthquake hazard, usually by a suite of appropriate ground motions, determination of structural response (structural demand), identification of performance limits (structural capacity), and degrees of structural damage and losses associated with specific damage states [Wen *et al.*, 2004]. A key ingredient of this evaluation process is the *fragility*, a term that describes the probability of failure to meet a performance objective as a function of demand on the system. The seismic fragility plays

a central role in a fully coupled seismic risk analysis in that it provides the link between seismic hazard and building loss estimation.

Seismic fragility modeling of buildings, bridges, and other civil infrastructure in regions of high seismicity in the Western United States (WUS) has matured significantly during the past decade, due to research conducted in the SAC[a] project under the Federal Emergency Management Agency (FEMA) sponsorship [FEMA 350, 2000a; Cornell *et al.*, 2002] and in the Pacific Earthquake Engineering Research (PEER) Center [*e.g.*, Singhal and Kiremidjian, 1996; Shinozuka *et al.*, 2000]. In contrast, the notions of building fragility and vulnerability assessment are not well established in the Central and Eastern U.S. (CEUS). Current research under the sponsorship of the Mid-America Earthquake (MAE) Center is aimed at assessing vulnerability of building and bridge construction typical to that region [Wen *et al.*, 2003; 2004; Wen and Ellingwood, 2005] as part of the consequence-based risk management (CBRM) paradigm [Abrams, 2002].

Among the issues that distinguish fragility assessment in the CEUS from the WUS, two stand out. First, earthquakes with the capability of damaging buildings are rare in most areas in the CEUS. As a result, the earthquake hazard has not been appreciated and most jurisdictions have not adopted earthquake-resistant design practices or codes until quite recently, if at all. Hence, the potential for severe damage to buildings in the CEUS is greater. Second, there are few natural ground motion records available for the CEUS, due to the infrequent nature of earthquakes, and there are none that correspond to the large earthquakes, such as the New Madrid sequence of 1811–12, that are believed to threaten modern civil infrastructure or construction in the region. Accordingly, seismic

---

[a] SAC is a joint venture of the Structural Engineers Association of California (SEAOC), the Applied Technology Council (ATC), and California Universities for Research in Earthquake Engineering (CUREe).

2

vulnerability and risk assessment of buildings in the CEUS must rely on synthetic earthquake ground motions.

This study focuses on the behavior of reinforced concrete (RC) frames in the CEUS, which have been designed for gravity load (or gravity plus wind load) effects, when subjected to earthquakes that are judged, in recent seismological research, as being plausible in the New Madrid Seismic Zone (NMSZ). Such gravity load designed (GLD) RC frames have limited lateral load resistance and are susceptible to column-sidesway or soft-story mechanisms under earthquake effects. The extent of the inventory of vulnerable RC frames in the CEUS necessitates the seismic risk assessment of such frames to prioritize risk mitigation efforts and develop post-earthquake response and recovery strategies for communities in this area of the country.

The Memphis Test Bed project, which is being conducted in the MAE Center, is using Memphis, TN, as a study region for illustrating the application of the CBRM to a typical at-risk region in the CEUS. The MAE Center concurrently is developing a software platform, MAEviz, aimed at assessing the vulnerability of the built environment in Mid-America to a future New Madrid-intensity earthquake and estimating economic losses and social impact were such an event to occur. Among its advantages, MAEviz will propagate all sources of uncertainty in the various components of seismic risk modeling to enable decision- and policy-makers to develop risk reduction and mitigation strategies that are consistent with the seismic hazard in the CEUS and the resources available to address that hazard.

1.2 Objectives and Scope

The goals of this study are to develop a set of probability-based tools for efficient uncertainty analysis and seismic vulnerability and risk assessment of GLD RC frames that are susceptible to Mid-America ground motions and to use these tools in evaluating the seismic vulnerability of RC frames that are representative of the building inventory in Memphis, TN — the largest population center close to the NMSZ in the CEUS. The following critical steps are necessary to achieve these goals:

(1) Identify the possible sources of poor behavior in GLD RC frames when they are subjected to earthquake effects.

(2) Develop mechanics-based models to simulate the behavior of GLD frames and validate the models using experimental data.

(3) Identify sets of synthetic earthquake ground motions that are plausible for CEUS sites at risk.

(4) Identify sample GLD RC frames that represent the inventory of such frames in the CEUS.

(5) Develop finite element structural models of the sample GLD frames that incorporate the above mechanics-based models.

(6) Identify a performance- or consequence-based framework that propagates uncertainties involved in the seismic risk assessment process.

(7) Identify appropriate interface measures that provide the flow of information between the different disciplines involved in the risk assessment.

(8) Develop seismic fragilities of the sample GLD RC frames and evaluate the vulnerability of such frames at various levels of earthquake hazard in the CEUS.

(9) Investigate the sensitivity of the seismic fragilities to the uncertainties in various material and structural properties and modeling parameters, and develop confidence bounds on the fragility estimates.

The RC frame inventory in the CEUS will be represented by GLD RC frames that are of different heights but have the same number of bays. Finite element structural models of the frames will not consider three-dimensional effects, the presence of infill walls, the contributions of non-structural components to seismic response, or soil-structure interaction.

1.3 Thesis Outline

This chapter has presented the context of the research that will be addressed in the chapters that follow.

Chapter 2 reviews the previous research on the seismic performance evaluation of GLD RC frames and related research in the areas of seismic vulnerability and risk assessment.

Chapter 3 describes the earthquake hazard in the CEUS, and displays the synthetic earthquake ground motions that were generated for the CEUS and are used in subsequent fragility analyses in later chapters.

Chapter 4 describes sample GLD RC frames that are believed to represent the inventory of such low-, mid-, and high-rise frames in the CEUS, and explains the finite element structural modeling of those frames that is later utilized in fragility analyses.

Chapter 5 lays out a performance- or consequence-based framework for seismic risk assessment and provides the fragility formulation adopted in this study.

Chapter 6 develops a beam-column joint model that addresses the deficiencies in the joints of GLD RC frames identified in Chapter 2 and is suitable for incorporation in the finite element models of the GLD frames. That model is validated through experimental data.

Chapter 7 derives the seismic fragilities for GLD RC frames and assesses their seismic vulnerability.

Chapter 8 examines the sensitivity of the fragilities to various uncertainties and develops confidence bounds on the fragilities.

Finally, Chapter 9 presents a summary of the research, major conclusions drawn from this study, and future research ideas.

CHAPTER 2

CRITICAL APPRAISAL OF CURRENT STATE OF THE ART

2.1 Introduction

This chapter summarizes and critically appraises previous experimental and analytical studies that address the seismic performance of RC frames that were designed without consideration of earthquake effects, as well as related previous research in the areas of seismic vulnerability and risk assessment.

2.2 Seismic Performance Evaluation of GLD RC Frames

RC frame structures in the CEUS traditionally have been designed using detailing provisions of ACI[a] Standard 318, *Building code requirements for reinforced/structural concrete*, for the gravity load combination $1.4DL + 1.7LL$[b], with little or no consideration of seismic resistance [Hoffmann *et al.*, 1992]. In the event of an earthquake in this region, the seismic performance of such GLD RC frames is expected to be deficient because of reinforcing details that are typical in this type of construction. In one study, Beres *et al.* [1992] reviewed detailing manuals (ACI 315) and design codes (ACI 318) from the past five decades. Based on this review and consultation with practicing structural engineers, the following problematic reinforcing details that are typical in GLD RC frames were identified:

(1) Little or no transverse shear reinforcement is provided within the beam-column joints.

---

[a] American Concrete Institute.
[b] *DL* and *LL* respectively stand for dead and live loads.

(2) Bottom reinforcement in the beams is terminated within the beam-column joints with a short embedment length.

(3) Columns have bending moment capacities that are close to or less than those of the joining beams, promoting column-sidesway or soft-story mechanisms.

(4) The longitudinal reinforcement ratio in columns is seldom more than 2%.

(5) There is minimal transverse reinforcement in columns to provide shear resistance and confinement.

(6) Lightly confined lapped splices of column reinforcement often are placed in potential plastic hinge zones just above the floor levels.

(7) Construction joints are placed immediately below and above the beam-column joints.

Extensive research programs were undertaken at Cornell University and the State University of New York at Buffalo (SUNY at Buffalo) in the early 1990s to examine the impact of these deficiencies on the seismic response of GLD RC frames. Experimental studies at member or component scales under reversed cyclic loading and at system scales under seismic excitation were carried out and supplemented by analytical studies. Thirty-four full-scale interior and exterior beam-column joints, a two-story one-bay 1/6-scale frame, and a three-story three-bay 1/8-scale frame were tested at Cornell University [Pessiki *et al.*, 1990; Beres *et al.*, 1992; 1996; El-Attar *et al.*, 1997]. Similarly, four columns, two 1/3-scale slab-beam-column subassemblages, and a three-story three-bay 1/3-scale frame were tested at SUNY at Buffalo [Aycardi *et al.*, 1992; 1994; Bracci *et al.*, 1992a; 1992b; 1995]. Finite element models that were calibrated to the test data provided by these experimental studies were utilized to investigate the probable seismic

performance of GLD RC frames and to examine the effects of improving some of the non-ductile reinforcing details listed above on the seismic performance of such frames [Hoffmann *et al.*, 1992; Kunnath *et al.*, 1995a; 1995b]. Both research programs found that despite their flexibility, GLD RC frames possess some inherent seismic strength. However, structural performance of such frames is questionable in case of a major earthquake. The findings of these research programs are discussed in detail in the following.

Full-scale beam-column joint tests conducted at Cornell University [Pessiki *et al.*, 1990; Beres *et al.*, 1992; 1996] revealed that the damage occurred mainly in the joint panel region. For those tests of the interior joints, which were typical of strong column-weak beam specimens, the failure was initiated by the pullout of the insufficiently developed beam bottom reinforcement, accompanied by joint shear cracking and column damage close to the joint panel. It was reported that the pullout of the beam bottom bars reduced the positive beam moment capacities to 50–70% of their nominal values. In other tests where the specimens were designed as weak column-strong beam in order to study the column splice behavior and where continuous beam bottom bars were provided, the interior joints either failed in joint shear or experienced heavy damage. Significant damage was also observed in the columns. Lapped splices of column reinforcement performed adequately, and no failure was associated with the failure of a column splice. Providing joint reinforcement when continuous beam bottom bars were present improved the performance of the interior joints and caused failure to occur by column bar buckling rather than joint shear. When sufficient joint reinforcement was provided, the interior joint sustained its peak resistance with continued cycling to larger drifts. The failure in

the exterior joints occurred mainly by excessive diagonal shear cracking due to the high joint shear, pullout of the beam bottom bar being less important than in the tests of the interior joints. Experimental load-deformation plots indicated highly pinched hysteretic behavior for both interior and exterior beam-column joints. The deficient behavior observed in the tests was not associated with the construction joints.

Component tests conducted at SUNY at Buffalo [Aycardi *et al.*, 1992; 1994] provided further input for designing the shake table tests of GLD RC frames that were performed later. The failure of the column specimens was flexure-dominated; hence, the transverse shear reinforcement provided was sufficient to resist the imposed shear demand. The exterior slab-beam-column subassemblage was reported to experience a strong column-weak beam failure mechanism, as the damage was initiated in the beams with the pullout of the beam bottom bars. However, the columns reached their capacities and were damaged when the loading was reversed, which indicates weak column-strong beam behavior. The interior slab-beam-column subassemblage, on the other hand, developed a weak column-strong beam failure mechanism, with no damage in the beam. Joint shear distortion was observed in the tests of both assemblages. The exterior assemblage suffered joint damage at only large drifts due to the presence of some joint reinforcement, while the interior assemblage experienced significant joint shear deformations.

Shake table tests on reduced-scale frame models conducted at Cornell University [El-Attar *et al.*, 1997] showed that GLD RC frames, typically with weak column-strong beam designs, are susceptible to soft-story collapses under earthquake effects. Such frames are also highly flexible, which may result in significant P-Δ effects that can lead

to collapse or excessive damage to building contents. Both two- and three-story frames showed first-mode dominant behavior when responding to a sequence of 1952 Taft earthquake ground motions that were scaled to increasingly higher peak ground accelerations (PGAs). The three-story 1/8-scale frame experienced top story drifts exceeding 2% when the PGA was 0.18 g and nearly 3% when the PGA was 0.35 g. The collapse of the frame occurred when plastic hinges developed at both ends of the first story columns and formed a soft-story failure mechanism when the Taft ground motion was scaled to a PGA beyond 0.35 g. No significant damage was observed in the beams, joint panels, or column splice regions, indicating that weak column-strong beam behavior leads to premature soft-story mechanisms before the other problematic reinforcing details are subjected to significant demands. Analytical studies that supplement the experimental findings revealed that accounting for slab contribution to the flexural strength of the beams is necessary in assessing the seismic performance of GLD RC frames as that otherwise may lead to strong column-weak beam interpretation of the frame behavior.

Shake table tests on GLD RC frames continued with the test of a three-story 1/3-scale frame model at SUNY at Buffalo [Bracci *et al.*, 1992a; 1992b; 1995]. This model was tested under a sequence of strong motions that are representative of earthquakes that can cause minor, moderate, and severe structural damage, respectively. The analysis of the frame response to the initial white noise excitation yielded a viscous damping of 2% for the first mode of vibration. Under minor shaking (1952 Taft earthquake ground motion scaled to a PGA of 0.05 g — a different component than in El-Attar *et al.* [1997]), the 1/3-scale frame remained primarily elastic with slight cracking in the columns. Moderate and severe shaking (Taft accelerograms with PGAs of 0.20 g and 0.30 g)

caused the interstory drift demands to exceed 1% and 2%, respectively, at both the first two stories of the frame. Significant damage occurred in the columns, while the beams only experienced slight damage. Hence, the overall frame behavior was dominated by the weak column-strong beam behavior. When subjected to severe shaking, the 1/3-scale frame developed an identical pattern of plastic hinges as the 1/8-scale frame, and a similar soft-story collapse was anticipated; although collapse did not occur at 0.30 g, most of the first two story columns had reached their capacities by the time that the excitation ended. No damage was observed in the interior beams and beam-column joints. However, reinforcement bond-slip was observed at the first story exterior beams. Significant slab steel contribution to the flexural strength of the beams was noted.

Hoffmann *et al.* [1992] and Kunnath *et al.* [1995a] studied the seismic performance of typical GLD RC frames using finite element simulations, with hysteretic parameters calibrated to the above test data. Non-ductile reinforcing details such as the insufficiently developed beam bottom bars and the lack of joint shear reinforcement were modeled implicitly with simplifying assumptions, which are subsequently discussed in Chapter 6. The confined concrete model that was incorporated in the finite element models takes into account the inadequate confinement of the concrete core in the columns. Inelastic dynamic time history analyses of three-, six-, and nine-story frames revealed that GLD RC frames would sustain repairable damage under moderate earthquakes, while irreparable damage or collapse would occur if the frames were exposed to severe earthquakes (simulated by 1940 El Centro and 1952 Taft earthquake ground motions scaled to PGAs of 0.20 g). The Taft accelerogram imposed the highest demand on the frames, with interstory drifts exceeding 3% and 4% in the three- and six-

story frames, respectively, and with drifts about 2% for the nine-story frame. It was concluded that GLD RC frames are vulnerable to damage from joint shear failures and weak column-strong beam effects leading to soft-story collapses.

Hoffmann *et al.* [1992] and Kunnath *et al.* [1995b] later studied the effects of improving the non-ductile reinforcing details identified above in the finite element models. None of the detailing enhancements they considered led to any appreciable improvement in the seismic performance of the three-story frame. On the other hand, the following observations were made for the six- and nine-story frames. First, the provision of continuity or sufficient anchorage to the beam bottom bars shifted the damage from beams to columns and, in combination with increased joint failures, resulted in increased drifts and soft-story effects. Hence, this enhancement, if utilized alone, was detrimental. Second, the provision of sufficient joint shear capacity altered the failure mechanism from a combination of beam and column hinging to a favorable beam-sidesway mechanism. However, drift demand was reduced marginally. Finally, additional confinement to the beams and columns, independent of other enhancements, did not affect the overall frame behavior. Implementing the detailing enhancements together reduced the drift demand and caused formation of an essentially beam-sidesway mechanism with some column hinging at upper stories. However, weak column-strong beam effects present at upper stories may still jeopardize the seismic performance of the GLD frames.

2.3 Seismic Vulnerability and Risk Assessment

Seismic vulnerability and risk assessment procedures can be classified into two groups depending on whether their derivation is based on post-earthquake surveys or analytical simulations.

Post-earthquake survey-based procedures rely theoretically on the most reliable data source — damage data from earthquakes. In a number of such procedures [*e.g.*, Gulkan and Sozen, 1999; Yucemen *et al.*, 2004], some basic structural information (*e.g.*, number of stories, structural system), material properties (*e.g.*, *in-situ* concrete strength), apparent structural deficiencies (*e.g.*, vertical and plan irregularities), and building site location were collected with damage data through a post-earthquake survey. This information was utilized to arrive at a rating score or index in which the numerical value usually determines whether the building is safe or unsafe, with respect to the traditional goal of assuring life safety. Other procedures [*e.g.*, Shinozuka *et al.*, 2000; Rossetto and Elnashai, 2003] utilized the collected information for developing seismic assessment tools in the form of fragility curves.

These observation-based or empirical procedures are highly specific to a particular seismo-tectonic, geotechnical, and built environment [Rossetto and Elnashai, 2003]. Application of these procedures to regions other than those for which they were developed often does not yield satisfactory damage estimates when seismic characteristics and building infrastructure differ. Consequently, they have found limited use only in highly seismic regions, where they have been used to rank seismic vulnerability of buildings. In contrast, more recent seismic vulnerability and risk assessment procedures require multiple performance evaluations within a performance-

or consequence-based framework, which may only be feasible with simulation-based analytical procedures.

Before the resources for intensive analytical simulations required for the derivation of fragility curves were available, expert opinion had been the substitute for analytical simulations. The ATC relied on expert opinion with limited observational data from the 1971 San Fernando earthquake when preparing the ATC-13 report [ATC, 1985], which is one of the first applications of fragility modeling to civil infrastructure subjected to earthquake demand. The reliability of the fragilities in ATC-13, which were identified in terms of damage state probability matrices, is questionable in that the fragilities are subjective and the associated degree of conservatism is unknown [Rossetto and Elnashai, 2003].

The well-known loss estimation software package, HAZUS, developed under the sponsorship of FEMA [2003a], is also based on expert opinion to a considerable degree. HAZUS incorporates fragilities for 36 categories of building and 4 damage states, where the fragilities are modeled by lognormal distributions with the distribution parameters based primarily on expert opinion.

HAZUS was developed to serve as a decision tool for estimating earthquake losses from a possible future seismic activity and for mitigating such losses on a regional basis for the U.S. [Whitman *et al.*, 1997]. The loss estimation methodology classifies the buildings in terms of building type on the basis of their height and structural system (*e.g.*, mid-rise RC moment frame) and seismic design level on the basis of the seismic standard used in their design, the seismic zones in which they are built, their design vintage, and their use (*e.g.*, low code) [Kircher *et al.*, 1997a]. Based on this classification, building

capacity is represented by a nonlinear static pushover (NSP) curve in the form of base shear versus roof displacement, and building response to an input scenario earthquake, considering the local site conditions, is determined with the capacity spectrum method [Freeman, 1998]. The building response is then entered into the associated built-in fragility curves defined at the thresholds of four discrete damage states (slight, moderate, extensive, and complete), defined separately for the structural system and for drift- and acceleration-sensitive non-structural components, to perform the loss estimation calculations given the occupancy class of the building (*e.g.*, residential, commercial) [Kircher *et al.*, 1997b]. Whitman *et al.* [1997] observed that the losses estimated using HAZUS should be viewed with caution since they may be off by a factor of two, or even more in the CEUS. Some other limitations were noted by Erberik and Elnashai [2003]. Perhaps most significant, HAZUS does not provide for the analysis or propagation of uncertainty. The outcomes are the mean values and the user cannot assess the confidence in the damage prediction without performing a lengthy sensitivity analysis that would involve re-running HAZUS a large number of times to capture the variations in the input parameters.

More recent approaches have relied on analytical simulations. The relation between structural response and earthquake ground motion intensity, which is the basic ingredient for deriving the fragility curves, is established through analytical simulations with varying comprehensiveness. Differences also exist in characterization of earthquake hazard, structural damage, performance limits, *etc.*

Singhal and Kiremidjian [1996] developed fragility curves for low-, mid-, and high-rise RC frames that were designed using seismic provisions. The uncertainty in

16

structural capacity and demand was taken into account through Monte Carlo simulations. Stochastically generated frame models randomly paired with simulated ground motion records were used in the nonlinear time history analyses (NTHAs). Structural demand versus seismic intensity relationships were determined from so-called stripe analyses, as illustrated in Figure 2.1. The structural demand at each seismic intensity level was assessed using ground motions scaled to that particular intensity level and was represented by a lognormal probability density function ($LN(\lambda, \zeta)$), in which $\exp(\lambda)$ is the median and ζ is the logarithmic standard deviation. The lognormal model of demand was then utilized to compute fragility estimates (for the performance limits considered) at that particular level. Finally, fragility curves were represented by lognormal cumulative distribution functions that were fit to individual fragility estimates, computed at several seismic intensity levels. The comparison of the fragilities with those in ATC-13 revealed that ATC-13 is rather unrealistic in that it predicts negligible probabilities of severe damage or collapse under a large earthquake such as the 1994 Northridge earthquake. Singhal and Kiremidjian [1998] later presented a Bayesian method for updating the fragility curves that they developed earlier for low-rise RC frames and estimating confidence bounds on those fragility curves, by using the observed building damage data from the 1994 Northridge earthquake. Differences do exist between the earlier and the updated fragility estimates.
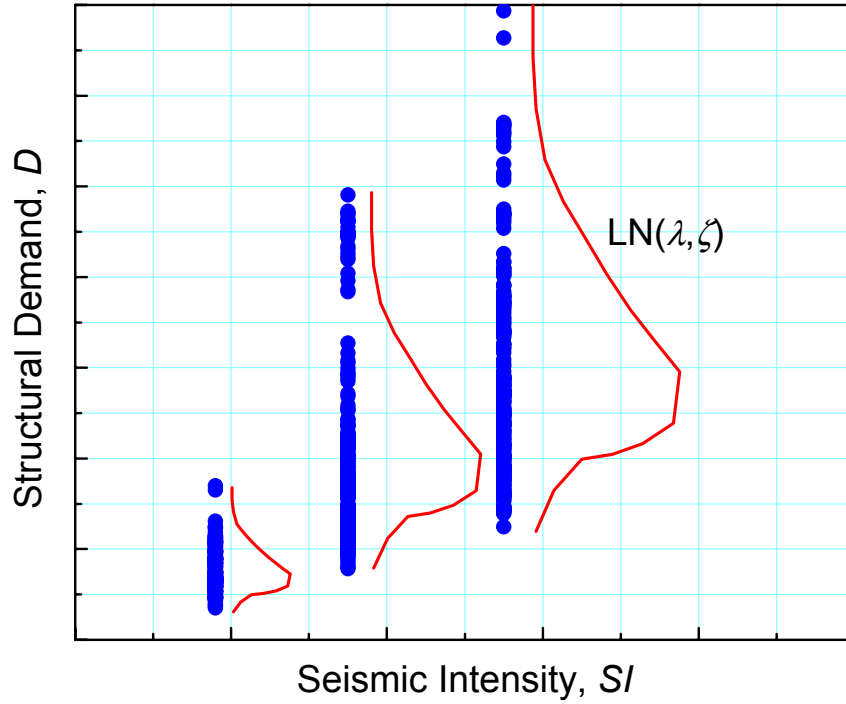
Figure 2.1 Stripe analyses.

Mosalam *et al.* [1997] developed fragility curves for low-rise GLD RC frames with and without masonry infill walls. Single-degree-of-freedom (SDOF) models were employed in the NTHAs. These models were obtained from the adaptive NSP analyses of the frame models, which were generated using Monte Carlo simulations to take into account the uncertainty in structural material properties. The structural responses of these SDOF models to each ground motion (*i.e.*, each model was paired with each ground motion rather than randomly as in Singhal and Kiremidjian [1996]) were used to determine the fragility estimates (for the performance limits considered) for that particular ground motion. Fragility curves that were then fit to individual estimates for two different ensembles of synthetic ground motions showed a dependency on the choice of the ensemble particularly for the bare frame. The comparison of the fragilities with

those of ATC-13 revealed significantly larger differences for the lower performance levels.

Shinozuka *et al.* [2000] developed both empirical and analytical fragility curves for bridges. The empirical fragility curves utilized the observed bridge damage data from the 1995 Kobe earthquake. In contrast, the analytical fragility curves utilized such data that were simulated from the NTHAs of stochastically generated models of two typical bridges in Memphis, TN, taking into account the uncertainty in structural material properties. Both fragility curves were represented by lognormal distribution functions with the distribution parameters estimated using the maximum likelihood method. Confidence intervals for the distribution parameters were also provided.

Porter *et al.* [2001] proposed an assembly-based vulnerability framework for assessing the seismic vulnerability of buildings on a building-specific basis. The proposed approach differs from the above analytical procedures in that "a vulnerability function" that relates the seismic losses to the seismic intensity was developed for a particular building and the damage to individual assemblies was determined for this purpose. The seismic losses were assessed using stripe analyses. The structural response to each scaled ground motion was entered into assembly fragility curves, and the associated damage to each structural and non-structural element in the building and to its contents was determined as outlined in the study. The total damage was then expressed in terms of the sum of repair and loss-of-use costs as a fraction of replacement cost. After performing a regression analysis on the generated data, the seismic vulnerability function was obtained for a particular building. The application of the proposed framework to a

$$\hat{D} = a \cdot SI^b \cdot \varepsilon$$
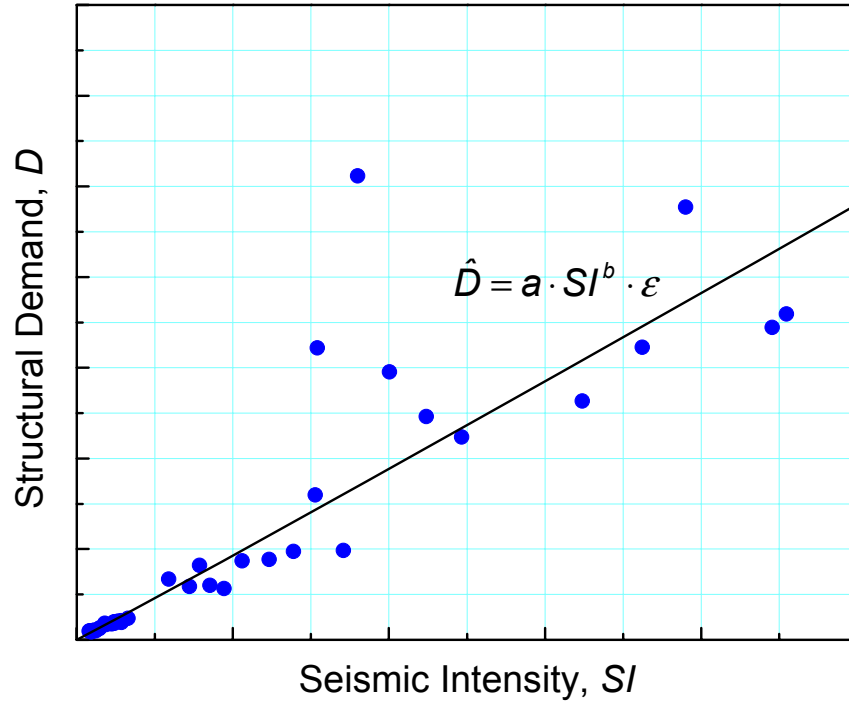
Figure 2.2 Cloud analysis.

steel moment frame building revealed that substantial uncertainty exists in the vulnerability function derived for the building.

Cornell *et al.* [2002] developed a probabilistic framework for seismic design and assessment of structures in a demand and capacity format, addressing the uncertainties in hazard, structural, damage, and loss analyses. Structural demand versus seismic intensity relationships were determined from a so-called cloud analysis, as illustrated in Figure 2.2. The structural demand was assessed using a suite of ground motions and the median structural demand was represented by a log-linear function of seismic intensity. The structural demand was assumed to be distributed lognormally about the median with constant logarithmic standard deviation. This framework provided the probabilistic basis for the design recommendations that resulted from the SAC project.

Other researchers developed simulation-based analytical fragility curves for RC buildings in recent years. Erberik and Elnashai [2004] used the same methodology as in Singhal and Kiremidjian [1996] for deriving fragility curves for mid-rise flat-slab RC buildings with masonry infill walls. However, they paired each stochastically generated building model with each ground motion record considered in the study rather than randomly matching the models with the ground motions. Performance limits for which the fragility curves were developed were identified from the NSP analysis of the building. The comparison of fragilities with those for moment frames that also have masonry infill walls revealed that the flat-slab RC buildings are more vulnerable to seismic damage than the moment-resisting RC frames.

Rossetto and Elnashai [2005] developed fragility curves for low-rise RC frames with masonry infill walls that were designed according to the seismic design code in place in Italy in 1982. Structural demand versus seismic intensity relationships were determined using the same methodology as in Erberik and Elnashai [2004] but the capacity spectrum method with adaptive NSP analysis was employed, reducing the required computational time compared to NTHAs. A response surface equation was fit to the demand versus intensity data. Fragility curves were then developed using a larger data set at refined seismic intensity levels, which was generated through a re-sampling process from the response surface equation. Confidence bounds were also identified on the fragility curves. The comparison of fragilities with the discrete fragility estimates obtained from the observational damage data in Rossetto and Elnashai [2003] revealed that the simulation-based fragility estimates in this study are conservative.

Kwon and Elnashai [2006] developed fragility curves for low-rise GLD RC frames but the problematic reinforcing details associated with such frames, such as the inadequate joint shear capacity and the insufficient positive beam bar anchorage, were not considered. The finite element model of the three-story GLD RC frame was validated using experimental data from the shake table tests of the 1/3-scale replica of the frame [Bracci *et al.*, 1992a; 1992b]. However, the behavior of this model might be significantly different from that of the actual frame due to the reduced scale. The fragility curve derivation methodology followed that in Erberik and Elnashai [2004] with full combination of the randomly generated material strength parameters in the generated frame models, which resulted in a biased sample set. The analysis of structural demand statistics indicated that the effect of material uncertainty is negligible with respect to that of ground motion uncertainty. Furthermore, the comparison of fragility curves that were developed using different sets of ground motions revealed a dependency on the choice of the ensemble as in Mosalam *et al.* [1997].

In a recent study, Ramamoorthy *et al.* [2006] also developed fragility curves for low-rise GLD RC frames. The finite element model of the two-story GLD RC frame was similar to those calibrated to the tests at SUNY at Buffalo [Bracci *et al.*, 1992b; 1995]. The structural demand was assessed using a cloud analysis based on NTHAs and the median demand was represented by a bilinear function rather than a linear function in Cornell *et al.* [2002], with the regression parameters estimated from a Bayesian methodology presented in the study. The fragility curves were utilized to show the effectiveness of the seismic retrofitting scheme adopted in the study in the form of column strengthening.

2.4 Summary

The structural deficiencies of GLD RC frames built in the CEUS are reasonably well known. Experimental studies point to the first four of the problematic reinforcing details listed earlier in this chapter as significant in making GLD RC frames vulnerable to seismic demands. Appropriate modeling of such non-ductile reinforcing details is required to get accurate estimates of seismic performance from the finite element simulations of GLD RC frames. As part of the structural modeling process, a beam-column joint model will be developed that addresses the shear and bond-slip in the joints of GLD RC frames. This model will be incorporated in the finite element models of GLD RC frames in subsequent seismic fragility analyses.

Research on seismic fragility modeling of civil infrastructure to date has focused mainly on high seismic areas in the WUS. However, the seismic risk in the CEUS, where construction practices differ, may be substantial. The above review has revealed that none of the existing studies of GLD RC frames in the CEUS have:

(1) identified the impact of the differences in frequency content of the ground motions on the finite element structural responses and seismic fragility estimates;

(2) used state-of-the-art finite element platforms that incorporate rigorous modeling of deficient behavior associated with non-ductile reinforcing details in GLD RC frames in the CEUS;

(3) developed fragility estimates with systematic treatment of uncertainties in addition to that in ground motion; or

(4) assessed the seismic vulnerability of GLD RC frames with respect to multiple performance-based design objectives.

Simulation-based probabilistic tools are clearly required for reliable seismic vulnerability and risk assessment in the CEUS, given the infrequent nature of earthquakes in the region. Hence, this study will develop probabilistic assessment tools for GLD RC frames in the CEUS, using state-of-the-art finite element models within a framework that propagates all sources of uncertainty, as required by the CBRM paradigm of the MAE Center. In the following chapters, these research issues will be addressed in further detail.

CHAPTER 3

SYNTHETIC EARTHQUAKE GROUND MOTIONS FOR THE

CENTRAL AND EASTERN UNITED STATES

3.1 Introduction

Characterization of the earthquake hazard is a fundamental step in seismic vulnerability and risk assessment of buildings and other structures. In a simulation-based fragility assessment, the seismic demand on a building is determined using ground motion time histories that reflect the earthquake hazard in the region of interest. In the absence of natural strong motion records in the CEUS, synthetic earthquake ground motions must be utilized for this purpose.

3.2 Earthquake Hazard in the CEUS

The highest seismicity in the U.S. occurs along the boundary of the Pacific tectonic plate in the WUS (see Figure 3.1). In the last four decades, four major earthquakes causing substantial damage have struck the WUS: the 1971 San Fernando (M 6.6), the 1989 Loma Prieta (M 6.9), the 1994 Northridge (M 6.7), and the 2001 Nisqually earthquakes (M 6.8).[a] Such large earthquakes have not occurred recently in the CEUS but have occurred in the past. Two of the three large earthquakes with magnitudes 7.8–8.1 that occurred in the New Madrid area in 1811–12 top the list of the largest earthquakes in the conterminous U.S. (see Table 3.1); that list also includes the magnitude 7.3 Charleston, South Carolina earthquake in 1886 [USGS, 2007].

---

[a] M in parentheses denotes the moment magnitude.
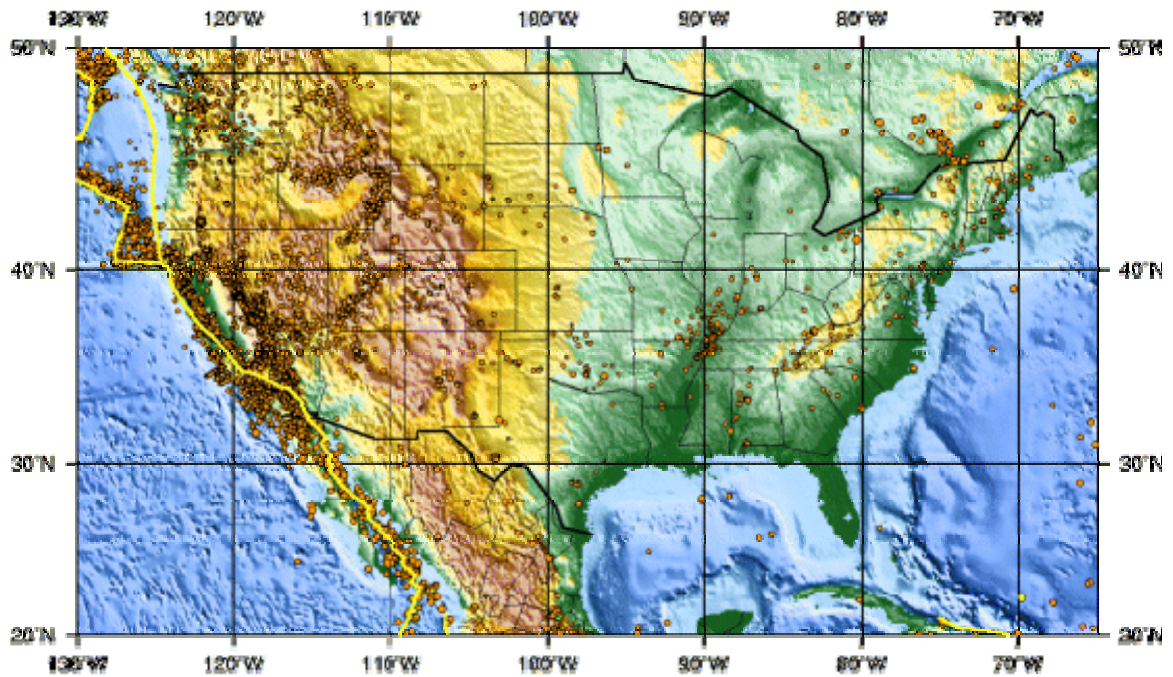
Figure 3.1 Seismicity in the U.S. (1990-2000) [USGS, 2007].

Table 3.1 Largest earthquakes in the conterminous U.S. [USGS, 2007].

Date	Location	Magnitude
1811 12 16	New Madrid, Missouri	8.1
1812 02 07	New Madrid, Missouri	≈8
1857 01 09	Fort Tejon, California	7.9
1812 01 23	New Madrid, Missouri	7.8
1892 02 24	Imperial Valley, California	7.8
1906 04 18	San Francisco, California	7.8
1872 03 26	Owens Valley, California	7.4
1872 12 15	N Cascades, Washington	7.3
1873 11 23	California-Oregon Coast	7.3
1886 09 01	Charleston, South Carolina	7.3
1952 07 21	Kern County, California	7.3
1959 08 18	Hebgen Lake, Montana	7.3
1992 06 28	Landers, California	7.3

Characteristics of the earthquakes in the CEUS differ significantly from those in the WUS. The CEUS earthquakes are intraplate earthquakes, occurring within stable continental regions, while the WUS earthquakes are interplate earthquakes, occurring at tectonic boundaries. The recurrence intervals of intraplate earthquakes are much larger than those of interplate earthquakes. The strain energy sufficient to trigger a fault rupture takes much longer to accumulate within a stable continental crust than along the boundaries of tectonic plates. Hence, significant Mid-America earthquakes are infrequent when compared to those in the WUS. Historical evidence suggests that major earthquakes (magnitude 7 or greater) such as the 1811–12 New Madrid sequence recur approximately every 500 years in the NMSZ [U.S. Geological Survey (USGS), 2002a]. Furthermore, the strong and stable nature of plate interiors is much more efficient in propagating the seismic waves than the weak zones of near plate boundaries. Hence, a Mid-America earthquake affects a much wider area than an earthquake of similar magnitude in the WUS. This is illustrated in Figure 3.2, where the attenuation characteristic of the 1895 Charleston, Missouri earthquake of magnitude 6.6 is compared with that of the 1994 Northridge earthquake of magnitude 6.7 [USGS, 2003]. Moreover, in certain earthquake-prone regions, including the region affected by the NMSZ, the thick sediments result in amplified ground shaking intensity at the surface that is many times larger than at the bed rock [USGS, 2002a].

Of several zones believed capable of generating great earthquakes, the NMSZ is believed to represent the major threat of future seismic events in Mid-America [Wen and Wu, 2001], as illustrated in the seismic hazard map of the U.S. in Figure 3.3 [USGS, 2002b]. This map depicts the seismic hazard in terms of spectral acceleration (S_a) with
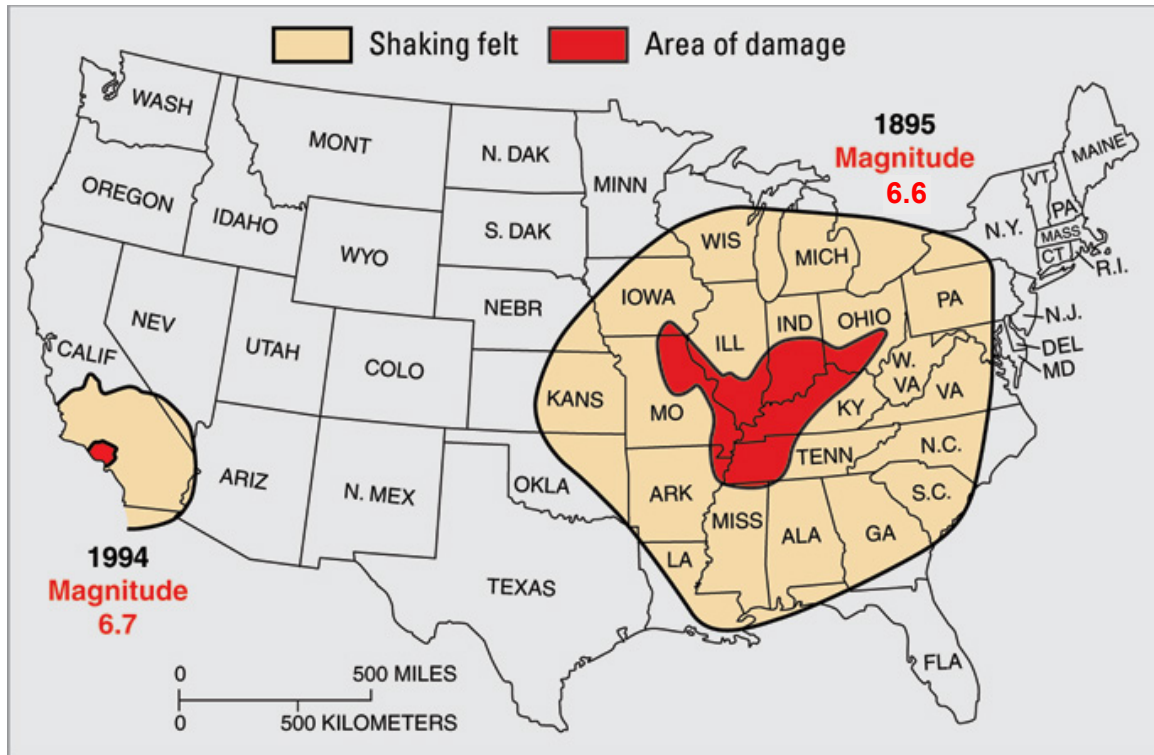
Figure 3.2 Attenuation characteristics of CEUS and WUS earthquakes [USGS, 2003].

2% probability of exceedance in 50 years (abbreviated 2% PE in 50 yr in the following) for a 5% damped oscillator that has a period of 1.0 s. The USGS currently maps the seismic hazard in terms of PGA and S_a at periods including 0.2 s, 0.3 s, and 1.0 s at several hazard levels that include 10%, 5%, and 2% PE in 50 yr, which respectively correspond to mean recurrence intervals of 475, 975, and 2,475 years. Figure 3.3 shows that the long-term seismic hazard in certain regions of the CEUS approaches that of the WUS. In the CEUS, the probability of an earthquake with comparable magnitude to the 1811–12 New Madrid sequence (in the range 7.5–8.0) within the next 50 years has been estimated as 7–10%, while the probability of an earthquake of magnitude 6.0 or larger has been estimated as 25–40% [USGS, 2002a].
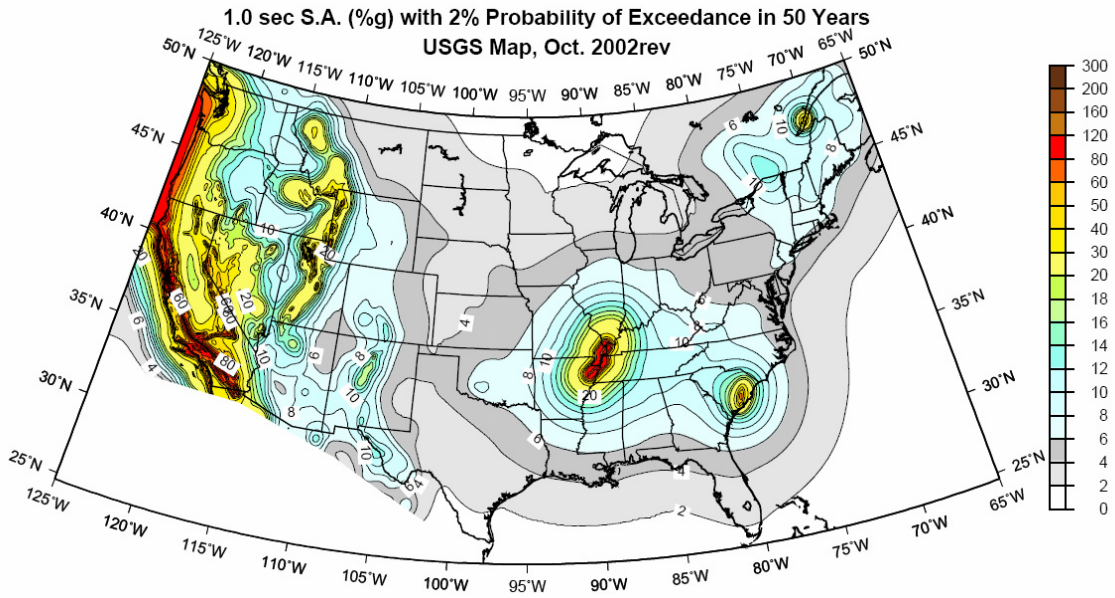
Figure 3.3 Seismic hazard map of the U.S. [USGS, 2002b].

3.3 Earthquake Ground Motions for Fragility Assessment

Strong motion records from sites in the CEUS of engineering interest are practically non-existent due to the infrequent nature of the earthquakes in the region, as discussed above. In particular, there are no records of low-probability high-consequence earthquakes, such as the 1811–12 New Madrid sequence. Hence, there is no clear association between seismicity and known tectonic structures. Accordingly, the ground motion ensembles used in this study are based on simulations from source and attenuation models using established procedures [*e.g.*, Boore, 2003], propagating the sources of uncertainty in the simulation process.

Synthetic uniform hazard ground motions (UHGM) for the CEUS are available from two different MAE Center studies. In the first, Wen and Wu [2001] generated synthetic ground motions for the cities of Memphis, TN; Carbondale, IL; and St. Louis, MO, which represent a cross-section of the earthquake-prone Mid-America cities. In the

29

second, Rix and Fernandez [2006] generated synthetic ground motions for seven such Mid-America cities, including Memphis, TN. These are denoted Wen-Wu and Rix-Fernandez ground motions, respectively, in the analyses that follow.[b]

The Rix-Fernandez ground motions were developed for hazard levels of 10%, 5%, and 2% PE in 50 yr for soil sites in the Upper Mississippi Embayment. The Wen-Wu ground motions were developed for hazard levels of 10% and 2% PE in 50 yr for both hard rock and representative soil[c] sites. For each hazard level, ensembles of 10 ground motions were generated, which subsequently will be used in the NTHAs of the GLD RC frames.

The procedures used in generating the UHGM in the above studies differ slightly. Wen and Wu [2001] simulated 90,000 years of records from the source and attenuation models according to the regional seismicity. Once the lognormal probability distributions for spectral accelerations at particular periods were determined, the spectral acceleration values corresponding to the above mentioned probabilities at those periods were used to construct the uniform hazard response spectra (UHRS) for those probability levels. Figure 3.4 illustrates this procedure. Ten ground motion records that best fit each of the UHRS in a least-squares sense were then selected to form the corresponding UHGM ensemble.

In contrast, Rix and Fernandez [2006] first simulated the UHRS for the above hazard levels, from the seismic source models and the soil attenuation relationships that they previously developed for the region [Fernandez and Rix, 2006]. Each of these mean UHRS and their standard deviations were then used to simulate 1,000 UHRS; 10 ground

---

[b] The Wen-Wu and Rix-Fernandez ground motions were synthesized at every 0.01 s and 0.005 s, respectively.
[c] Representative soil is roughly equivalent to Site Class C or D [FEMA 273, 1997a], depending on location.

30
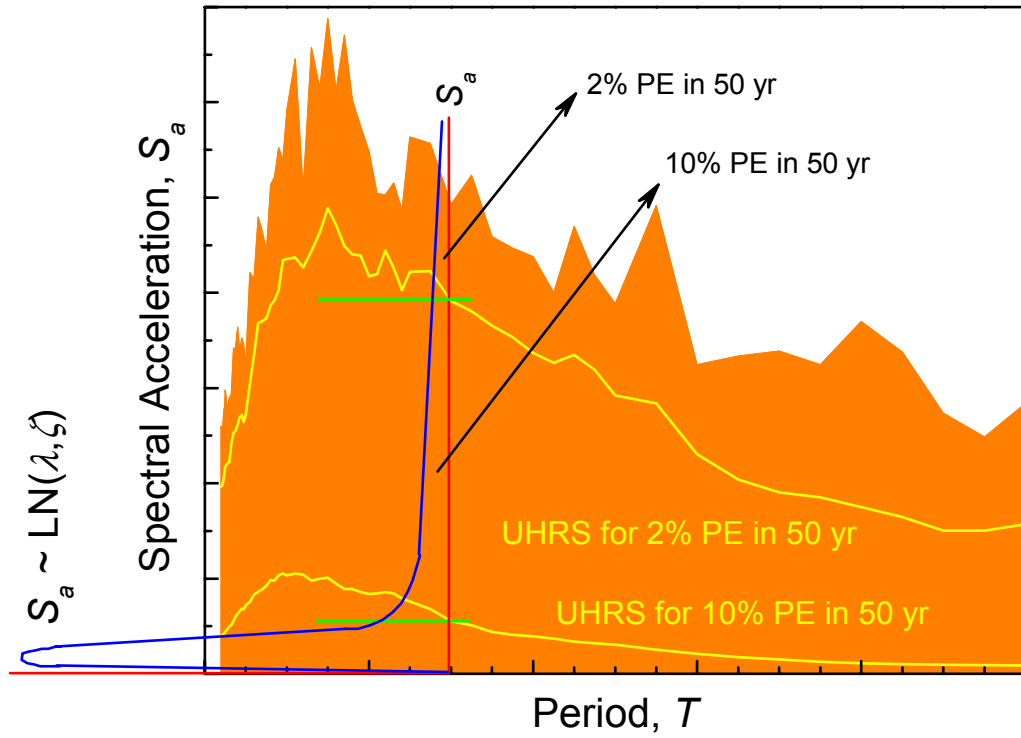
Figure 3.4 UHRS simulation procedure.

motion records then were generated using spectral matching to the randomly selected 10 UHRS, to form the UHGM ensemble for each hazard level.

For the NTHAs, the Wen-Wu ground motions were truncated after their 99.5% Arias intensities [Arias, 1970] were achieved to extract the significant portions of the records for computational efficiency, similar to the process that Rix and Fernandez used to develop their ground motions. Figure 3.5 illustrates this process for the Wen-Wu accelerogram #2 from the 2% PE in 50 yr soil ensemble.
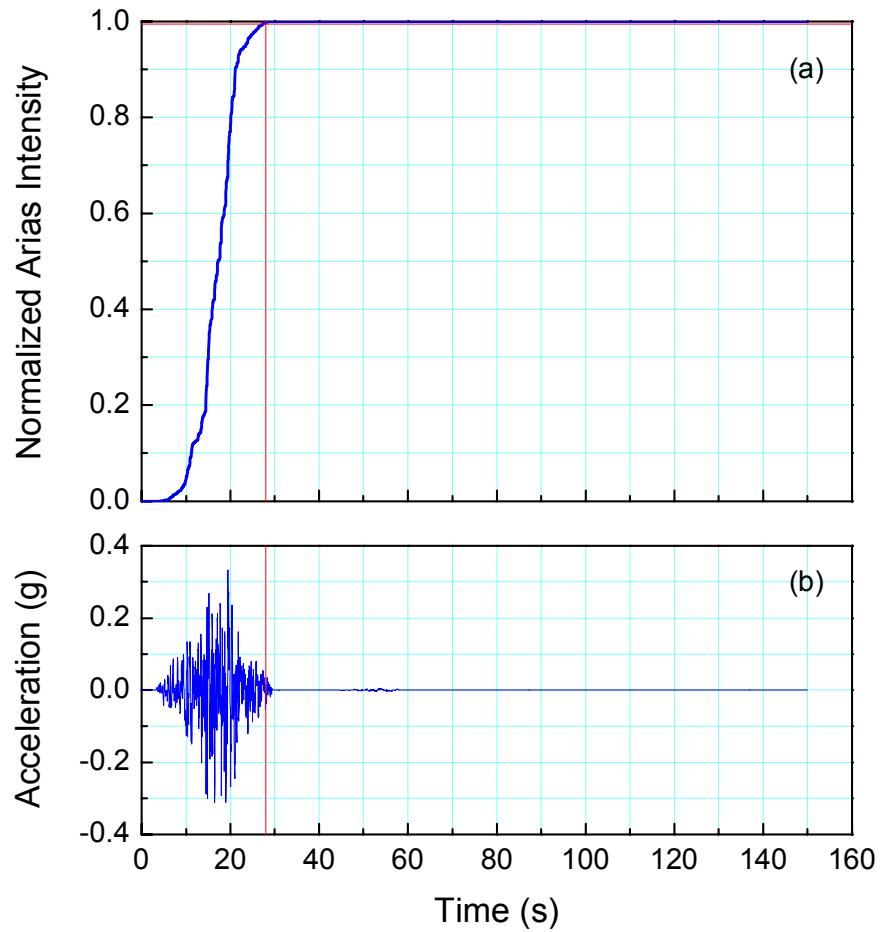
Figure 3.5 (a) Normalized Arias intensity of (b) the Wen-Wu accelerogram #2 from the 2% PE in 50 yr soil ensemble.
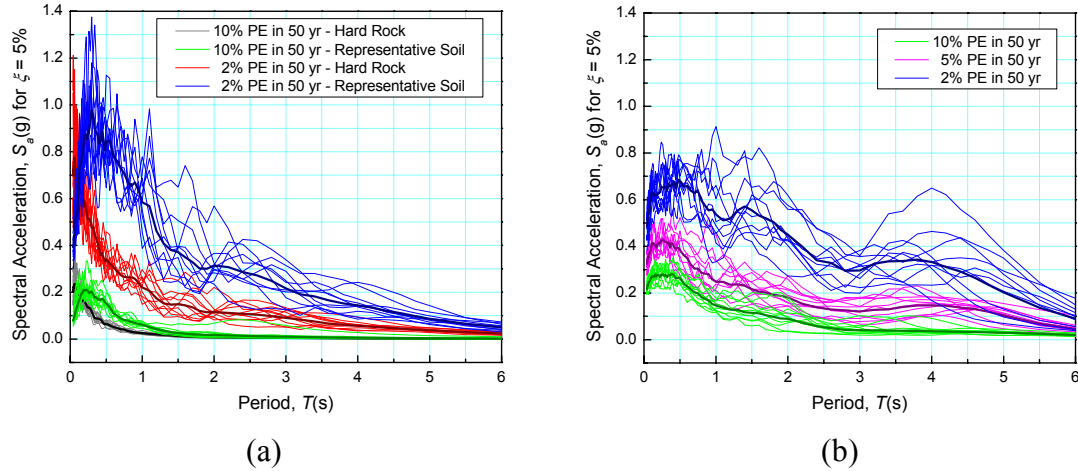
Figure 3.6 Individual and median response spectra of the UHGM for Memphis, TN: (a) Wen-Wu and (b) Rix-Fernandez (Uplands profile).

Figure 3.6 shows the elastic 5% damped response spectra (spectral accelerations) for the individual synthetic records, and the median response spectrum for each ensemble, that were generated for Memphis, TN. The inherent randomness (aleatoric uncertainty, as defined in Chapter 5) in seismic demand is characterized by the variability in the response spectra represented for each ensemble. The differences in spectral acceleration amplitudes of 10% and 2% PE in 50 yr ensembles between the Wen-Wu and Rix-Fernandez soil motions illustrate one source of knowledge-based uncertainty (defined as epistemic uncertainty in Chapter 5) in ground motion modeling. The medians for the Rix-Fernandez ensemble are larger than those for the corresponding Wen-Wu ensemble throughout the entire range of periods for 10% PE in 50 yr, and are larger for the 2% PE in 50 yr ensemble for periods longer than about 1.2 s. Such differences between the ground motion ensembles originate from differences in seismic source modeling and local site processes.

The Wen-Wu ground motions were simulated from the Atkinson and Boore [1995] point source model. In contrast, the Rix-Fernandez ground motions were
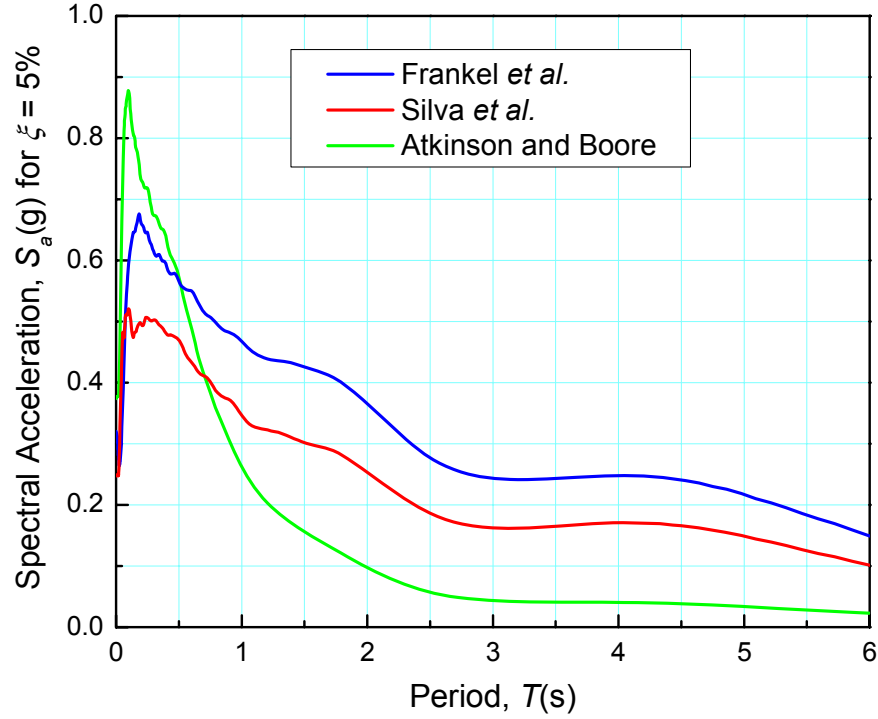
Figure 3.7 Soil attenuation relationships.

simulated from a weighted average of three alternative source models: Atkinson and Boore [1995], Frankel *et al.* [1996], and Silva *et al.* [2003]. Figure 3.7 depicts the soil attenuation relationships [Fernandez and Rix, 2006] for a magnitude 7.5 earthquake occurring at a distance 40 km (25 miles) away from the site; it can be seen that the Frankel *et al.* and Silva *et al.* models predict higher amplitude motions than the Atkinson and Boore model for periods longer than 0.5 s and 0.7 s, respectively.

Nonlinear soil behavior (*i.e.*, damping) was included in site response and resonances in the soil column were captured in simulating the Rix-Fernandez ground motions. On the other hand, the site response in the Wen-Wu ground motions was modeled by the quarter wavelength method, which overestimates the ground motion intensity at low periods when effects of soil nonlinearity are significant and misses the
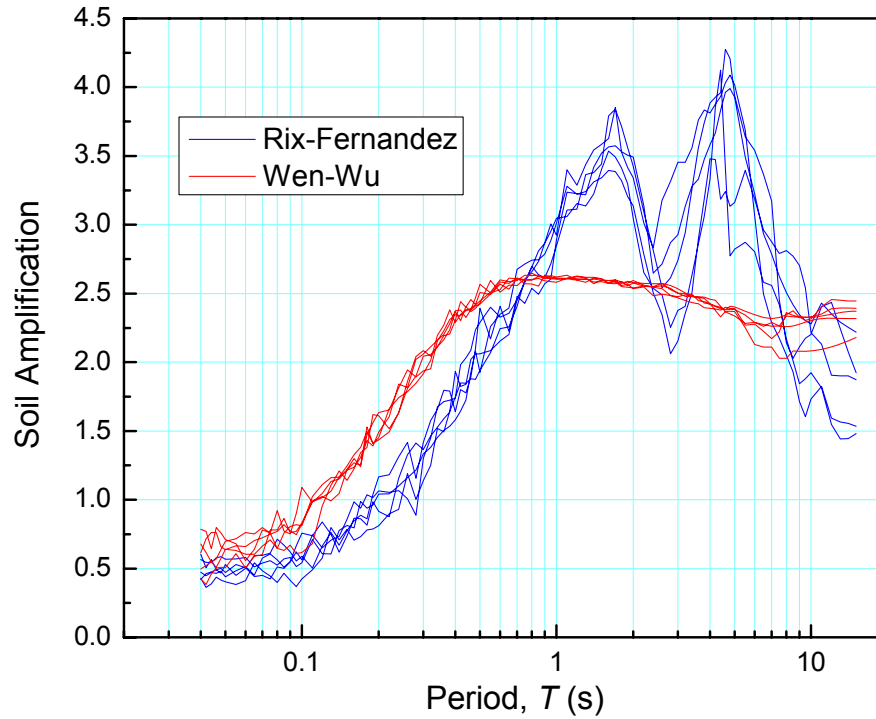
Figure 3.8 Typical soil amplification plots.

resonances in the soil column at higher periods [Wen and Wu, 2001]. These differences are illustrated in the comparison of typical soil amplification plots for the Rix-Fernandez and Wen-Wu ground motions in Figure 3.8.

The use of the above synthetic ground motion ensembles introduces a source of epistemic (modeling) uncertainty to the risk assessment. There are several alternative models for generating synthetic ground motions in Mid-America, each of which is believed plausible in the seismological community. The impact of the choice of the model on seismic fragility will be considered subsequently in Chapter 7.

3.4 Summary

Mid-America is a region of moderate seismicity, where large earthquakes have occurred infrequently in the past. However, strong motion records of such earthquakes are not

available. Hence, seismic vulnerability and risk assessment of buildings and other structures in the CEUS must rely on synthetic ground motions developed for the region. Ensembles of such synthetic UHGM from two MAE Center studies were presented and the sources of differences that might affect the subsequent seismic fragility analyses of GLD RC frames were identified.

CHAPTER 4

BUILDING INVENTORY IN THE CENTRAL AND EASTERN

UNITED STATES

4.1 Introduction

Seismic risk assessment of a building inventory in a region requires the selection of sample buildings that are representative of design and construction practices in the region and the finite element simulations of those buildings. Accordingly, this chapter presents the classification of the GLD RC frame inventory in the CEUS compiled as part of the Memphis Test Bed project; identifies low-, mid-, and high-rise GLD RC frames that represent such RC frame inventory in the CEUS; and develops finite element structural models of these sample GLD RC frames.

4.2 Memphis Test Bed Project

The Memphis Test Bed project, which is being conducted in the MAE Center, is intended to provide a demonstration of the concepts of CBRM and its application to the seismic vulnerability assessment of civil infrastructure in a typical at-risk region in the CEUS. Shelby County, TN, which includes the city of Memphis, is typical of a region that is prone to large earthquakes that may occur in the NMSZ but where earthquake hazard or risk mitigation has not been a major concern in building construction and public policy development until recently. Most of Shelby County (with a population of approximately 900,000) lies within approximately 70 km (45 miles) of the NMSZ. A survey of the building infrastructure in Shelby County, TN [French and Olshansky, 2001] revealed that
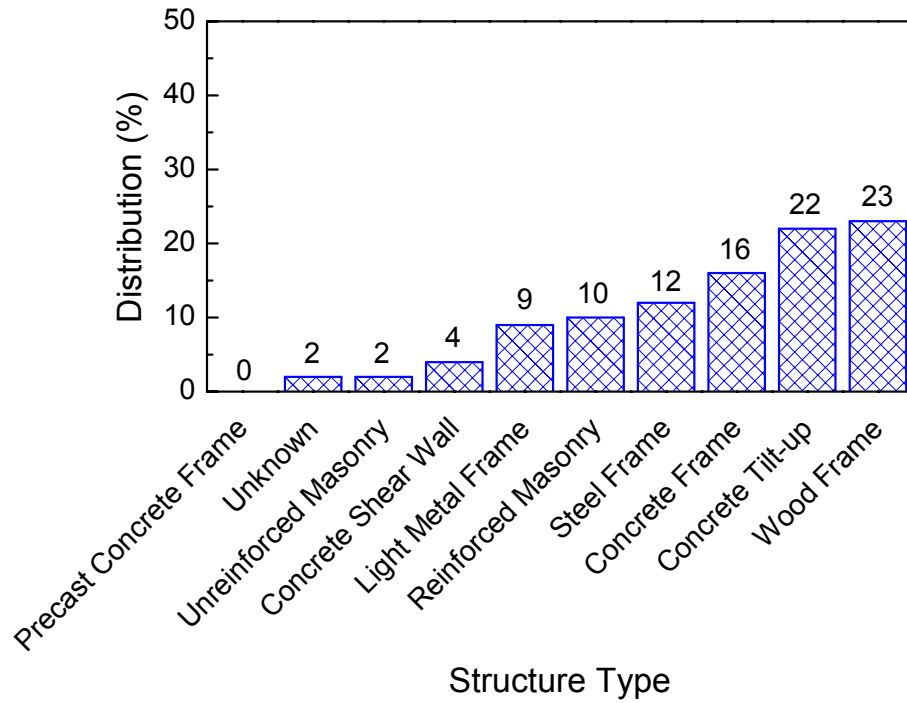
Figure 4.1 Distribution of buildings with appraised value greater than $5 million.

RC frames comprise less than 1% of the total building inventory, while 94% of the buildings are wood construction[a]. On the other hand, 16% of the buildings with appraised value greater than $5 million are RC frames, as illustrated in Figure 4.1. RC frames are classified based on their number of stories, design vintage, and use in Figure 4.2.

---

[a] The vast majority of the wood-frame buildings in Memphis are non-engineered residential buildings.
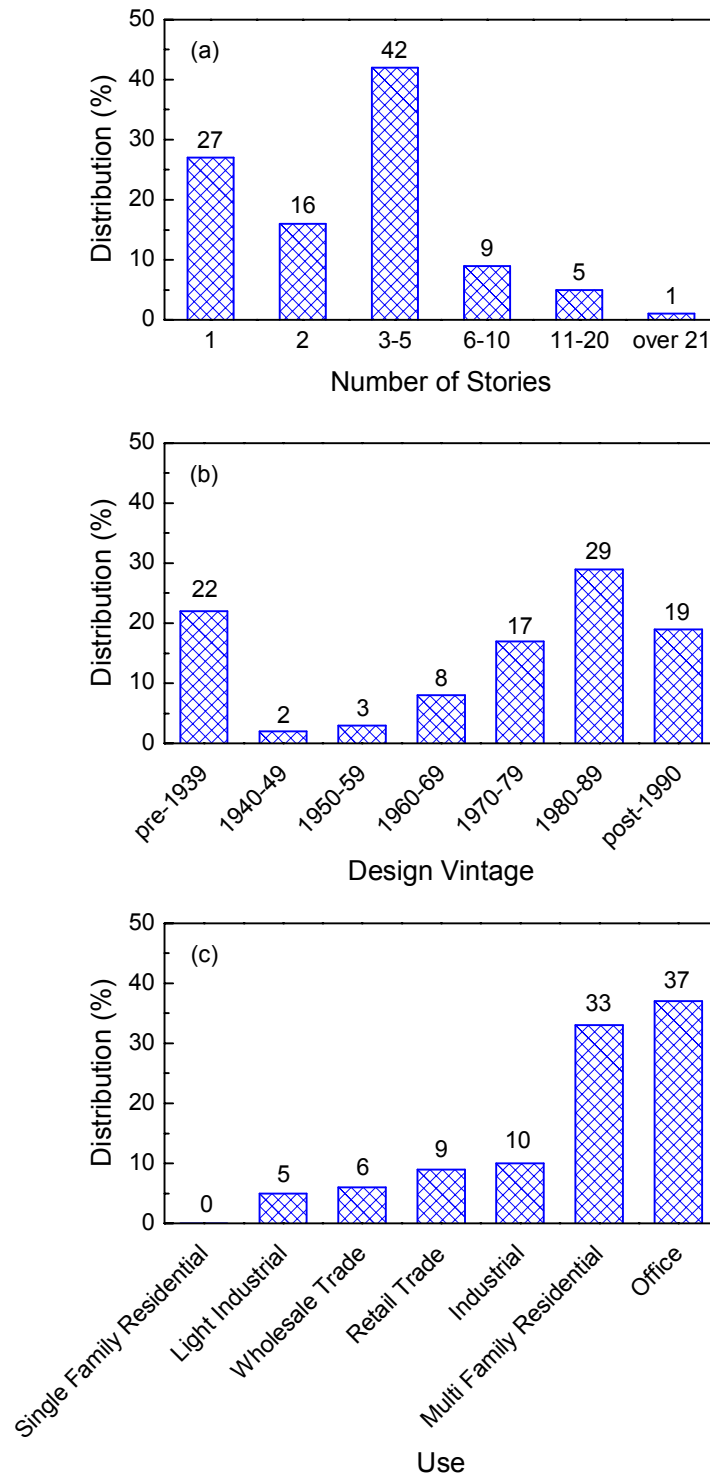
Figure 4.2 Classification of RC frames in Shelby County, TN based on their: (a) number of stories, (b) design vintage, and (c) use.

4.3 Representative Buildings of the RC Frame Inventory

Three-, six-, and nine-story GLD RC frames that are believed to represent the inventory of low-, mid-, and high-rise[b] RC frames in the CEUS were selected from Hoffmann *et al.* [1992], covering a broad range of building heights/periods (*cf.* Figure 4.2a) for seismic vulnerability assessment in the region. The frames were designed using detailing provisions of ACI Standard 318-89 [ACI Committee 318, 1989] for the gravity load combination $1.4DL + 1.7LL$, and hence they are typical of pre-1990 RC frames in the CEUS (*cf.* Figure 4.2b). All three frames represent typical office buildings (*cf.* Figure 4.2c) with identical symmetric floor plans. The design of the frames lacked any consideration of seismic action, and the lateral force requirements were determined by wind loads. Beam designs were governed by gravity loads rather than wind loads; and hence reinforcing steel (rebar) layouts were identical in beams at all story levels. Column section properties were identical over three-story heights. The elevation of the nine-story frame, together with the beam and column rebar layouts, are illustrated in Figure 4.3. The section properties and detailing in the top three stories of this frame, if separated, are identical to those of the three-story frame, and similarly for the six-story frame. The specified compressive strength of the concrete was 28 MPa (4,000 psi), whereas the design steel yield strength was 280 MPa (40,000 psi).

---

[b] The classification follows that adopted in Table 5.1 of the HAZUS manual [FEMA, 2003a], where RC frames with 1–3, 4–7, and 8+ stories are grouped.
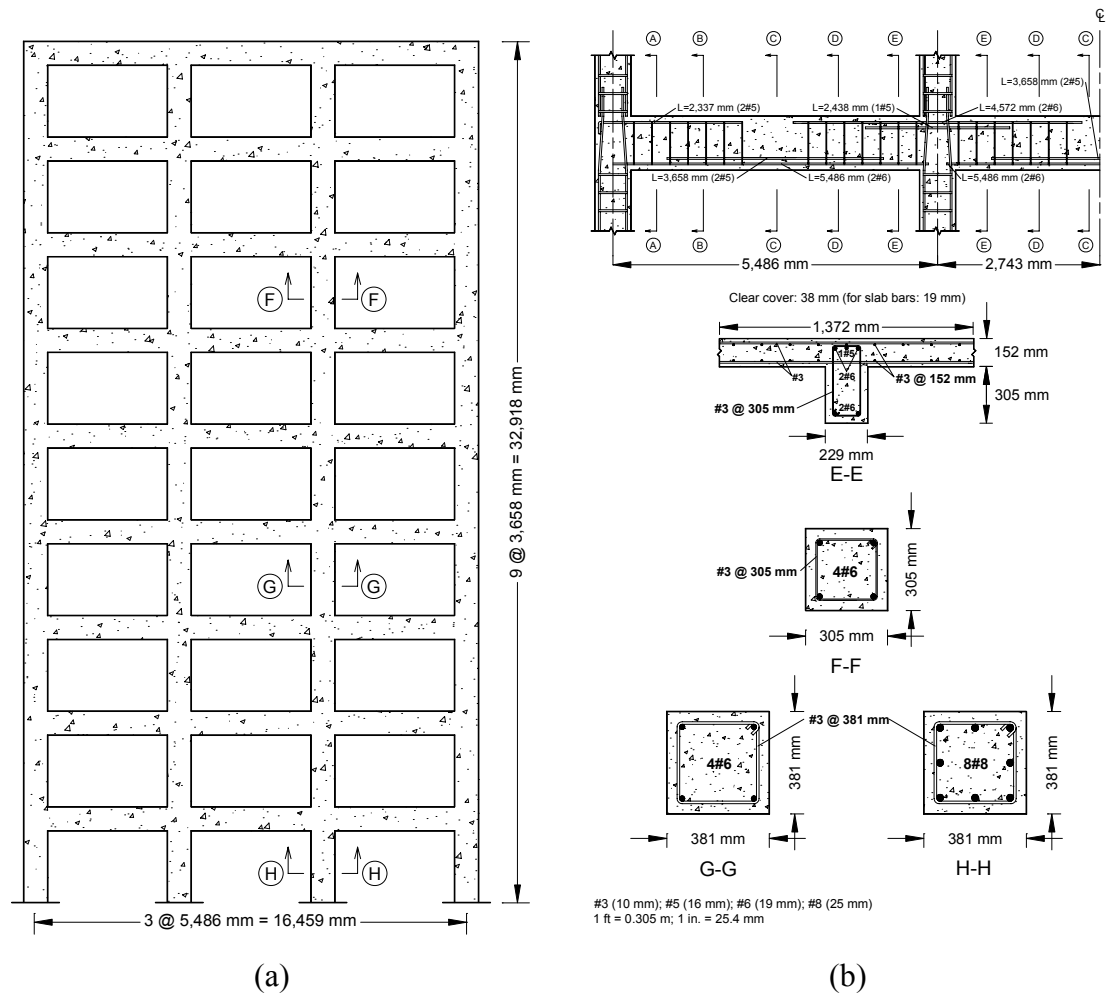
Figure 4.3 (a) Elevation and (b) beam and column reinforcing steel layouts; of the nine-story GLD RC frame.
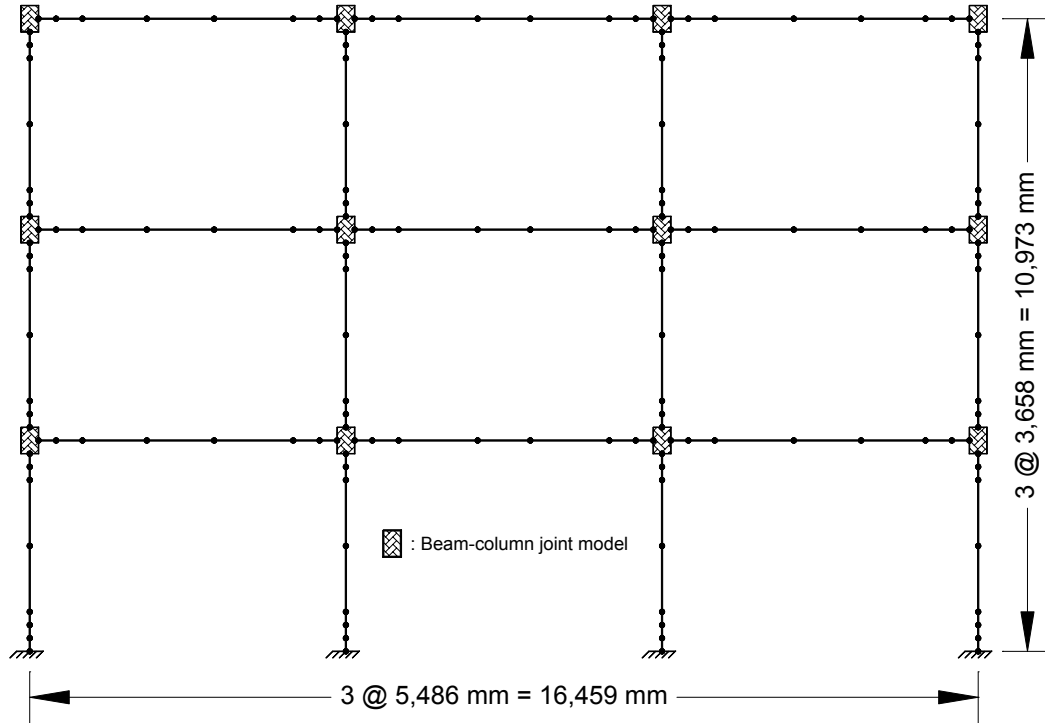
Figure 4.4 OpenSees model of the three-story frame (1 in. = 25.4 mm).

4.4 Finite Element Structural Models

Finite element analyses of the three-, six-, and nine-story GLD RC frames were performed using the open-source computational platform OpenSees [McKenna and Fenves, 2006]. OpenSees can account for geometric and material nonlinearities, and will facilitate the adoption of the beam-column joint model for GLD RC frames that will be developed in Chapter 6. Figure 4.4 shows the structural model of the three-story frame as a typical example. Displacement-based beam-column elements (with two integration points) were utilized in the two-dimensional structural models of the typical interior frames. Smaller elements were required near beam-column joint regions where significant inelastic actions may occur. Beam members were discretized such that points of rebar discontinuity along beam span could also be taken into account.
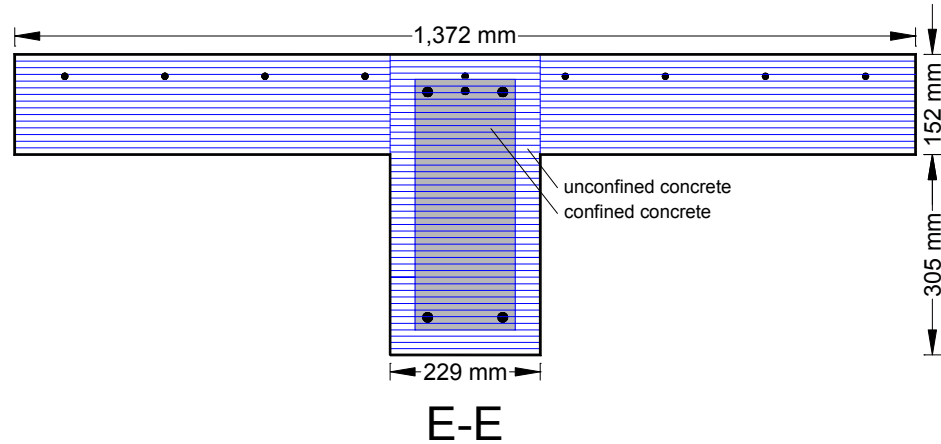
Figure 4.5 Discretization of beam sections (1 in. = 25.4 mm).

The fiber approach to element/section modeling, which makes use of the nonlinear uniaxial constitutive models of concrete and steel, enabled the modeling of the spread of inelasticity across the section depth and along the member length. Concrete compressive strength and steel yield strength were increased by 25% from their nominal values to account for the conservatism in nominal material strength with respect to *in situ* strength and the increase in strength that occurs under dynamic loading [Aslani and Miranda, 2005]. Cover and core concrete properties were calculated using the modified Kent and Park model [Park *et al.*, 1982], while steel properties were represented through a bilinear steel model with 0.5% strain hardening. The increase in concrete strength due to confinement was examined carefully and was found to be only marginal, varying in the range of 2–4% in locations where minimal transverse reinforcement (see Section 2.2) was provided in columns and beams (none in beam section C-C in Figure 4.3b). Figure 4.5 shows the discretization of beam sections (as an example) into layers of longitudinal steel bars and fibers of confined and unconfined concrete. Fibers were approximately 10 mm (0.4 in.) thick, and concrete cover losses in unconfined regions were modeled. The

43

effective width of the slab was defined according to ACI Standard 318 and the slab bars within this width were considered, except in the region close to the columns where the bottom bars lacked sufficient anchorage [Kurose *et al.*, 1991].

A distributed gravity loading of 40,000 N/m (2.74 kip/ft) was applied to the beam spans, while a dynamic mass of 15,700 N/(m/s^2) (1.08 kip/(ft/s^2)) was lumped at each beam-column joint for dynamic analysis, based on the load combination $1.0DL + 0.25LL$. In the NTHAs, hysteretic damping was simulated through hysteresis models of materials. Accordingly, viscous damping only reflected the damping present when the frames responded elastically, and a Rayleigh damping of 2% for the first two modes was assumed, based on the experimental findings from the three-story 1/3-scale GLD RC frame test [Bracci *et al.*, 1995].

OpenSees allows the analyst a choice of integration techniques and solution algorithms. Newmark's average acceleration time-stepping scheme, which is an unconditionally stable numerical integration algorithm that assumes constant acceleration over a time increment, was used in integrating the nonlinear dynamic equilibrium equation for each frame. The resulting equation was then solved using the Newton-Raphson method at each time step, the increment of which was chosen to be the same as that of the ground motion record. When the numerical solution failed to converge, the time increment was reduced to 1/10 of the original value. This reduction was applied up to three times if the problem persisted, resulting in a time increment equal to 1/1,000 of the original increment.[c] The time increment was set back to its previous value after 10

---

[c] For computational efficiency, the analysis was terminated when the maximum response of the frame measured in terms of interstory drift, exceeded 10%, at which point the solution always diverged.

analyses with the same reduced time step. This solution algorithm failed to converge at the point of collapse of the frame.

The non-ductile reinforcing details at the beam-column joints will be subsequently taken into account in the structural models. A beam-column joint model that addresses the lack of joint shear reinforcement and the insufficiently developed beam bottom bars will be developed in Chapter 6.

4.5 Summary

A survey of the building infrastructure in Shelby County, TN — a typical at-risk region in the CEUS — was presented. Three-, six-, and nine-story GLD RC frames that represent the RC frame inventory in the CEUS were identified. Finally, finite element structural models of these GLD RC frames of different heights were developed; these frames will be utilized in later fragility analyses with the incorporation of the beam-column joint model developed in Chapter 6.

CHAPTER 5

FRAMEWORK FOR SEISMIC RISK ASSESSMENT

5.1 Introduction

Seismic risk assessment deals with the probabilistic estimation of the safety and performance of buildings and other civil infrastructure under uncertain future seismic events. Several disciplines, including engineering seismology and geology, soil dynamics, structural mechanics and dynamics, are involved in this process [Chandler and Lam, 2001]. To incorporate all the information from these distinct disciplines in a probabilistic assessment procedure efficiently, a framework that allows the work of each discipline to be performed separately and subsequently combined for engineering decision is necessary. The framework should also quantitatively treat and propagate all sources of uncertainties involved in order to obtain reliable seismic risk assessments. There are basically two types of uncertainties: aleatoric and epistemic. Aleatoric uncertainties are due to factors that are inherently random in nature and are essentially irreducible. In contrast, epistemic uncertainties are knowledge-based, arising from assumptions made in the analysis of the system and from the limitations in the supporting databases; such uncertainties can be reduced with additional knowledge or more comprehensive analysis. In seismic performance and risk assessment of structures, both the randomness and uncertainty of the ground motion intensity demand, structural demand, and structural capacity need to be considered [Wen *et al.*, 2004].

This chapter lays out the framework for seismic risk assessment followed in later chapters; explains the concept of a seismic fragility, which is a key ingredient of the

framework; presents a probabilistic demand model that facilitates the derivation of fragilities through simulation-based reliability analysis; and describes how the core elements involved in this process are determined at the current state of the art: seismic intensity, structural demand, and limit states — damage assessment; followed by the fragility formulation adopted in this study.

5.2 Framework for Quantitative Risk Analysis

The framework for seismic risk assessment is provided by the theorem of total probability [*e.g.*, Ellingwood *et al.*, 2007]

$$
\begin{aligned}
&P[Loss > c] = \\
&\sum_{si} \sum_{LS} \sum_{ds} P[Loss > c|DS = ds] P[DS = ds|LS] P[LS|SI = si] P[SI = si]
\end{aligned} \tag{5.1}
$$

in which SI is the seismic intensity, measured in terms of ground motion (peak ground acceleration, velocity) or spectral (spectral acceleration, velocity, or displacement) intensities, $P[LS|SI = si]$ is the probability of reaching a structural limit state LS, given the occurrence of $SI = si$, $P[DS = ds|LS]$ is the probability of damage state DS, given limit state LS, and $P[Loss > c|DS = ds]$ is the probability that the loss exceeds c, given that $DS = ds$. The breakdown in this equation identifies the fundamental contributors to the risk assessment clearly: seismology or seismic hazard ($P[SI = si]$), structural engineering ($P[LS|SI = si]$), and building economics and losses ($P[Loss > c|DS = ds]$). The term $P[DS = ds|LS]$ bridges the gap between structural engineering analysis, which assesses limit states in terms of forces and deformations, and loss estimation, which relates damage states (*e.g.*, minor, moderate, severe) to economic losses, expressed as a percentage of replacement cost.

5.3 Fragility Modeling

The term $P[LS|SI = si]$ in Eq. 5.1 is denoted the *fragility*, which defines the capability

(expressed in terms of probability) of an engineered system to withstand a specified event

[Kennedy and Ravindra, 1984]. In some applications, the fragility is described as the

conditional probability of damage

$$P[DS = ds|SI = si] = \sum_{LS} P[DS = ds|LS]P[LS|SI = si]. \tag{5.2}$$

In FEMA 273 and its successor FEMA 356 [FEMA, 1997a/2000b] and some other

documents [*e.g.*, SEAOC Vision 2000, 1995], the structural response terms are mapped

directly to specific damage states or performance levels (*e.g.*, an interstory drift of 2% for

RC frames is tantamount to the *life safety* level); in that case, the conditional probabilities

$P[DS = ds|LS]$ are either one or zero, and the summation in Eq. 5.2 is not required. More

generally, several structural limit states may map to a specific damage state ds ; hence the

form of Eq. 5.2.

The fragility is commonly modeled by a lognormal cumulative distribution

function (CDF), a choice that has been supported by numerous research programs during

the past decade in disparate fields [Ellingwood, 1990; Singhal and Kiremidjian, 1996;

Song and Ellingwood, 1999; Shinozuka *et al.*, 2000; Tekie and Ellingwood, 2003]. The

fragility is described by

$$F_R(x) = \Phi\left[\frac{\ln(x/m_R)}{\beta_R}\right] \tag{5.3}$$

in which m_R is the median capacity (expressed in units that are dimensionally consistent

with the control variable used to define the seismic hazard, *e.g.*, PGA or S_a), β_R is the

logarithmic standard deviation, which is approximately equal to the coefficient of

variation (COV) in capacity, V_R, when $V_R \leq 0.3$, and $\Phi[\ ]$ is the standard normal probability integral. Equation 5.3 depicts $P[LS|SI = si]$ or $P[DS = ds|SI = si]$ in Eqs. 5.1 and 5.2 when the state of knowledge is essentially perfect (at the scales of customary structural engineering and mechanics). In this simple formulation, the CDF and its parameters m_R and β_R measure inherent randomness (or aleatoric uncertainty) in seismic capacity. Such uncertainties are essentially irreducible at the scale of current engineering analysis.

Additional sources of uncertainty in estimated capacity arise from assumptions made in modeling the system (*e.g.*, two-dimensional idealizations of building frames, approximate models of connections or joints, neglect of non-structural components). In the presence of these knowledge-based (or epistemic) uncertainties, the structural fragility can be visualized as a family of CDFs, reflecting incomplete knowledge regarding the parameters used to model the structural fragility: in the median, COV, and the CDF itself. To first order, these uncertainties can be vested in the estimate of the median capacity, m_R, in Eq. 5.3. Under this assumption, m_R is replaced by a (Bayesian) random variable, M_R, which is modeled by a lognormal distribution with median m_R and logarithmic standard deviation β_{RU}. Then, the overall uncertainty in capacity (aleatoric and epistemic) is displayed by the *family* of lognormal CDFs, defined by parameters (m_R, β_{RR}, β_{RU}), in which the aleatoric uncertainty β_{RR}, is distinct from β_{RU}. In many applications, however, it is desirable to have one overall estimate of fragility for review, assessment, and decision purposes that reflects both aleatoric and

epistemic uncertainty. Such an estimate is provided by the mean fragility, defined by

replacing β_R in Eq. 5.3 with

$$\beta_R = \sqrt{\beta_{RR}{}^2 + \beta_{RU}{}^2} \qquad (5.4)$$

[Ellingwood, 1998].

5.4 Probabilistic Seismic Demand Model

A probabilistic seismic demand model, which relates the structural demand, D, to the seismic intensity, SI, facilitates the derivation of seismic fragilities, discussed above, when using simulation-based analytical procedures such as NTHA. Perhaps the simplest demand model relating the D to the SI is [Cornell *et al.*, 2002]

$$D = a \cdot SI^b \cdot \varepsilon \qquad (5.5)$$

where ε is a lognormal random variable with median one and logarithmic standard deviation $\sigma_{\ln\varepsilon}$, depicting the uncertainty in the relation. The parameters a and b are determined by linear regression of ln$D$ on lnSI obtained from simulations, while $\sigma_{\ln\varepsilon}$ is estimated using

$$\sigma_{\ln\varepsilon} = \sqrt{\frac{1}{n-2}\sum_{i=1}^{n}\left[\ln(D_i) - \ln\left(a \cdot SI_i{}^b\right)\right]^2} \qquad (5.6)$$

where n is the number of (D, SI) data points. The probability that the D exceeds d given the value of SI is then given by

$$P[D \geq d | SI = x] = 1 - \Phi\left[\frac{\ln\left(d/ax^b\right)}{\sigma_{\ln\varepsilon}}\right]. \qquad (5.7)$$

Similar to Eq. 5.3, the probability that the structural capacity, C, is less than d is given by

$$P[C < d] = \Phi\left[\frac{\ln\left(d/\hat{C}\right)}{\beta_C}\right] \qquad (5.8)$$

where $\hat{C}$ and β_C are respectively the median and logarithmic standard deviation of the structural capacity, C, associated with the limit state LS. With the probabilistic representation of the structural capacity, C, by Eq. 5.8, and that of the structural demand, D, by Eq. 5.7, the conditional probability that the structural capacity, C, fails to resist the structural demand, D, given the seismic hazard, SI, *i.e.*, the fragility, can be represented by

$$P[C < D | SI = x] = 1 - \Phi\left[\frac{\ln\left(\hat{C}/ax^b\right)}{\sqrt{\sigma_{\ln\varepsilon}^2 + \beta_C^2}}\right]. \qquad (5.9)$$

5.5 Core Elements of the Framework

The seismic risk analysis presented above requires a convolution of seismic hazard, seismic demand, structural damage, and loss estimation analyses (see Eq. 5.1). Setting aside the loss estimation component, the core elements that display the products of these components and serve as the links between them, namely, seismic intensity, structural demand, and structural limit state, are explored in the following, considering alternative measures of each that have been proposed in the literature.

5.5.1   Seismic Intensity Measures

The seismic intensity measure (IM) depicts the seismic hazard and the subsequent structural response analysis is conditioned on the IM in a seismic risk assessment framework. The desired IM should be *sufficient* and *efficient*, and have a hazard curve that is relatively easy to compute, *hazard computability* [Giovenale *et al.*, 2004].

In search of these optimum characteristics, researchers have proposed several IMs. These IMs can be classified into two groups as structure-independent (ground motion characteristics-based) and structure-specific. Among those solely based on strong motion record properties are PGA (peak ground acceleration), peak ground velocity (PGV), peak ground displacement (PGD), Arias intensity (AI), and duration of the motion. Structure-specific IMs are spectral response quantities: S_a (spectral acceleration), spectral velocity (S_v), and spectral displacement (S_d), usually computed at the fundamental period of the structure, and several other parameters derived from these fundamental quantities. In the following three sub-sections, the significant IMs are reviewed with their advantages and disadvantages.

5.5.1.1   Structure-Independent IMs

The PGA has been the most commonly used seismic IM until recently. It does not require any structural response computation and seismic hazard curves expressed in terms of PGA are readily available through the USGS. However, its inefficiency in certain cases has been noted; the dispersions of DMs when the IMs are peak ground motion characteristics are often large [Shome *et al.*, 1998]. The PGA is an effective IM only for short-period structures [Kurama and Farrow, 2003] falling in the acceleration-amplified region of a typical response spectrum ($T \leq 0.5$ s; Chopra [1995]). Moreover, the PGA correlates poorly with the structural damage. In contrast, the PGV provides a better indicator of the potential of an earthquake to cause structural damage [Glaister and Pinho, 2003]. The PGV, which is related to the energy in the ground motion, correlates well with energy-based response parameters over certain periods [Conte *et al.*, 2003] and with maximum floor acceleration [Elenas and Meskouris, 2001].

5.5.1.2   Structure-Specific IMs

Structure-specific IMs are more efficient, in that they better capture the damage potential of earthquakes on structures, thus reducing the dispersion of DM given IM. The linear-elastic pseudo-spectral acceleration, S_a, being dependent on structural properties as well as ground motion characteristics, is currently the most frequently used IM [Krawinkler *et al.*, 2003; Giovenale *et al.*, 2004]. It is usually defined as the value at the fundamental period of the structure. The USGS currently maps seismic hazard in terms of S_a for a 5% damped oscillator at several probability levels, including 10%, 5%, and 2% PE in 50 yr. The efficiency of S_a in reducing the variability of DM was studied by Shome and Cornell [1998] and Shome *et al.* [1998], who concluded that it was the best single-valued IM among the alternatives. More recent research has pointed out a number of shortcomings of using the S_a as an IM, among them:

(1) The period softening associated with inelastic behavior [Cordova *et al.*, 2000; Krawinkler *et al.*, 2003; Giovenale *et al.*, 2004; Luco and Cornell, 2007] is ignored;

(2) The contribution of higher modes to the structural response [Krawinkler *et al.*, 2003; Giovenale *et al.*, 2004; Luco and Cornell, 2007] is not considered; and

(3) It is not particularly efficient nor sufficient for:

(a) long-period buildings [Shome *et al.*, 1998; Luco and Cornell, 2007],

(b) soft soil ground motions [Kurama and Farrow, 2003; Luco and Cornell, 2007], and

(c) near-field ground motions [Krawinkler *et al.*, 2003; Kurama and Farrow, 2003; Luco and Cornell, 2007].

In short, S_a is an efficient and sufficient IM for first-mode dominant buildings on stiff soil conditions subjected to far-field ground motions that are not very sensitive to earthquake magnitude, M, and source-to-site distance, R. Spectral velocity and displacement, S_v and S_d, are equivalent to S_a in reducing the scatter of DM due to their definition

$$S_a = \omega \cdot S_v = \omega^2 \cdot S_d \tag{5.10}$$

where ω is the natural frequency of an SDOF oscillator.

5.5.1.3   Multi-Parameter IMs

The difficulty of accounting for the shortcomings of S_a listed above with a single parameter has led to proposals for multi-parameter IMs [*e.g.*, Luco and Cornell, 2007]. Krawinkler *et al.* [2003] stated that no single parameter is ideally suited to capture "all intensity, frequency content, and duration information that significantly affect the elastic and inelastic response of complex soil-structure systems." Cordova *et al.* [2000], for example, proposed a two-parameter IM that accounts for period softening

$$S^* = S_a(T_1) \cdot \left[\frac{S_a(z \cdot T_1)}{S_a(T_1)} \right]^{\chi} \tag{5.11}$$

where z and χ are obtained by calibration to the results of NTHAs (optimization of reduction in dispersion) to be 2 and 0.5, respectively. More recently, intensity vectors as opposed to scalar IMs have been proposed [*e.g.*, Baker and Cornell, 2005], but issues associated with their application and compatibility with customary hazard measures and for risk computation by Eq. 5.1 have not yet been resolved [Giovenale *et al.*, 2004]. The USGS currently provides seismic hazard curves in terms of PGA and S_a. To compute

hazard curves in terms of other IMs via Probabilistic Seismic Hazard Analysis (PSHA, as defined by Cornell [1968]), compatible attenuation relationships are needed. Attenuation relationships have been published in the literature for some of the IMs mentioned above but not for others. Among those having attenuation relationships are PGV, PGD, and AI. Cordova *et al.* [2000] derived the necessary attenuation relationships for the IM they proposed, S^* in Eq. 5.11, by modifying the already available attenuation relationships for S_a using the functional form of the S^*.

5.5.2 Structural Demand Measures

The structural demand measure (DM) expresses the structural response (see Eq. 5.7) and relates the response further to a particular damage state that the structure attains as a consequence of an earthquake. DMs of primary interest are parameters that correlate best with various types of damage: structural, non-structural, and contents damage, as seismic losses are estimated from damage states, identified in terms of DMs [Krawinkler *et al.*, 2003]. Maximum interstory drift is reported to be a relevant DM for damage assessment of structural and deformation-sensitive non-structural components, whereas floor acceleration and velocity are relevant DMs for assessment of damage to other non-structural components and building contents [*e.g.*, Krawinkler *et al.*, 2003]. Several other DMs have been proposed, which can be classified into four generic groups of deformation-, ductility-, energy-based DMs, and combinations of the first three. The frequently used DMs, belonging to each group, respectively, can be listed as maximum interstory drift [*e.g.*, Cornell *et al.*, 2002], displacement ductility [*e.g.*, Shome *et al.*, 1998], hysteretic energy [*e.g.*, Conte *et al.*, 2003], and Park and Ang [1985] damage

index [*e.g.*, Singhal and Kiremidjian, 1996]. A comprehensive review of DMs for RC structures is given in Williams and Sexsmith [1995].

5.5.3   Structural Limit States

Fragility analysis (see Eq. 5.9) is completed with the introduction of limit states (LSs) — expressed with the same parameter of DMs — corresponding to certain performance levels. The LSs depict the structural capacities at the thresholds of damage states. LSs can be defined for structural or non-structural damage states, or both, depending on the application, as monetary losses and downtime due to earthquake damage are controlled by a combination of those states. Several guidelines and similar documents qualitatively describe performance levels (or damage states) for purposes of building performance and seismic risk assessment. SEAOC Vision 2000 defines five performance (damage) levels: fully operational (negligible), operational (minor or light), life safety (moderate), near collapse (major or severe), and collapse (complete). FEMA 273/356 similarly defines three building performance levels: immediate occupancy (IO), life safety, and collapse prevention (CP); and assigns interstory drifts of 1%, 2%, and 4% to define these performance levels for RC frames.

5.6 Fragility Formulation

The seismic fragilities in this study are developed from nonlinear analyses of building frame response using OpenSees. The seismic demand on the frames is assessed through NTHAs that are performed using the ensembles of synthetic earthquake ground motions presented in Chapter 3, and is represented by the probabilistic demand model given by Eq. 5.5. The maximum interstory drift angle, θ_{max}, is selected as the DM due to its

capability to provide insight about the potential for structural or local collapse. Consistent with the approach in the SAC project [Cornell *et al.*, 2002], the spectral acceleration at the fundamental period of the frame, $S_a(T_1)$, for 5% damping is adopted as the IM. The capacities are defined by the LSs that correspond to three widely used performance levels (immediate occupancy, life safety, and collapse prevention) in the earthquake community (*e.g.*, FEMA 273/356). These performance levels are adopted so that the results are consistent with, and can be compared to, previous work. The IO level is described by the limit below which the structure can be occupied safely without significant repair. The median IO limit[a] is defined by the θ_{max} beyond which the frame enters the inelastic range, and is determined from an NSP analysis performed using a lateral force pattern that is based on the first mode shape. The life safety level occurs at a deformation at which "significant" damage has been sustained, but at some margin below incipient collapse. Because this limit is hard to quantify in terms of interstory drift, the intermediate level is identified herein as the θ_{max} at which significant structural damage (SD) has occurred; the median SD limit[a] is associated with a θ_{max} of 2% [FEMA 356, 2000b]. Finally, the CP level is defined by the point of incipient collapse of the frame due to either severe strength degradation of members or significant P-Δ effects resulting from excessive lateral deformations. The CP limit[a] is calculated from statistical analyses of incremental dynamic analysis (IDA) results [Vamvatsikos and Cornell, 2002], and its median is defined by the median θ_{max} prior to failure to converge[b] in the IDA.[c]

---

[a] The uncertainty associated with this LS is captured by the term β_C in Eq. 5.12.
[b] See Section 7.2.1 for how the failure to converge is defined.
[c] IDAs were performed with S_a increments of 0.01 g.

The seismic fragilities are then computed by

$$P[C < D | S_a = x] = 1 - \Phi \left[\frac{\ln(\hat{C}/ax^b)}{\sqrt{\beta_{D|S_a}^2 + \beta_C^2 + \beta_M^2}} \right] \qquad (5.12)$$

in which the epistemic (modeling) uncertainty, β_M, has been introduced as suggested by Eq. 5.4, and where $\beta_{D|S_a}$ and β_C denote, respectively, the aleatoric uncertainties $\sigma_{\ln\varepsilon}$ and β_C, in D and C in Eq. 5.9. $\beta_{D|S_a}$ is calculated using the NTHAs results with Eq. 5.5. β_C depends on the LS considered. At the IO and SD levels, β_C must capture the uncertainty with respect to the assumption that these limits can be defined by the elastic limit and a θ_{max} of 2%, respectively. It is assumed that β_C = 0.25 for both IO and SD levels. For the CP level, β_C is set equal to the logarithmic standard deviation, ζ, of structural capacity calculated using the IDA results, discussed above. β_M is assumed to be 0.20, based on the assumption that the modeling process yields an estimate of building frame response that, with 90% confidence, is within ±30% of the actual value [Wen *et al.*, 2003].

5.7 Summary

The seismic risk assessment framework that will be adopted in the quantitative risk analysis of GLD RC frame inventory in the CEUS in subsequent chapters was presented. Appropriate interface measures that provide the flow of information between the different disciplines involved were determined from the current state of the art, and the role of structural engineering in this framework was identified. The concept of a seismic fragility, which is defined as the probability of reaching stipulated damage states

(performance levels) as a function of (given) a specified measure of earthquake ground motion intensity, was formulated for the simulation-based reliability analysis performed subsequently in later chapters.

CHAPTER 6

MODELING BEAM-COLUMN JOINTS OF GRAVITY LOAD

DESIGNED REINFORCED CONCRETE FRAMES[a]

6.1 Introduction

Finite element-based structural models of GLD RC frames used in simulation-based seismic fragility analysis must incorporate accurate models of those critical details that have been identified as being problematic. Previous research (summarized in Chapter 2) on the seismic performance of GLD RC frames has revealed that: (1) the first four problematic reinforcing details listed in Section 2.2 are critical in making such frames vulnerable to seismic demands; (2) the lack of adequate transverse reinforcement has only a marginal effect on performance (Confinement of the concrete core by transverse reinforcement can be taken into account through confined concrete models such as the modified Kent and Park model [Park *et al.*, 1982] in fiber models as presented in Chapter 4); and (3) previous tests have not pointed to lapped splices and construction joints as a source of poor behavior. Of the non-ductile reinforcing details that make GLD RC frames vulnerable to seismic demands (*i.e.*, the first four of the non-ductile reinforcing details listed in Section 2.2), the latter two are reflected explicitly in existing finite element platforms. However, a new joint model is required to capture the deficiency in joint shear behavior that results from a lack of transverse shear reinforcement and insufficient positive beam bar anchorage in the finite element analysis.

---

[a] This chapter is an extended version of the manuscript: Celik OC, Ellingwood BR [2007] "Modeling beam-column joints in fragility assessment of gravity load designed reinforced concrete frames," *Journal of Earthquake Engineering*, in press.

This chapter focuses on modeling shear and bond-slip behavior of the beam-column joints in GLD RC frames. Following a critical appraisal of the literature on models for simulating the RC beam-column joint response, a joint model is developed that is based on the experimental determination of joint panel shear stress-strain relationship. The panel zone constitutive parameters are defined to replicate the experimental joint shear stress-strain relationships, eliminating the need for further calibration, while the effect of bond-slip is taken into account through a reduced envelope for the joint shear stress-strain relationship. This modeling scheme is validated on two full-scale experimental RC beam-column joint test series. Seismic demand analyses of GLD RC frames incorporating the proposed beam-column joint model demonstrate the importance of modeling shear and bond-slip behavior in joints when assessing seismic performance of GLD frames.

6.2 Review of Beam-Column Joint Modeling in GLD RC Frames

Beam-column joint behavior is governed by shear and bond-slip in GLD RC frames. The typical practice of providing little or no joint shear reinforcement leads to shear deformations in the panel zone that may be substantial. This practice also leads to joint shear failure that can restrict the utilization of the flexural capacities of the joining beams and columns. Moreover, the common practice of terminating the beam bottom reinforcement within the joints without a hook makes the bottom reinforcement prone to pullout under a seismic excitation. Insufficient beam bottom bar anchorage precludes the formation of bond stresses necessary to develop the yield stress in the beam bottom reinforcement. Thus, the positive beam moment capacity cannot be utilized. Models of

RC beam-column joint response that have been proposed in the literature are reviewed in the following.

Hoffmann *et al.* [1992] and Kunnath *et al.* [1995a] modified the flexural capacities of the beams and columns of GLD RC frames to model insufficient positive beam bar anchorage and inadequate joint shear capacity implicitly. To account for insufficient positive beam bar anchorage, the pullout moment capacity of the beam was approximated as the ratio of the embedment length to the required development length per ACI 318-89 multiplied by the yield moment of the section. This approximation required that the yield strength of the discontinuous steel be reduced by the ratio of the actual to the required anchorage length. To model inadequate joint shear capacity, the flexural capacities of the beams and columns framing into the joint were reduced to a level that would induce shear failure of the joint. However, this modeling did not consider shear deformations of the joint. The proposed procedure was utilized in inelastic dynamic time history analyses of typical three-, six-, and nine-story GLD RC frames, which revealed that these frames are susceptible to damage from joint shear failures and weak column-strong beam effects leading to soft-story collapses.

Alath and Kunnath [1995] modeled the joint shear deformation with a rotational spring model with degrading hysteresis. The finite size of the joint panel was taken into account by introducing rigid links (see Figure 6.1a). The envelope to the shear stress-strain relationship was determined empirically, whereas the cyclic response was captured with a hysteretic model that was calibrated to experimental cyclic response. The model was validated through a comparison of simulated and experimental response of a typical GLD RC frame interior beam-column joint subassembly.
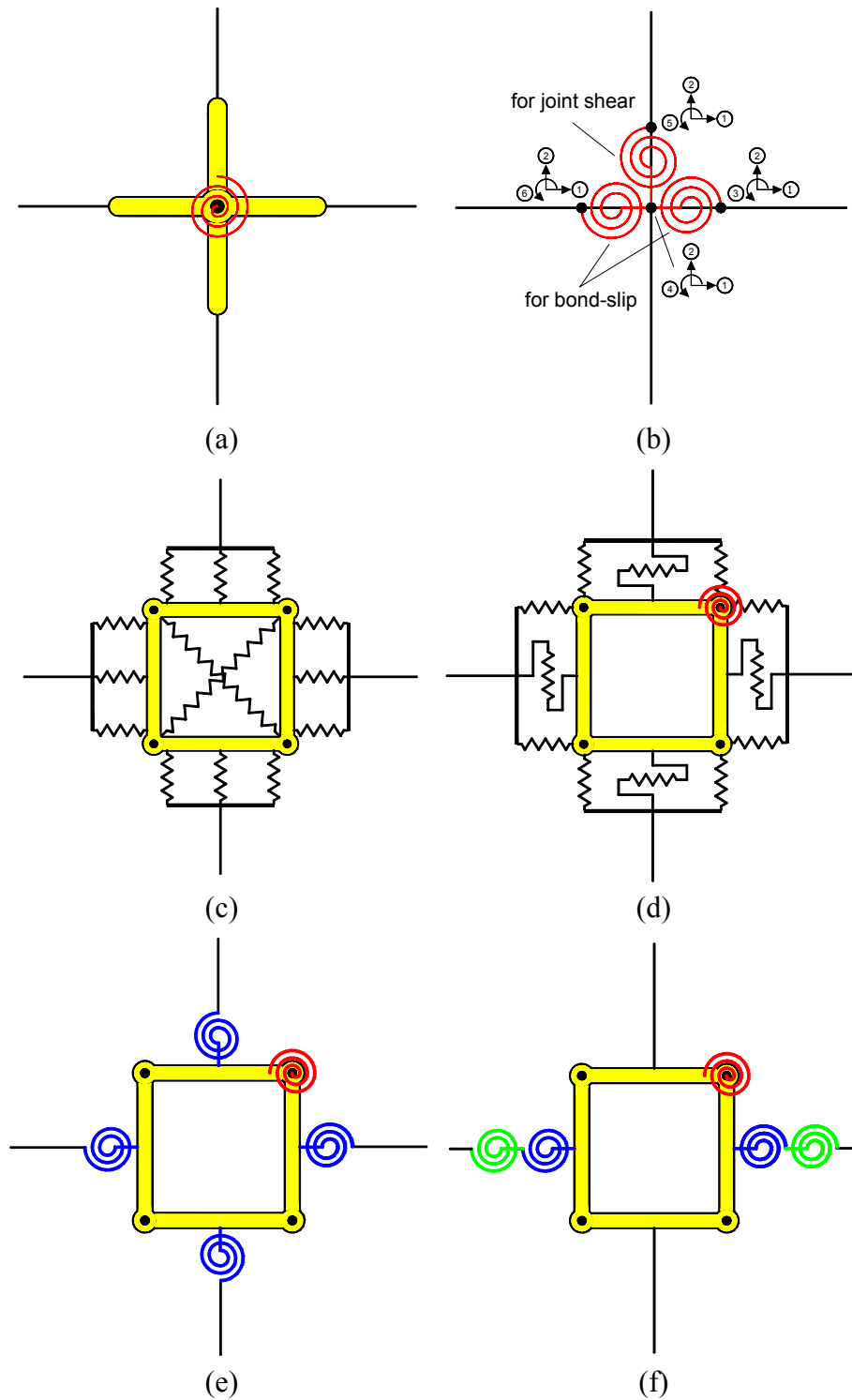
Figure 6.1 Existing beam-column joint models: (a) Alath and Kunnath [1995], (b) Biddah and Ghobarah [1999], (c) Youssef and Ghobarah [2001], (d) Lowes and Altoontash [2003], (e) Altoontash [2004], and (f) Shin and LaFave [2004].

Biddah and Ghobarah [1999] modeled the joint shear and bond-slip deformations with separate rotational springs (see Figure 6.1b). The shear stress-strain relationship of the joint was simulated using a tri-linear idealization based on a softening truss model [Hsu, 1988], while the cyclic response of the joint was captured with a hysteresis relationship with no pinching effect. The bond-slip deformation was simulated with a bilinear model based on previous analytical and experimental data. The cyclic response of the bond-slip spring was captured with a hysteresis relationship that accounts for pinching effects. The model was validated using experimental data on exterior joints of ductile and non-ductile frames. Ghobarah and Biddah [1999] utilized this joint element in performing dynamic analyses of three- and nine-story GLD RC buildings, designed to be typical of office buildings constructed during the 1960s in North America and containing the non-ductile reinforcing details identified above. The authors compared the dynamic response of three- and nine-story frames modeled with joint elements to the response of similar frames with rigid joints when subjected to strong motion records scaled to represent earthquakes capable of producing minor, moderate, and severe damage. The comparisons revealed that accounting for joint shear and bond-slip deformations in modeling results in significantly larger drifts, particularly for the nine-story frame.

Youssef and Ghobarah [2001] proposed a joint element (see Figure 6.1c) in which two diagonal translational springs connecting the opposite corners of the panel zone simulate the joint shear deformation; 12 translational springs located at the panel zone interface simulate all other modes of inelastic behavior (*e.g.*, bond-slip, concrete crushing); and elastic elements were used for the joining elements. The model was validated using experimental test results of ductile and non-ductile exterior beam-column

joints. This model requires a large number of translational springs and a separate constitutive model for each spring, which may not be available and restricts its applicability.

Lowes and Altoontash [2003] proposed a four-node 12-DOF joint element (see Figure 6.1d) that explicitly represents three types of inelastic mechanisms of beam-column joints under reversed cyclic loading. Eight zero-length translational springs simulate the bond-slip response of beam and column longitudinal reinforcement; a panel zone component with a zero-length rotational spring simulates the shear deformation of the joint; and four zero-length shear springs simulate the interface-shear deformations. Because experimental research that reports bond-slip data of full-scale frames or beam-column joint subassemblies is scarce, the envelope and cyclic response of the bar stress versus slip deformation relationship were developed from tests of anchorage-zone specimens and assumptions about the bond stress distribution within the joint. To define the envelope to the shear stress-strain relationship of the panel zone, the modified-compression field theory (MCFT) [Vecchio and Collins, 1986] was utilized. The cyclic response of the panel zone was modeled by a highly pinched hysteresis relationship, deduced from experimental data provided by Stevens *et al.* [1991]. A relatively stiff elastic load-deformation response was assumed for the interface-shear components. Lowes *et al.* [2004] later attempted to model the interface-shear based on experimental data; this later effort also predicted a stiff elastic response for the interface-shear.

Mitra and Lowes [2004] subsequently evaluated the model proposed earlier by Lowes and Altoontash [2003] by comparing the simulated response with the experimental response of beam-column joint subassemblies. The experimental data

included specimens with at least a minimal amount of transverse reinforcement in the panel zone, which is consistent with the intended use of the model. Joints with no transverse reinforcement, a reinforcing detail typical in GLD RC frames, were excluded from this study. Mitra and Lowes noted that in joints with low amounts of transverse reinforcement, shear is transferred primarily through a compression strut, a mechanism, which is stronger and stiffer than predicted by the MCFT.

Altoontash [2004] simplified the model proposed by Lowes and Altoontash [2003] by introducing a model consisting of four zero-length rotational springs located at beam- and column-joint interfaces, which simulate the member-end rotations due to bond-slip behavior, while the panel zone component with a rotational spring remains to simulate the shear deformation of the joint (see Figure 6.1e). The constitutive relationship (*i.e.*, the envelope and the cyclic response) for the panel zone from Lowes and Altoontash [2003] was retained, enabling the calculation of constitutive parameters based on material properties, joint geometry, joint reinforcing steel ratio, and axial load. However, calibration of constitutive parameters was still required for joints with no transverse reinforcement to overcome the limitation of the MCFT for such joints. Altoontash [2004] adapted the constitutive model developed for the translational bond-slip springs in Lowes and Altoontash [2003] in a fiber section analysis to derive the constitutive model for the member-end rotational springs, but noted that detailed information on bond-slip response is needed. Furthermore, the development length was assumed to be adequate to prevent complete pullout, which is not necessarily true for bottom reinforcement in beams of GLD RC frames. The validation studies include RC interior beam-column joint tests [Walker, 2001] and a two-story RC frame.

Shin and LaFave [2004] represented the joint by rigid elements located along the edges of the panel zone and rotational springs embedded in one of the four hinges linking adjacent rigid elements (see Figure 6.1f). The envelope to the joint shear stress-strain response was approximated by the MCFT, whereas experimental data were used to calibrate the cyclic response. Two rotational springs (in series) located at beam-joint interfaces simulate the member-end rotations due to bond-slip behavior of the beam longitudinal reinforcement and plastic hinge rotations due to inelastic behavior of the beam separately. The constitutive parameters for bond-slip deformation were based on a previous study reported by the authors. A comparison of the predictions from this model to results of an RC interior joint test showed good agreement. The proposed joint model is intended for RC beam-column joints of ductile moment frames designed and detailed following modern seismic code requirements.

LaFave and Shin [2005] discussed the use of the MCFT in defining the envelope to the shear stress-strain relationship of the panel zone. The authors collected from the literature experimental joint shear stress and strain data of 50 RC interior joint subassemblies that failed in joint shear. The envelope responses to the experimental data typically follow a quad-linear curve that connects three key points (corresponding to joint shear cracking, reinforcement yielding, and joint shear strength) starting from the origin and has a degrading slope once past the joint shear strength. For each of the experimental subassemblies, the authors applied the MCFT as described by Lowes and Altoontash [2003] to determine the ordinates of the envelope points, particularly the maximum joint shear stress (*i.e.*, joint shear strength). Comparison of the ratio of analytical (MCFT) to experimental maximum joint shear stress versus the ratio of transverse joint shear

reinforcement provided to that required by ACI 318-02 [ACI Committee 318, 2002] revealed that the MCFT approach consistently underestimates the joint shear strength for joints that do not satisfy the joint reinforcement requirement per ACI 318-02. Hence, the MCFT may be inappropriate for modeling GLD RC frames, which have little or no joint transverse shear reinforcement.

The modeling schemes that incorporate joint shear and bond-slip deformations discussed herein lack the appropriate constitutive models for general configurations of GLD RC frame beam-column joints.

<h3 style="text-align:center">6.3 Modeling Joint Behavior in Finite Element Analysis</h3>

Moment transferred through the rotational spring that simulates joint shear deformations constitutes the basic input for most of the modeling schemes discussed above. In this study, the moment-rotation relationship is derived from the experimental determination of joint shear stress and strain. The effect of bond-slip on joint behavior is taken into account through a modification proposed for the joint shear stress-strain relationship.

6.3.1 Experimental Determination of Joint Shear Stress and Strain

Joint shear stress is defined herein as the horizontal force transferred at the mid-height horizontal section of a beam-column joint divided by the joint area. A typical interior beam-column joint test setup for the experimental determination of joint shear stress is shown in Figure 6.2a. The test setup includes half-lengths of the joining beams and columns, based on the assumption that the points of inflection in the joining beams and columns under seismic loading lie at their midpoints. From the free body diagram of the joint panel in Figure 6.2b, with the beam moments at the joint face represented through
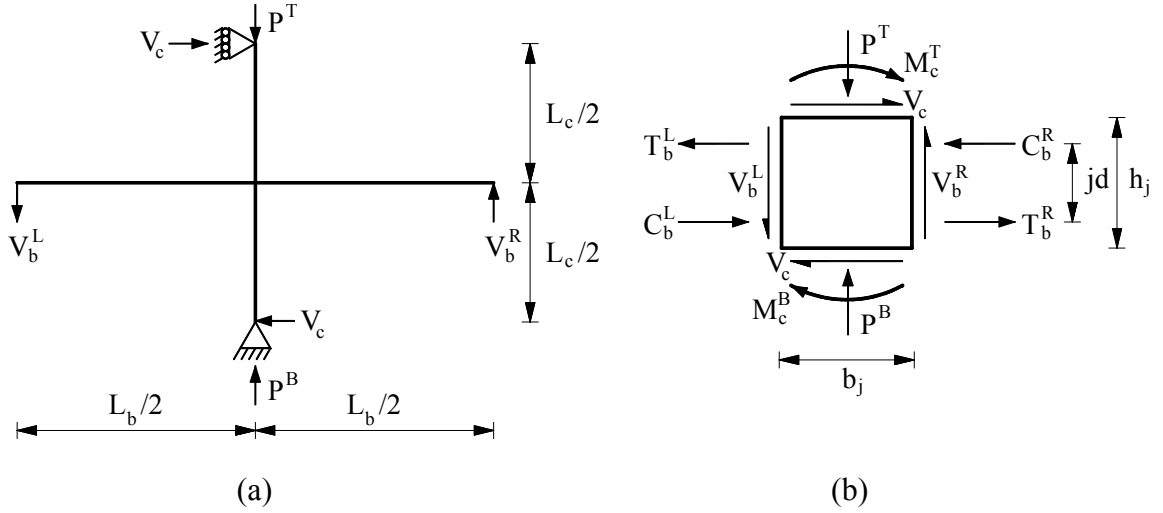
Figure 6.2 Free body diagrams of: (a) a typical interior beam-column joint test setup and (b) its joint panel.

tension and compression couples, and noting that there is no axial load on the beams, the joint shear is

$$V_{jh} = T_b^L + T_b^R - V_c \qquad (6.1)$$

in which T_b^L and T_b^R are the tension forces acting on the left and right faces of the panel (*i.e.*, the tension forces in the left and right beam longitudinal reinforcement), respectively, and V_c is the column shear force. The column shear can be measured easily by a load cell that is attached at the column top or can be calculated using the equilibrium of forces given the beam-end actuator forces. The tension forces, T_b^L and T_b^R, can be calculated from strain gage measurements, which requires a constitutive model that can accurately predict the stress in the steel. This approach is seldom used due to its impracticality and difficulty [Shiohara, 2001]. Instead, the tension forces, T_b^L and T_b^R, are expressed in terms of the beam moments at the joint face, M_b^L and M_b^R; and the

internal moment arm, jd, which is assumed constant throughout the test (superscripts L and R refer to left and right, respectively). The joint shear can then be rewritten as

$$V_{jh} = \frac{M_b^L}{jd} + \frac{M_b^R}{jd} - V_c.$$ (6.2)

If the beam moments at the joint face and the column shear are calculated from the applied shear forces on the left and right beams, V_b^L and V_b^R, then the joint shear is

$$V_{jh} = \left(V_b^L + V_b^R\right) \cdot \left(\frac{L_b - b_j}{2jd} - \frac{L_b}{2L_c}\right)$$ (6.3)

where L_b is the total length of the left and right beams, b_j is the width of the joint panel, and L_c is the total length of the top and bottom columns. Then, the joint shear stress is given by

$$\tau_{jh} = \frac{V_{jh}}{A_{jh}}$$ (6.4)

where A_{jh} is the joint area, which can be calculated, for example, using Section 21.5.3 of ACI 318-05 [ACI Committee 318, 2005]. Joint shear stress can be normalized by either $\sqrt{f_c'}$ or f_c':

$$\bar{\tau}_{jh} = \frac{\tau_{jh}}{\sqrt{f_c'}}$$ (6.5a)

$$\bar{\tau}_{jh} = \frac{\tau_{jh}}{f_c'}$$ (6.5b)

where f_c' is the concrete compressive strength. Both Eq. 6.5a and Eq. 6.5b have been used in the literature; the first suggests that the joint shear strength is proportional to the
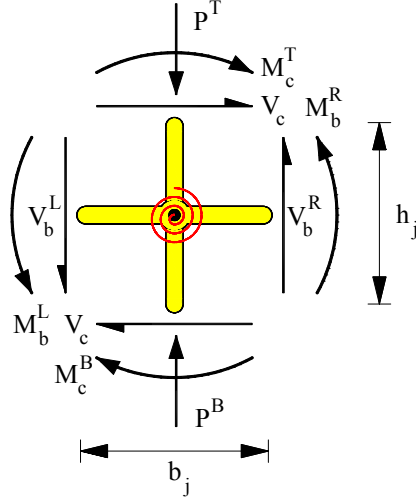
Figure 6.3 Free body diagram of the scissors model.

concrete tensile (or splitting) strength, whereas the second implies that the shear strength is proportional to the compressive strength [Walker, 2001].

Joint shear strain, γ_j, is defined as the change in the angle between the two initially perpendicular edges of the panel zone.

6.3.2 Moment-Rotation Relationship of the Panel Zone

Consider the scissors model [Alath and Kunnath, 1995] representation of the joint panel in Figure 6.2b, with the free body forces in Figure 6.3. The moment at the rotational spring expressed in terms of the shear forces on the beams is

$$M_j = \left(V_b^L + V_b^R\right)\frac{L_b}{2}. \tag{6.6}$$

If Eq. 6.3 is substituted into Eq. 6.4, the resulting equation is solved for the sum of the shear forces on the beams, and the sum is substituted into Eq. 6.6, then the moment transferred through the rotational spring can be expressed in terms of the joint shear stress and sectional dimensions

$$M_j = \tau_{jh} A_{jh} \frac{1}{\dfrac{1 - b_j / L_b}{jd} - \dfrac{1}{L_c}}. \tag{6.7}$$

The relative rotation of the two rigid links that constitutes the scissors model represents the change in the angle between the two adjacent edges of the panel zone. Hence, the rotation of the rotational spring equals the joint shear strain

$$\theta_j = \gamma_j. \tag{6.8}$$

Equations 6.7 and 6.8 can be used to convert the τ_{jh}-γ_j relationship into the M_j-θ_j relationship for the scissors model proposed by Alath and Kunnath [1995]. The formulations that include all possible joint configurations (*i.e.*, interior and exterior joints, and interior and exterior top floor joints) to convert the joint shear stress, τ_{jh}, into the moment transferred through the rotational spring, M_j, are given in Appendix A for all the models used later in the analysis.

6.3.3   Panel Zone Constitutive Model

To implement the constitutive relationship for the panel zone in a finite element-based structural analysis platform, one must define a backbone curve for the envelope and a hysteresis rule for the cyclic response. Previous experimental research on the seismic performance of the beam-column joints that have no transverse reinforcement in the panel zone [*e.g.*, Beres *et al.*, 1996; Walker, 2001; Alire, 2002; and Pantelides *et al.*, 2002] has revealed that the joint shear stress-strain response typically has a degrading envelope and a highly pinched hysteresis. Hence, a constitutive model that has a multi-linear envelope exhibiting degradation and a tri-linear unloading-reloading path representing a pinched hysteresis (see Figure 6.4) is implemented in this study. The
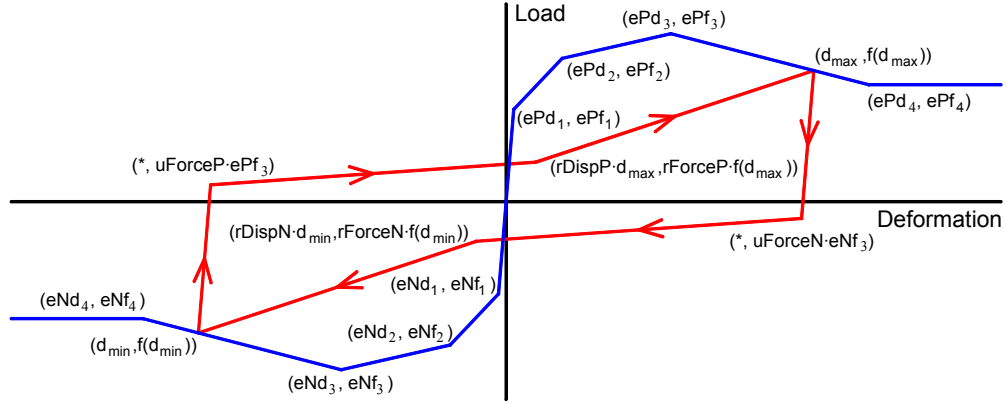
Figure 6.4 Constitutive model proposed by Lowes and Altoontash [2003].

general form of this model was proposed by Lowes and Altoontash [2003], but its control points are defined herein. The envelope (positive or negative) consists of a quad-linear curve that connects four key points starting from the origin and a constant segment that follows the fourth point. The hysteresis rule is defined by a tri-linear unloading-reloading path: (1) the model unloads with the initial stiffness until the force reaches a fraction of the strength; (2) thereafter, points to the pinching point that is defined as a fraction of the maximum previous deformation and the corresponding force; and (3) upon reaching the pinching point, aims to the peak point. The model can also take into account the cyclic degradation of unloading and reloading stiffness and strength [Lowes and Altoontash, 2003].

6.3.4   The Effect of Bond-Slip on the Joint Shear Stress

The typical practice in non-seismic building construction of terminating the beam bottom reinforcement within the beam-column joints with a short embedment length results in bond-slip and a reduced positive beam moment capacity, as explained above. This in turn reduces the joint shear (stress) as can be seen in Eq. 6.2. The joint shear stress-strain

relationship, if symmetric (*i.e.*, has the same positive and negative envelope) owing to the identical beams to the left and right of the joint, preserves its symmetric nature for interior joints. However, it does not remain symmetric for exterior joints, even if it is symmetric when only the joint shear deformations are considered. The constitutive model selected for the panel zone (see Figure 6.4) is sufficiently flexible that it can also represent the anti-symmetric joint shear stress-strain envelope. Bond-slip due to insufficient anchorage of the beam bottom reinforcement can be taken into account by utilizing such a constitutive model with a reduced envelope (only the positive envelope is reduced for exterior joints). Experimental studies suggest that bond-slip causes additional rotation at the beam-ends (at the joint face). However, it has been argued [Leon, 1989] that this additional rotation measured in laboratory tests is largely due to the lack of horizontal restraint at the ends of the beams away from the joint in typical beam-column joint specimens. Hoffmann *et al.* [1992] noted during tests of continuous indeterminate frames that the bar slip is very small and usually difficult to detect visually. Hence, the additional rotation at the beam-ends (apart from the additional joint rotation, which is accounted for) due to bond-slip is neglected.

6.4 Validation of Joint Model by Experimental Tests

To validate the joint model described above for finite element analysis of GLD RC frames, test data from two experimental programs involving RC beam-column test specimens that have no transverse shear reinforcement in the panel zone were utilized [Walker, 2001; Pantelides *et al.*, 2002]. These test programs considered interior and exterior joints, respectively. Information about the experimental tests highlighting important details required in the joint modeling process is summarized below. The

performance of four different representations of the beam-column joints in reproducing experimental force-drift behavior is assessed.

6.4.1 Walker [2001] — Interior Beam-Column Joints

Walker [2001] tested seven RC interior beam-column joints that are representative of joints in frames constructed prior to 1970 under reversed cyclic loading. Two test series were carried out to study the influence of joint shear stress demand and displacement history on the seismic response. The first series consisted of four nominally identical specimens with a target joint shear stress of $0.14 f_c'$ ($0.82\sqrt{f_c'}$ MPa; $9.9\sqrt{f_c'}$ psi), while the second series consisted of three nominally identical specimens with a target joint shear stress of $0.22 f_c'$ ($1.29\sqrt{f_c'}$ MPa; $15.6\sqrt{f_c'}$ psi). The two levels of joint shear stress represent the averages of the joint shear stress demands in RC buildings constructed prior to 1967 and between 1967 and 1979, respectively. Four displacement histories (designated PEER, CD15, CD30, and PADH) were used in testing the specimens (see Figure 6.5). The specimens were identified with the name of the applied displacement history and a two-digit extension representing the target joint shear stress (*e.g.*, PEER-14).

None of these specimens had any transverse shear reinforcement in the panel zone. To study the specific influence of this deficient reinforcing detail, other problematic reinforcing details typical in GLD RC frames were not considered in Walker's tests. In particular, the beam bottom bars were continuous; the strong column-weak beam criterion was satisfied (the column-to-beam moment capacity ratio was kept between 1.5 and 1.8); and the transverse shear reinforcement for beams and columns were designed to satisfy the requirements of ACI 318-99 [ACI Committee 318, 1999].
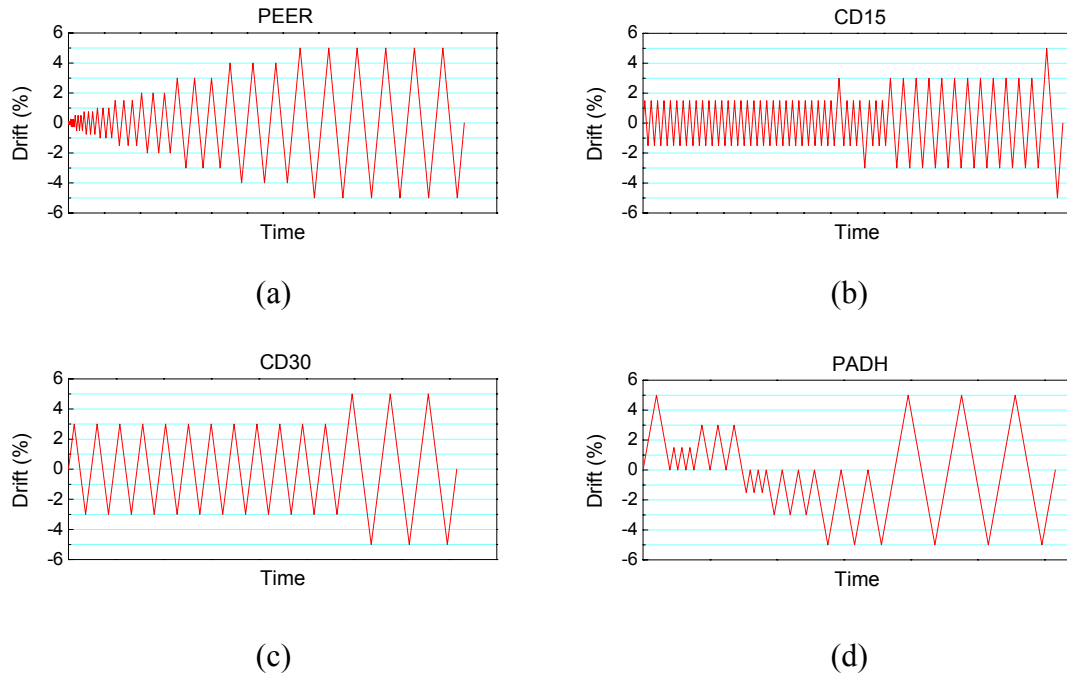
Figure 6.5 Displacement histories used in testing the Walker [2001] specimens: (a) PEER, (b) CD15, (c) CD30, and (d) PADH.

The specified compressive strength of the concrete was 34 MPa (5,000 psi), whereas the design steel yield strength was 462 MPa (67,000 psi). The axial load applied on the column was $0.1f'_c A_g$ (641 kN; 144 kip) where A_g is the gross area of the column section. Figure 6.6 shows the reinforcing steel layouts for the Test Series 14 and Test Series 22, as well the support conditions and the loading points.

P

127 mm

1,067 mm

1,067 mm

A   A

B

B

Δ   Δ

38 mm clear cover
#4 (13 mm) @ 89 mm
hoops and crossties - Red

406 mm

457 mm

A-A

4#7 (22 mm) corner - Red
4#6 (19 mm) middle - Red

508 mm

406 mm

B-B

4#7 (22 mm) - Red

4#5 (16 mm) - Red

1,829 mm   1,829 mm

203 mm   203 mm

(a)

P

127 mm

1,067 mm

1,067 mm

A   A

B

B

Δ   Δ

38 mm clear cover
#4 (13 mm) @ 89 mm
hoops and crossties - Red

406 mm

457 mm

A-A

4#9 (29 mm) corner -
Silver (PEER & PADH)
Green (CD30)
4#8 (25 mm) middle -
Silver (beam face)
Red (joint face)

508 mm

406 mm

B-B

6#7 (22 mm) top &
4#7 (22 mm) bottom -
Silver (PEER & PADH)
Green (CD30)

1,829 mm   1,829 mm

203 mm   203 mm

(b)

Figure 6.6 Reinforcing steel layouts for the Walker [2001] specimens: (a) Test Series 14 and (b) Test Series 22 (1 in. = 25.4 mm).

Table 6.1 Pantelides *et al.* [2002] test matrix.

Test Unit	Bottom Bar Anchorage mm (in.)	Axial Load Level $f'_c A_g$	Axial Load kN (kip)
1	150 (6)	0.10	547 (123)
2	150 (6)	0.25	1,370 (307)
3	360 (14)	0.10	560 (126)
4	360 (14)	0.25	1,410 (316)
5	180° hook	0.10	525 (118)
6	180° hook	0.25	1,310 (294)

6.4.2 Pantelides *et al.* [2002] — Exterior Beam-Column Joints

Pantelides *et al.* [2002] tested six RC exterior beam-column joints that are representative of joints in frames constructed prior to 1970 under reversed cyclic loading. They studied the influence of beam bottom bar anchorage and column axial load level on the seismic response. Anchorage of the beam bottom bars was provided by three different reinforcing details. In two specimens, the beam bottom bars were extended 150 mm (6 in.) into the joint, which is the typical practice in GLD RC frames. In another two specimens, the beam bottom bars were extended all the way (360 mm; 14 in.) into the joint. In the last two specimens, the beam bottom bars were bent up into the joint with a 180° hook. Two levels of axial load ($0.10 f'_c A_g$ and $0.25 f'_c A_g$) were studied for each of the three details. The test matrix for this series is given in Table 6.1.

All six specimens were nominally identical except for the beam bottom bar anchorage detailing. Figure 6.7 shows the reinforcing steel layout for Test Units #1 and #2, along with the support conditions and the loading point. The specimens were designed with concrete having a compressive strength of 28 MPa (4,000 psi) and Grade 60 reinforcement. The specimens did not have any joint reinforcement. The transverse
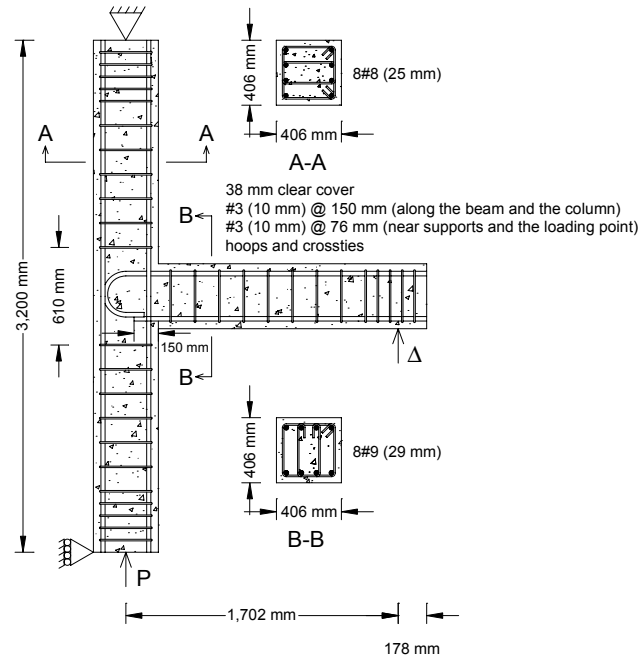
Figure 6.7 Reinforcing steel layout for the Pantelides *et al.* [2002] Test Units #1 and #2
(1 in. = 25.4 mm).

shear reinforcement for beams and columns did not satisfy the requirements of ACI
352R-91 [ACI-ASCE[b] Committee 352, 1991]. Both details are typical in GLD RC
frames. In contrast, the strong column-weak beam criterion was satisfied (the column-to-
beam moment capacity ratio was between 1.9 and 2.1). The displacement history applied
in testing the specimens is given in Figure 6.8.

6.4.3 Finite Element Structural Modeling

Figure 6.9 shows the finite element models of the two sets of beam-column specimens
developed for analysis by OpenSees. Concrete and steel properties reported in the test
programs [Walker, 2001; Pantelides *et al.*, 2002], rather than specified values used to
design the specimens, were incorporated into the finite element models. Cover and core

---

[b] ASCE stands for American Society of Civil Engineers.
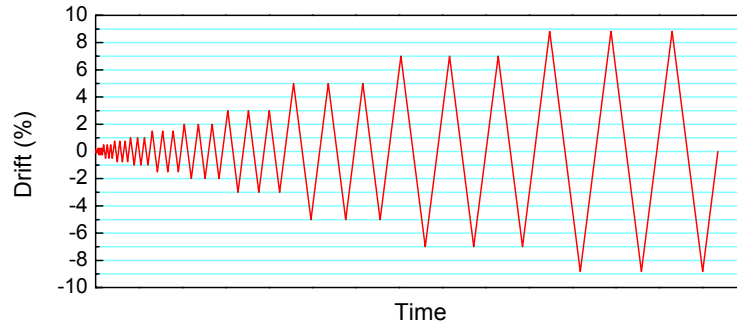
Figure 6.8 Displacement history used in testing the Pantelides *et al.* [2002] specimens.

concrete properties were calculated using the modified Kent and Park model [Park *et al.*, 1982], while steel properties were represented through a bilinear steel model with strain hardening in the range of 1 to 2%, based on material tests [Walker, 2001; Pantelides *et al.*, 2002]. Concrete cover loss was taken into account in all cases. Concrete and steel properties both are given in Tables B1 to B4 in Appendix B, as they are implemented in OpenSees in terms of the parameters that define the *Concrete01* and *Steel01* uniaxial stress-strain relationships, respectively.

Four different representations of the beam-column joints were considered. The candidate representations were the conventional rigid joint model (*i.e.*, centerline model), the scissors model without rigid end zones (*i.e.*, single rotational spring), the scissors model with rigid end zones [Alath and Kunnath, 1995], and the model proposed by Altoontash [2004], which already has been implemented in OpenSees by its developers as the *Joint2D* element. The conventional rigid joint assumption was included to differentiate the improvements that the other models might offer. A snapshot of all four models is given in Figure 6.10.

(a)

(b)
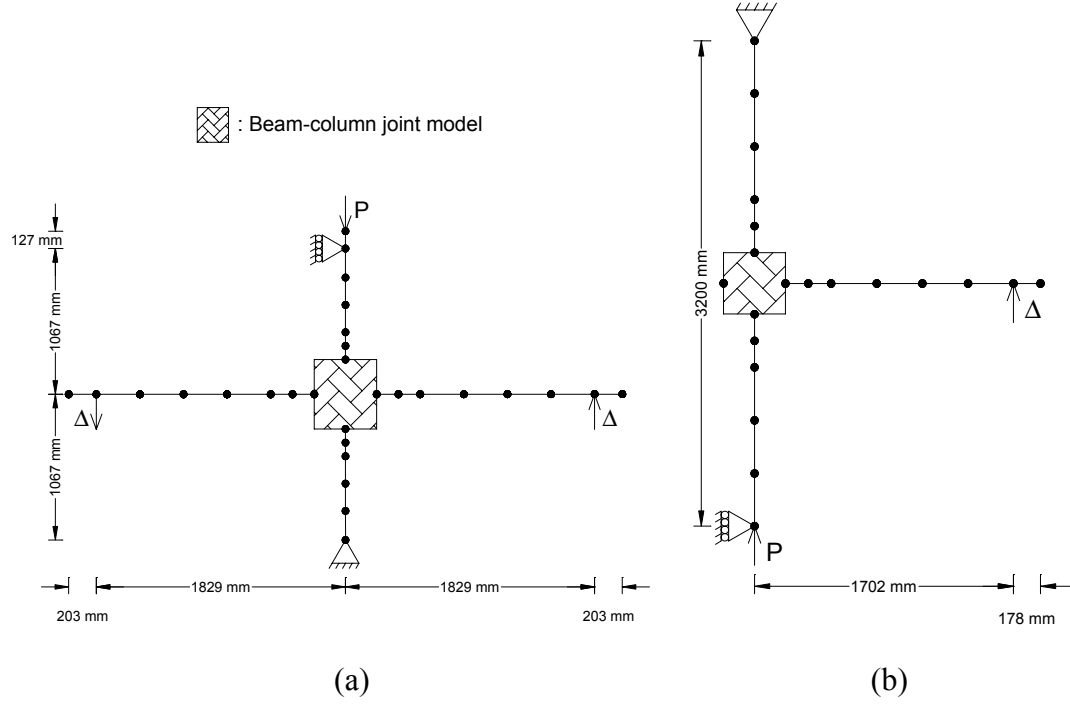
Figure 6.9 OpenSees models of: (a) the Walker [2001] and (b) the Pantelides *et al.* [2002] specimens (1 in. = 25.4 mm).

(a)   (b)   (c)   (d)
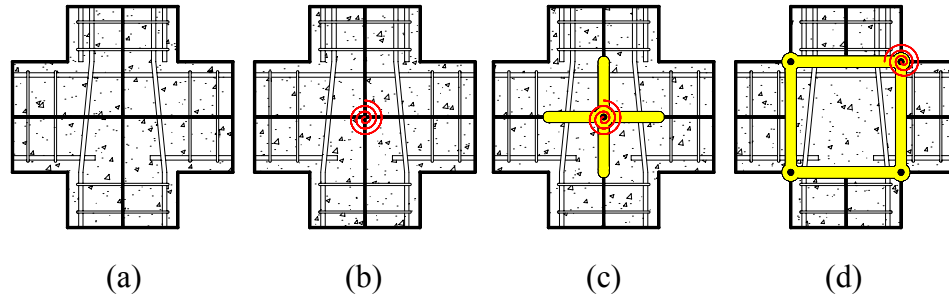
Figure 6.10 Snapshot of all the models used in Section 6.4.3: (a) conventional rigid joint model, (b) scissors model without rigid end zones, (c) scissors model with rigid end zones, and (d) *Joint2D* model.

Both Walker [2001] and Pantelides *et al.* [2002] identified performance levels corresponding to particular joint damage states (*e.g.*, joint cracking, beam yielding, concrete spalling). These performance levels, which were reported in terms of $\bar{\tau}_{jh}$ and γ_j among other performance parameters, formed the basis for setting the four key points

required to define the backbone of the shear stress-strain relationships. These four points $\left(\bar{\tau}_{jh}, \gamma_j\right)$ for each specimen considered in this study are given in Appendix B. Table B.5 presents the values of $\bar{\tau}_{jh}$ and γ_j with corresponding damage states for the Walker [2001] specimens. Table B.6 presents similar information for the Pantelides *et al.* [2002] specimens. It was possible to pick the values of $\bar{\tau}_{jh}$ and γ_j that represent the experimental envelopes more accurately for the Pantelides *et al.* [2002] specimens since $\bar{\tau}_{jh}$ and γ_j were reported for each loading cycle rather than at particular damage states. The internal moment arm values used in calculating the experimental joint shear stress for the Test Series 14 and Test Series 22 (of Walker [2001]) were 411 mm (16.2 in.) and 378 mm (14.9 in.), respectively, while that for the Pantelides *et al.* [2002] specimens was identified as 303 mm (11.9 in.). The $M_j\text{-}\theta_j$ relationships were represented through the constitutive model given in Figure 6.4, which had already been implemented in OpenSees as the *Pinching4* material. The hysteresis rules were defined through simple definitions of the unloading and pinching points, as given in Section 6.3.3. The following parameters were used in setting the hysteresis rules:

$$uForceP = uForceN = -0.10 \qquad (6.9a)$$

$$rForceP = rDispP = rForceN = rDispN = 0.15. \qquad (6.9b)$$

The cyclic degradation of stiffness and strength was not considered in this study.

6.4.4 Comparisons of Predictions with Experimental Responses

Finite element models were developed for all seven specimens tested by Walker [2001] and for the first four specimens tested by Pantelides *et al.* [2002]. Test Units #5 and #6 (of Pantelides *et al.* [2002]) were not considered because their experimental force-drift

responses were similar to those of Test Units #3 and #4, respectively. Figures 6.11 to 6.14 compare the simulated force-drift responses with the experimental counterparts for Specimens PEER-14 and PEER-22 (of Walker [2001]) and Test Units #1 and #3 (of Pantelides *et al.* [2002]); comparisons of predictions with experimental responses for the other specimens are given in Appendix C. Each figure shows distinct comparisons of the analytical responses from the four joint models with the experimental responses. The conventional rigid joint model is inadequate in all cases for reproducing the highly pinched experimental responses, which are characteristic of shear-dominated behaviors [Stevens *et al.*, 1991], making the importance of accounting for joint shear and bond-slip in modeling of GLD RC frames evident. Significant improvements to the rigid joint response from all other models are evident from Figures 6.11 to 6.14 (and Figures C.1 to C.7). Thus, the following comparisons and conclusions pertain to all joint models except the rigid joint model.
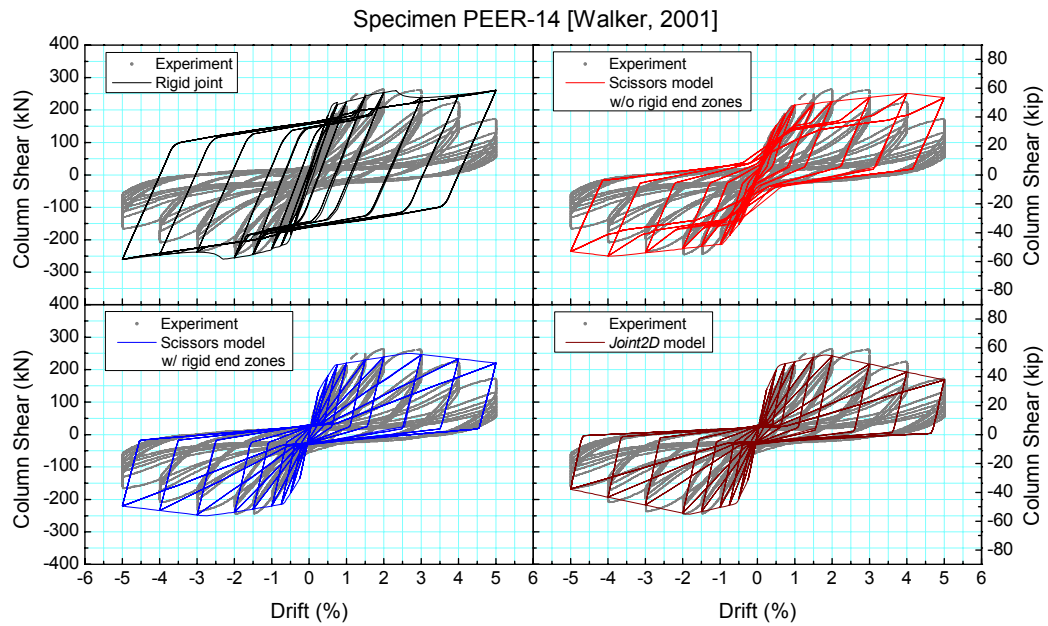
Figure 6.11 Comparisons of the simulated force-drift responses with the experimental response for the Walker [2001] Specimen PEER-14.
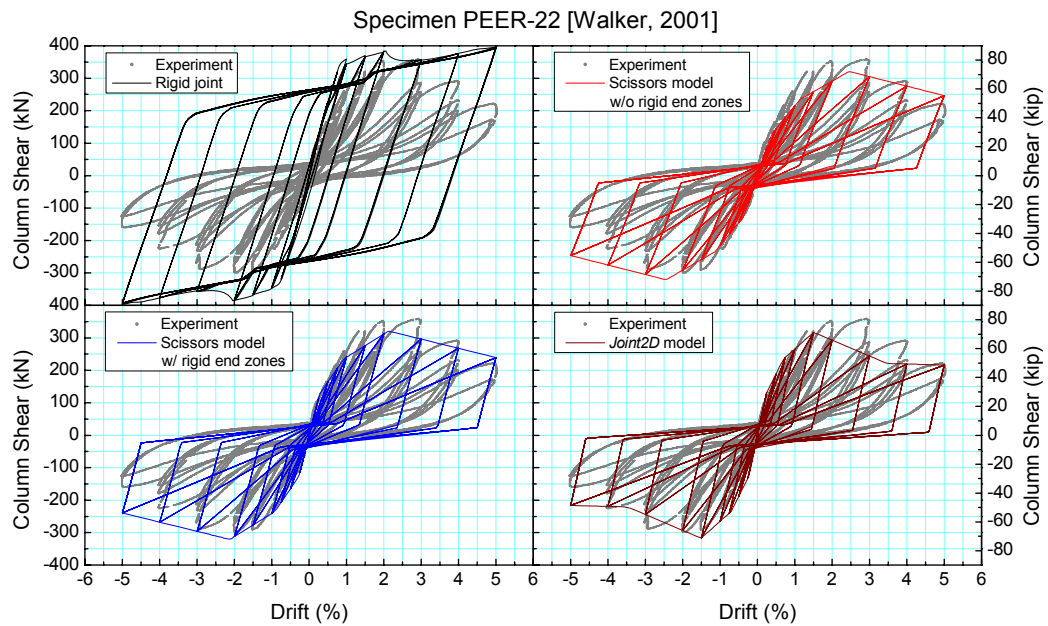
Figure 6.12 Comparisons of the simulated force-drift responses with the experimental response for the Walker [2001] Specimen PEER-22.
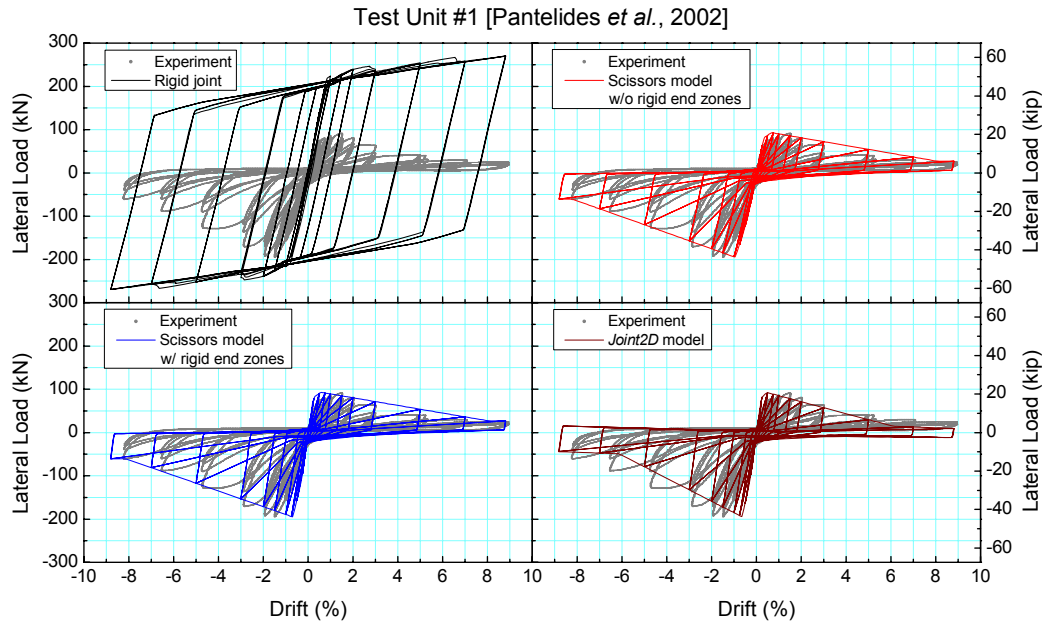
Figure 6.13 Comparisons of the simulated force-drift responses with the experimental response for the Pantelides *et al.* [2002] Test Unit #1.
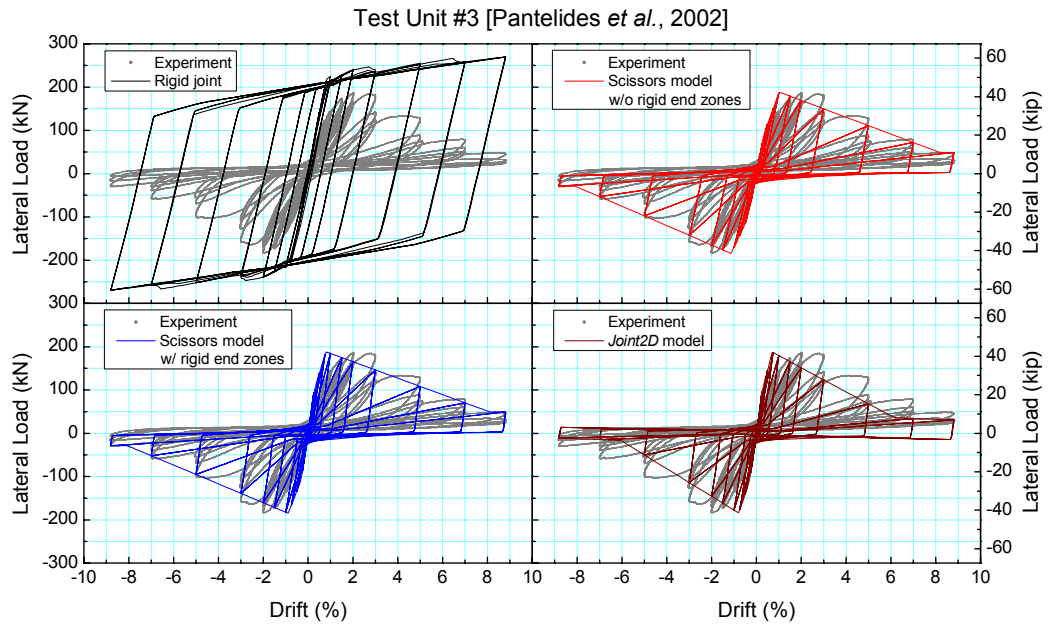
Figure 6.14 Comparisons of the simulated force-drift responses with the experimental response for the Pantelides *et al.* [2002] Test Unit #3.

The envelopes to the simulated force-drift responses of the Walker [2001] specimens showed good agreement with the experimental data (see Figures 6.11 and 6.12, and Figures C.1 to C.5). The discrepancies that exist between the simulated and experimental envelopes, particularly for Specimens CD15-14 and PADH-14 (see Figures C.1 and C.3, respectively), are attributed to the definition of backbone of joint shear stress-strain relationships, as the performance points $\left(\bar{\tau}_{jh}, \gamma_j\right)$ corresponding to particular damage states do not necessarily replicate the experimental shear stress-strain envelope. The degradation in backbone curves observed in the tests was captured by the finite element model. The simulated cyclic responses were also in good agreement with the experimental data (see Figures 6.11 and 6.12, and Figures C.1 to C.5). Hysteretic energy dissipated during the experimental loading cycles was represented well and the pinching point was captured quite well except for a few cases with the scissors model without rigid end zones (*i.e.*, Specimens PEER-14, CD30-14, and PADH-14). Since the cyclic degradation of stiffness and strength was not modeled, it was not possible to capture cyclic degradation effects observed on the specimens subjected to the CD15 and CD30 displacement histories (see Figures 6.5b and 6.5c, respectively), which consist of many constant-amplitude reversed cycles (see Figures C.1, C.2, and C.4). However, these effects did not seem to alter the subsequent responses significantly.

The Pantelides *et al.* [2002] test series included specimens with discontinuous beam bottom bars, which enabled the model to be tested for its ability to simulate bond-slip in addition to joint shear. The experimental response of Test Unit #3 and #4 were essentially symmetric (see Figures 6.14 and C.7, respectively) and the beam section was symmetric. This indicates that a development length of 360 mm (14 in.) provided

adequate anchorage to the beam bottom bars and prevented bond-slip. The experimental responses of Test Units #1 and #2, however, were unsymmetric (see Figure 6.13 and C.6, respectively). Every other parameter except the beam bottom bar anchorage was the same for Test Units #1 and #3, and Test Units #2 and #4, so the differences between the corresponding experimental responses (see Figures 6.13 and 6.14, and Figures C.6 and C.7, respectively) can only be due to the bond-slip behavior resulting from insufficient positive beam bar anchorage. As noted previously, this bond-slip resulted in reduced positive force-drift envelopes. The effect of axial load on beam-column joint response was also studied in this test series. No significant change was observed between the experimental responses of Test Units #1 and #2, and Test Units #3 and #4.

All simulated force-drift responses of the Pantelides *et al.* [2002] specimens (see Figures 6.13 and 6.14, and Figures C.6 and C.7) correlate well with the experimental data except the distortion observed in simulations with the *Joint2D* model for higher axial load levels (*i.e.*, Test Units #2 and #4). The effect of bond-slip in Test Units #1 and #2 was captured (see Figures 6.13 and C.6, respectively). The overall response and the hysteretic energy dissipated during the experimental loading cycles were represented well for all specimens.

6.5 Seismic Demand Assessment of Existing GLD RC Frames

Experimental data to define the backbone curves for the joint shear stress-strain relationships are not available for general configurations of GLD frame joints. Nor is there a theoretical tool for this purpose (*e.g.*, the MCFT has been shown to be inadequate to predict the panel shear stress-strain behavior of GLD RC frame joints [LaFave and Shin, 2005]). Since the seismic demand assessment of existing GLD frames requires a

constitutive relationship for the panel zone for each beam-column joint in the actual frame, the coordinates of the four key points (see Figure 6.4) that define the panel zone backbone for a general beam-column joint in a frame are derived below.

6.5.1 Defining the Backbone of the Panel Zone

Experimental studies (see Table 6.2) of typical details of GLD RC frame beam-column joints indicate that the four key points of the backbone curve for the panel zone (see Figure 6.4) correspond to joint shear cracking, reinforcement yielding, joint shear strength/adjoining beam or column capacity, and residual joint strength, respectively.

Joint shear stresses corresponding to the shear cracking of the panel zone were reported to be in the range of $0.21 - 0.69\sqrt{f_c'}$ MPa ($2.5 - 8.3\sqrt{f_c'}$ psi), increasing with higher axial loads. Uzumeri [1977] showed that the following ACI equation (*cf.* Eq. 6.5a) predicts the cracking shear (in $\sqrt{\text{psi}}$ units) well for beam-column joints with no shear reinforcement:

$$\left(\overline{\tau}_{jh}\right)_{cr} = 3.5\sqrt{1 + 0.002\left(N_u / A_{jh}\right)} \tag{6.10}$$

where N_u is the axial load (N_u / A_{jh} in psi). This equation, when used to estimate the experimental cracking shear stresses reported in Table 6.2, resulted in comparable values, and therefore was used to define the ordinate of the first point on the backbone.[c]

---

[c] The internal moment arm, jd, in Eq. 6.7 was computed from $7/8 \cdot \left\lfloor \left(d^+ + d^-\right)/2 \right\rfloor$ where d^+ and d^- are the distances to the bottom and top reinforcing bars from the opposite sides, respectively.

Table 6.2 Experimental database utilized in defining the backbone of the panel zone for GLD RC beam-column joints ($10\sqrt{\text{psi}} = 0.83\sqrt{\text{MPa}}$).

Reference	Joint Reinf.	Beam Bottom Bar	Axial Load $f'_c A_g$	$(\bar{\tau}_{jh})_{cr}$ $\sqrt{\text{psi}}$	$(\bar{\tau}_{jh})_{max}$ $\sqrt{\text{psi}}$	$(\gamma_j)_{cr}$ 10^{-3} rad	$(\gamma_j)_y$ 10^{-3} rad	$(\gamma_j)_{max}$ 10^{-3} rad	$(\gamma_j)_{res}$ 10^{-3} rad	α
Exterior Joints										
Uzumeri [1977]	No	Cont.	0.39	7.6	10.7–11.3					
Beres et al. [1992]	No	Disc.	0.11		5.0–7.5					
	Yes	Disc.	0.11		8.5–9.5					
	No	Disc.	0.39		7.0–9.0					
Pantelides et al. [2002]	No	Disc.	0.10	3.8	5.2	0.40		3.5	> 23	0.47
			0.25	5.8	7.0					0.66
	No	Disc.*	0.10	5.6	10.9	0.47		2.0		
			0.25	8.3	10.6					
	No	Cont.	0.10	2.5–3.1	10.2–10.4	0.13		3.3–4.3	> 55	1.0
			0.25	4.7–4.9	11.1–11.7	0.34		2.3–3.1	> 32	0.94
Interior Joints										
Leon [1990]	Yes	Disc. to Cont.	0	5.6–7.3						
Pessiki et al. [1990] and Beres et al. [1992]	No	Disc.	0.11	7.4	9.0–11.1					0.50
			0.39	7.7–7.9	10.5–12.0					0.50–0.70
	No	Cont.	0.39	6.3–8.2	12.7–13.4					
	Yes	Cont.	0.39	7.8–8.3	11.8–13.6					
Walker [2001]	No[†]	Cont.	0.10	4.1–5.6	8.7–10.2	0.25–0.46	3.3–4.1	9.9–22	42–76	
	No[‡]	Cont.	0.10	4.0–5.2	13.2–14.8	0.34–1.3	5.6–6.3	17–18	50–74	
Shin and LaFave [2004][§]	Yes					$\cong 0.5$	2–10	10–30	30–50	

* Data presented are for the negative backbone.
†, ‡ Data presented are for the Test Series 14 and 22, respectively.
§ Data are from a collection of 26 interior beam-column joint tests from the literature.

89

If the shear failure of the joint does not occur before the adjoining beams/columns reach their ultimate capacity, then the second and the third points on the backbone correspond to yield and ultimate capacities of the beams/columns (for GLD RC frames [*e.g.*, Walker, 2001]). The columns reach their ultimate capacity if the design is a weak column-strong beam, and conversely if the design is a strong column-weak beam. In either case, section analyses were carried out to determine the yield and ultimate moment capacities,[d] which were used to calculate the ordinates of the second and the third points on the backbone; these are summarized in Appendix D. The positive yield moment capacities of the beams were scaled by a factor α, which was reported to vary between 0.4 and 0.7 in previous experimental tests (see Table 6.2), to account for bond-slip. The positive ultimate capacities of the beams then were set equal to the scaled positive yield capacities of the beams.

The ordinate of the fourth point was assumed equal to that of the first point on the backbone, as previous experimental research has revealed that strength degradation occurs once the peak point is attained on the backbone curves of beam-column joints that are typical of GLD construction.

The abscissas of the four key points were based on the available experimental data (see Table 6.2); these joint shear strains $((\gamma_j)_{cr}, (\gamma_j)_y, (\gamma_j)_{max}, (\gamma_j)_{res})$ typically fall within the following ranges: 0.0001–0.0013, 0.002–0.010, 0.01–0.03, and 0.03–0.10 radians.

Based on the previous experimental research that reported joint shear strength $(\bar{\tau}_{jh})_{max}$ (see Table 6.2), the ordinates of the points on the backbone were reduced so as

---

[d] The levels of axial loads on columns were estimated from the finite element simulations.

not to exceed $\left(\bar{\tau}_{jh}\right)_{max}$, when the shear failure of the joint occurs before beams or columns reach their capacities. The joint shear strength falls within the following ranges: 0.42–0.62 $\sqrt{\text{MPa}}$ (5.0–7.5 $\sqrt{\text{psi}}$) for the positive backbone and 0.83–1.00 $\sqrt{\text{MPa}}$ (10.0–12.0 $\sqrt{\text{psi}}$) for the negative backbone; of exterior beam-column joints, while that for the interior beam-column joints falls within the 0.75–1.00 $\sqrt{\text{MPa}}$ (9.0–12.0 $\sqrt{\text{psi}}$) range.

6.5.2   Seismic Demand Analyses of GLD RC Frames

Seismic demand assessments of GLD RC frames that are representative of building construction in the CEUS (identified in Chapter 4) were performed using the finite element models of the frames[e] that incorporate the new beam-column joint model (adapted to the scissors model with rigid end zones). The lower bound values of joint shear strength (identified above) were utilized together with the following joint shear strains: 0.0005, 0.005, 0.02, and 0.08, and a bond-slip factor $\alpha = 0.5$ in defining the backbone curves of the panel zones for beam-column joints in the frames. The seismic demands on the frames were assessed through NTHAs utilizing Wen-Wu synthetic UHGM generated for Memphis, TN, which were presented in Chapter 3.[f]

The three-story GLD RC frame is a weak column-strong beam design, and its expected failure mode is a soft-story collapse. The soft-story behavior produces very high interstory drifts in the first story of the frame with rigid joints (conventional rigid joint model with rigid end zones)[g]. The first story of the frame with the proposed joint model

---

[e] All slab bars within the effective width of the slab were considered.
[f] Section 7.2.1 presents a comprehensive assessment of the seismic demand analysis, including a discussion of some of the numerical issues that arise when using NTHA to define failure. Here, the purpose is simply to illustrate the impact of joint modeling on structural response.
[g] Eigenvalue analyses yielded fundamental periods of 1.07 s when the finite element model of the three-story frame incorporated the new joint model and 1.00 s when rigid joint was assumed.

also sustains large deformations, but the upper stories experience drifts that are larger than those in the rigid-joint frame. Thus, the roof drifts in the frame with the proposed joint model are higher due to the increased flexibility of the frame, but the maximum interstory drifts are less than those in the rigid-joint frame. This behavior is reflected in Figure 6.15a, which illustrates the seismic demand (measured in terms of θ_{max} vs. $S_a(T_1)$, as presented in Chapter 5). Since the rigid joint assumption precludes any damage at the joint, it is not realistic in the presence of weak column-strong beam behavior and exaggerates the soft-story effect. On the other hand, the rigid joint assumption is plausible for frames designed for seismic effects according to modern building code provisions. Concurrent analyses of a comparable strong column-weak beam frame[h], depicted in Figure 6.15b, revealed that the proposed joint model leads to maximum interstory drifts that are larger than those obtained using a rigid joint model. Should such a frame contain deficient beam-column joints, the damage at those joints, combined with damage localized at the ends of the beams, would worsen the overall behavior of the frame.

---

[h] First three stories of the nine-story frame, which are identical to those of the three-story frame except the columns, were considered as the comparable strong column-weak beam frame.
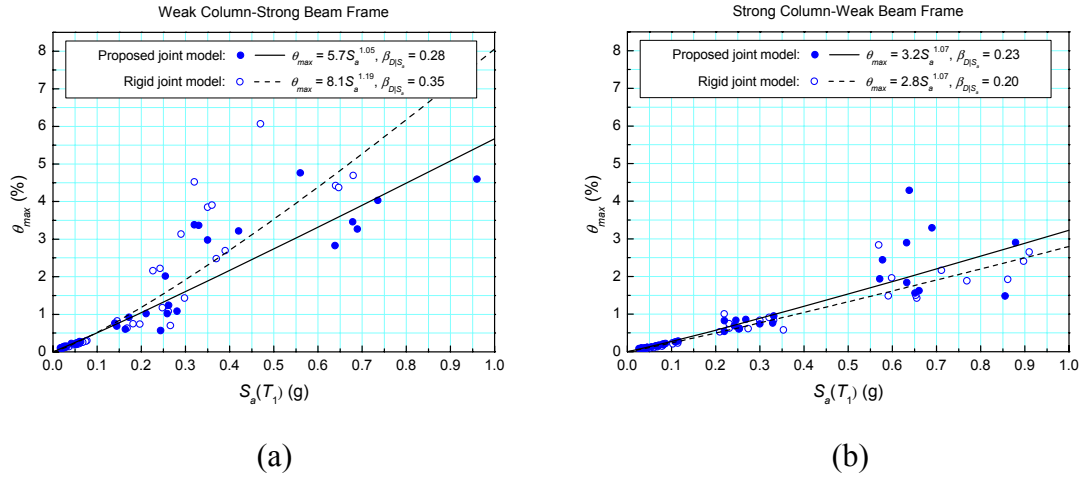
Figure 6.15 Seismic demands on: (a) the three-story GLD RC frame and (b) the comparable strong column-weak beam frame.
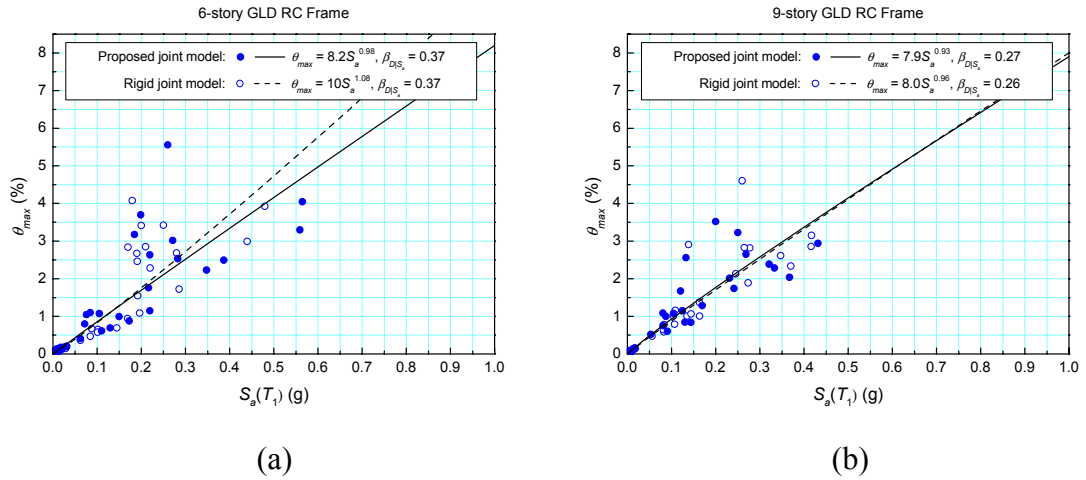
Figure 6.16 Seismic demands on the: (a) six- and (b) nine-story GLD RC frames.

The seismic demand on the six-story GLD RC frame[i], depicted in Figure 6.16a, shows a similar trend as that seen in Figure 6.15a, where the rigid-joint frame model predicts higher maximum interstory drifts than the frame with the proposed joint model. The columns of the top three stories of the six-story frame are weaker than the adjoining

---

[i] Fundamental periods of the six-story frame are 1.76 s with the proposed joint model and 1.60 s with the rigid-joint model.

beams, which leads to soft-story development at the fourth story, where a transition in column size occurs. The rigid-joint model amplifies the damage at this story, whereas the proposed joint model predicts more uniform story drift profiles with maximum interstory drifts usually occurring at the fourth story. On the other hand, the seismic demand on the nine-story GLD RC frame[j], depicted in Figure 6.16b, is comparable to that illustrated in Figure 6.15b. The top three stories of the nine-story frame are typical of weak column-strong beam designs. However, seismic demand at the upper stories of the nine-story frame is not always sufficient to trigger the weak column-strong beam behavior. Consequently, the damage at the joints of the nine-story frame, which is taken into account with the proposed joint model, worsens the behavior of that frame. These comparisons reveal the importance of modeling the joints in GLD RC frames in assessing seismic performance of such frames in regions of low-to-moderate seismicity.

6.6 Summary

A beam-column joint model that accounts for shear and bond-slip in the joints of GLD RC frames was developed, following a review and critical appraisal of existing models. The beam-column joint model was validated using the results from two full-scale experimental RC beam-column joint test series. The model adapted to the scissors model with rigid end zones was sufficiently accurate in simulating the experimental beam-column joint responses. Application of the proposed beam-column joint model, with the formulation for defining the backbone of the panel zone, for seismic demand analyses of three GLD RC frames revealed the importance of modeling the joint behavior accurately in assessing seismic performance of GLD frames.

---

[j] Fundamental periods of the nine-story frame are 2.54 s with the proposed joint model and 2.35 s with the rigid-joint model.

CHAPTER 7

SEISMIC FRAGILITY ASSESSMENT OF GRAVITY LOAD

DESIGNED REINFORCED CONCRETE FRAMES

7.1 Introduction

Current research in the MAE Center is developing quantitative evaluation tools for seismic risk mitigation in the CEUS. This chapter presents a key ingredient of that effort: seismic fragilities for GLD RC frames, which are susceptible to column-sidesway or soft-story mechanisms under earthquake excitation. Seismic fragilities are derived for low-, mid-, and high-rise GLD RC frames (*cf.* Section 4.3) using finite element simulations of the frames. These fragilities are compared to those incorporated in HAZUS and are later used in assessing the seismic vulnerability of the RC frame inventory in the CEUS.

7.2 Performance of GLD RC Frames Subjected to Mid-America Ground Motions

Three-, six-, and nine-story GLD RC frames (identified in Chapter 4) were considered for performance assessment in the following analyses. The uncertainty in structural demand due to the seismic intensity is known to be very large in comparison to other sources of uncertainty in structural demand. Accordingly, the finite element structural models of the frames (described in Chapter 4) that incorporate the new beam-column joint model (developed in Chapter 6) first were implemented using median values of material properties, structural damping, and joint model parameters[a]. The contribution of uncertainties in material and structural properties and structural modeling parameters to

---

[a] Structural parameters are treated as random in Chapter 8. The median and logarithmic standard deviations are found in Table 8.1.

Table 7.1 First three modal periods and effective modal masses of the three-, six-, and nine-story GLD RC frames.

Frame	T_1 (s)	T_2 (s)	T_3 (s)	M_1^*	M_2^*	M_3^*
3-story	1.12	0.36	0.20	87%	11%	2%
6-story	1.88	0.64	0.35	78%	12%	4%
9-story	2.82	0.97	0.54	78%	11%	4%

the overall seismic response and performance of the three frames will be considered subsequently in Chapter 8.

The following three sub-sections present seismic demand analyses of the frames, structural damage and failure mechanisms as identified from the finite element simulations of the frames, and the impact of the choice of ground motion ensembles on performance assessment.

7.2.1   Probabilistic Seismic Demand Analyses

The dynamic properties of the three-, six-, and nine-story frames are presented in Table 7.1. The fundamental periods of 1.12 s, 1.88 s, and 2.82 s, respectively, indicate that the GLD RC frames are flexible, and the first-mode effective modal masses, M^*, of 87%, 78%, and 78%, respectively, indicate that the dynamic behavior of GLD RC frames is first-mode dominant. These results are consistent with the previous research summarized in Chapter 2.

The seismic performance of the frames was assessed through NTHAs utilizing both Wen-Wu and Rix-Fernandez synthetic UHGM for Memphis, TN (presented in Chapter 3) and the effect of different ground motion models on building performance and fragility estimates was examined. Figure 7.1 depicts the seismic demands on the three-, six-, and nine-story GLD RC frames for the Wen-Wu and Rix-Fernandez ground motions

separately. The dynamic analyses did not converge for all accelerograms when the UHGM corresponding to the 2% PE in 50 yr hazard level for soil sites were utilized,[b] indicating that the frames would not be able to withstand some of these high-intensity ground motions; in those cases, the ground motions were scaled downward (with S_a decrements of 0.01 g) to identify the last (θ_{max}, S_a) pair prior to the point at which the solution failed to converge. The solution algorithm, which was presented in Section 4.4, was assumed to also fail if the maximum response of the frame occurred during the 5 s period of free vibration response following the ground motion excitation, which indicated that the solution was diverging (see Figure 7.2).

---

[b] See the following two sub-sections for further details.
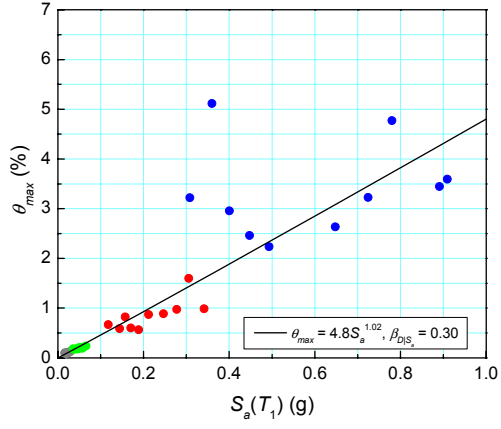
(a) 3-story, Wen-Wu
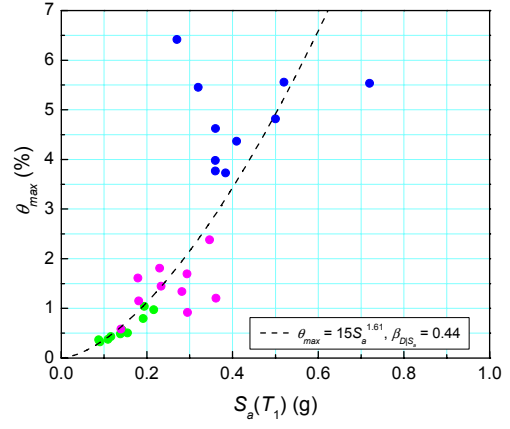
(b) 3-story, Rix-Fernandez
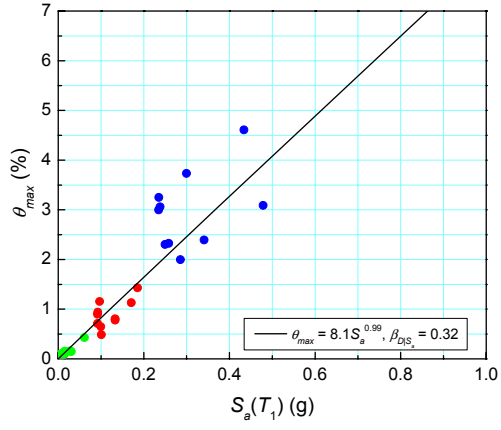
(c) 6-story, Wen-Wu
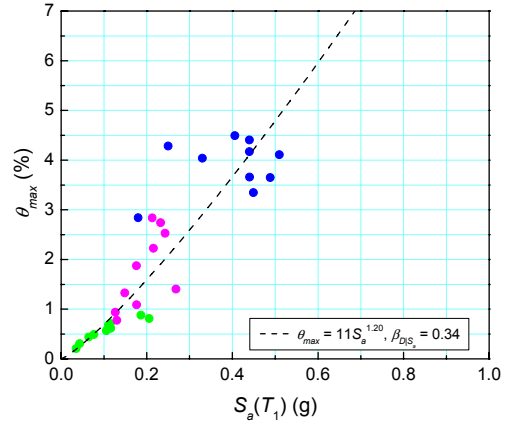
(d) 6-story, Rix-Fernandez
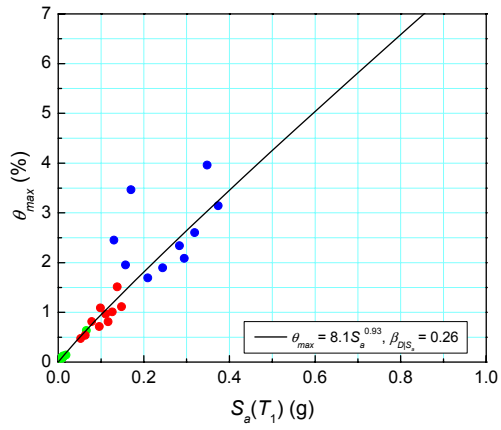
(e) 9-story, Wen-Wu
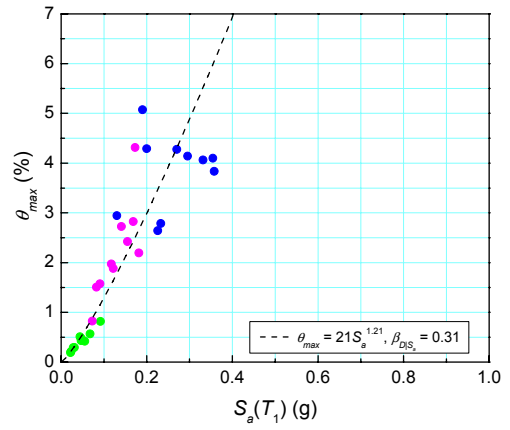
(f) 9-story, Rix-Fernandez

Figure 7.1 Seismic demands on the GLD RC frames for the Wen-Wu and Rix-Fernandez ground motions (color code defined in Figure 3.6).
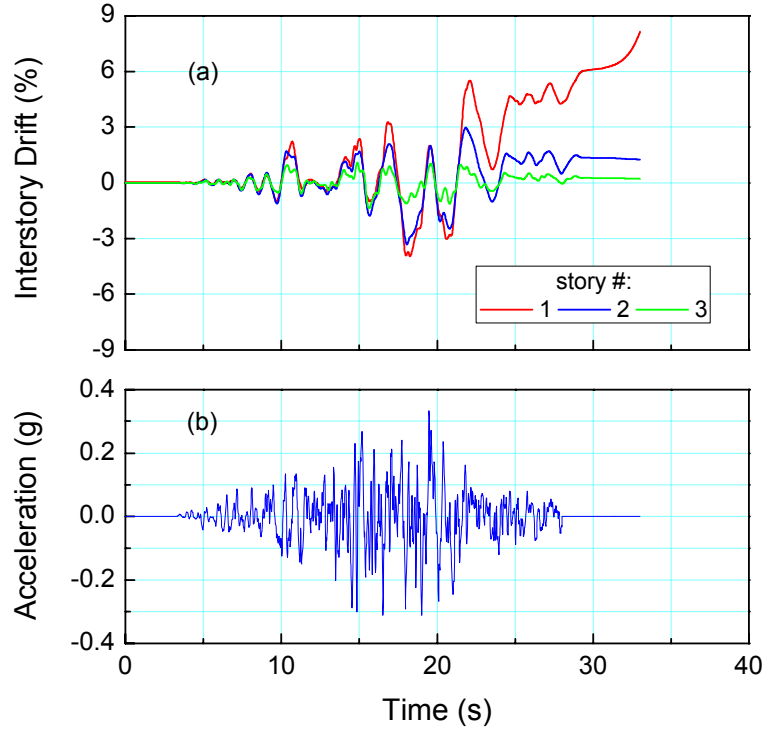
Figure 7.2 (a) Three-story frame response to the scaled (b) Wen-Wu accelerogram #2 from the 2% PE in 50 yr soil ensemble.

The seismic demands on the frames are represented by the probabilistic seismic demand model given in Chapter 5 for the Wen-Wu and Rix-Fernandez ground motions, respectively. For the three-story frame, this leads to:

$$\hat{\theta}_{max} = 4.8 \cdot S_a^{1.02}, \ \beta_{D|S_a} = 0.30; \tag{7.1a}$$

$$\hat{\theta}_{max} = 15 \cdot S_a^{1.61}, \ \beta_{D|S_a} = 0.44. \tag{7.1b}$$

For the six-story frame, one obtains:

$$\hat{\theta}_{max} = 8.1 \cdot S_a^{0.99}, \ \beta_{D|S_a} = 0.32; \tag{7.1c}$$

$$\hat{\theta}_{max} = 11 \cdot S_a^{1.20}, \ \beta_{D|S_a} = 0.34; \tag{7.1d}$$

while for the nine-story frame:

$$\hat{\theta}_{max} = 8.1 \cdot S_a^{0.93}, \ \beta_{D|S_a} = 0.26; \tag{7.1e}$$

$$\hat{\theta}_{max} = 21 \cdot S_a^{1.21}, \ \beta_{D|S_a} = 0.31. \tag{7.1f}$$

In all cases, the median θ_{max} is expressed in percent, %, and S_a is in gravitational units, g. The differences in median drift demands obtained under different ground motion ensembles is one reflection of the epistemic uncertainty in ground motion modeling, as discussed previously in Chapter 3. The impact of these demand differences on seismic performance assessment of the GLD RC frames will be presented subsequently.

7.2.2 Seismic Behavior

7.2.2.1 Three-Story GLD RC Frame

The three-story GLD RC frame is a weak column-strong beam design, where the column-to-beam moment capacity ratios vary within the range of 0.3 to 0.9 except at the first story exterior beam-column joints, where it is 1.2. This frame was not able to withstand two of the Wen-Wu and seven of the Rix-Fernandez accelerograms from the 2% PE in 50 yr soil ensembles. The collapses of this frame occurred due to soft-story formations, which were initiated when the columns reached their moment capacities at various stories while the first story interior joints failed in shear.

The pullout of the beam bottom bars (anchorage failures) was observed at the first two story exterior beams where the bottom bars are embedded into the exterior joints, significantly reducing the positive moment capacities at the exterior joint-ends of those beams. However, pullout of the bottom bars did not occur at the interior beams or interior joint-ends of the exterior beams at any story due to the weak column-strong beam behavior. The imposed earthquake load barely forced the interior joint-ends of the beams

into positive bending (these joints initially were subjected to negative bending due to the gravity loads) before the columns reached their moment capacities or the joints reached their shear strengths. In contrast, the first two story beams reached either their yield or ultimate moment capacities at their interior joint-ends in negative bending. No damage was observed at the top story beams, except where bottom bar pullout occurred at the exterior joint-ends in some cases.

For those high-intensity ground motions in which a solution could be achieved, the three-story frame withstood interstory drifts in excess of 5% without collapse. These drifts were accompanied by significant joint shear deformations. Examples of such behavior were presented in Section 6.4.4.

7.2.2.2   Six-Story GLD RC Frame

The top three stories of the six-story GLD RC frame are identical to the three-story frame and hence behave as weak column-strong beam frames, with the same column-to-beam moment capacity ratios as those given for the three-story frame. In contrast, the first three stories of the six-story frame are strong column-weak beam, with the column-to-beam moment capacity ratios in the range of 1.3 to 2.5. This frame collapsed under one of the Wen-Wu and six of the Rix-Fernandez accelerograms from the 2% PE in 50 yr soil ensembles,[c] due to soft-story failure mechanisms involving the first four stories of the frame. The collapses were initiated when the moment capacities were reached at the base of the first story columns and at the top of the fourth story columns, where the strong column-weak beam criterion was not satisfied. Accordingly, most of the column damage was concentrated at the top three stories.

---

[c] One out of ten accelerograms in the 5% PE in 50 yr Rix-Fernandez ensemble also led to frame collapse.

Significant shear deformations were observed at the first four to five story beam-column joints, with the pullout of the beam bottom bars occurring at the exterior joint-ends of the beams in the same stories. In some cases, the pullout of the beam bottom bars was also observed at the interior joint-ends of the first three story beams, where the strong column-weak beam criterion was satisfied. Under negative bending, the first four to five story beams reached their ultimate moment capacities at their interior joint-ends while the first two story exterior beams reached their yield or ultimate moment capacities at their exterior joint-ends. The maximum interstory drifts in the six-story frame exceeded 4% under some of the 2% PE in 50 yr soil ground motions.

7.2.2.3   Nine-Story GLD RC Frame

The nine-story GLD RC frame is a strong column-weak beam design with the exception of the top three stories, which are identical to the three-story frame. The column-to-beam moment capacity ratios vary within the range of 1.3 to 4.4 at the first six story beam-column joints, while the capacity ratios at the top three story joints are the same as those for the three-story frame. This frame collapsed under one of the Wen-Wu and four of the Rix-Fernandez accelerograms from the 2% PE in 50 yr soil ensembles. Plastic hinges were first developed at both ends of the low six-story beams, essentially forming beam-sidesway mechanisms. The collapses of the frame occurred when hinges formed either at the base of the first story columns or in the columns above the third story, or both, and significant P-Δ effects developed due to the high flexibility of the frame. Significant joint shear deformations and interstory drifts exceeding 4% were also observed in the nine-story frame, as they were for the three- and six-story frames.
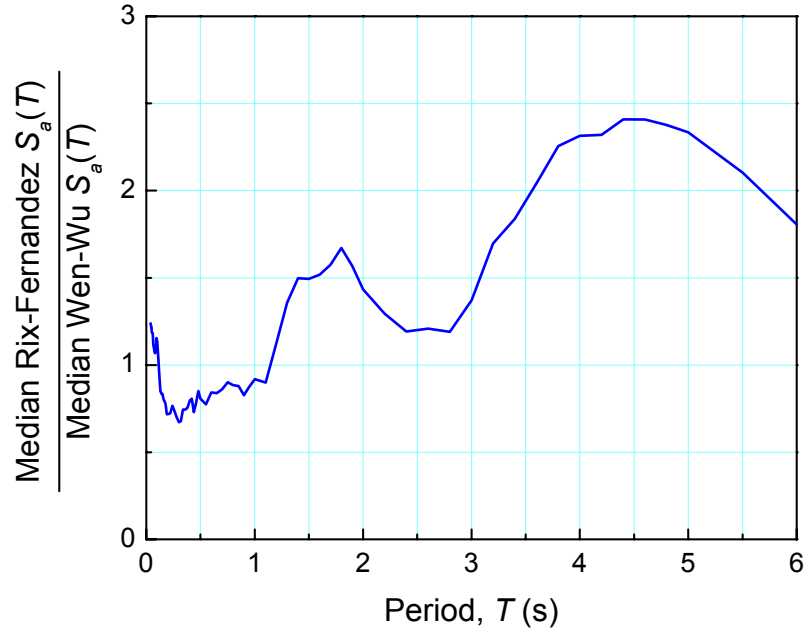
Figure 7.3 Ratio of the median Rix-Fernandez to that of the Wen-Wu 2% PE in 50 yr soil ensembles.

7.2.3   Impact of the Choice of Ground Motion Ensemble

The Rix-Fernandez ground motion ensembles imposed higher median drift demands on the frames than the Wen-Wu ground motion ensembles, as illustrated in Figure 7.1. The differences in amplitude and frequency content between the two sets of ensembles and the sources of such differences in ground motion modeling were previously discussed in Chapter 3. The following discusses the impact of those differences on the finite element structural responses.

Figure 7.3 depicts the ratio of the median Rix-Fernandez response spectrum (S_a) to that of the Wen-Wu spectrum for the 2% PE in 50 yr soil ensembles. The medians for the Rix-Fernandez ensemble are higher for periods longer than 1.2 s. Table 7.2 presents the median S_a values at the fundamental period of the frames for the above ensembles,

103

Table 7.2 Median spectral accelerations and logarithmic standard deviations at the fundamental periods of the frames for the Wen-Wu and Rix-Fernandez 2% PE in 50 yr soil ensembles.

| | 2% PE in 50 yr soil ensembles | | | |
| | Wen-Wu | | Rix-Fernandez | |
T_1 (s)	$\hat{S}_a$ (g)	ζ	$\hat{S}_a$ (g)	ζ
1.12	0.56	0.46	0.51	0.33
1.88	0.30	0.30	0.48	0.28
2.82	0.25	0.40	0.29	0.27

along with the logarithmic standard deviations ζ defining the variability in the response spectrum at those periods.

The interstory drifts from the NTHAs of the three-, six-, and nine-story frames subjected to the scaled[d] Rix-Fernandez accelerogram #1 from the 2% PE in 50 yr ensemble are illustrated in Figure 7.4, and are on the order of 4 to 6%. Eigenvalue analyses that were performed at certain time steps of the ground motion record allow the change of the fundamental (or modal) periods of the frames to be monitored and provide more insight into the nature of their nonlinear structural responses. Figure 7.5 depicts the period lengthening of the first three modes of the frames. The points at which nonlinear actions initiated — approximately 10 s in the three-story and 21 s in the six- and nine-story frames — are evident in Figure 7.5. Subsequently, the fundamental periods of the three-, six-, and nine-story frames lengthened significantly to values in the following approximate ranges: 1–2 s, 2–3 s, and 3–4 s, respectively (note the much higher values when unloading). The behavior illustrated by Figures 7.4 and 7.5 is typical of what was

---

[d] None of the frames was able to withstand the original accelerogram in that the drift responses were for the last IDAs before failure to converge as described above. Figures 7.4a, b, and c were obtained by scaling downward to 0.52 g, 0.51 g, and 0.20 g, respectively.

observed when the frames were subjected to the Rix-Fernandez 2% PE in 50 yr ensembles.

The median S_a values at the fundamental period of the three-story frame are similar for both Wen-Wu and Rix-Fernandez (2% PE in 50 yr soil) ensembles (see Table 7.2; 0.56 g vs. 0.51 g). However, the number of collapse cases when the Rix-Fernandez ground motions were imposed on the frame, was higher (seven vs. two). This is due to the higher spectral intensity in the Rix-Fernandez ground motions at periods beyond 1.2 s (see Figure 7.3), particularly in the range of 1–2 s, where the lengthened fundamental period of the softened frame fell (see Figure 7.5a). Consequently, the median drift demands were significantly higher for the Rix-Fernandez ground motions than for the Wen-Wu ground motions (*cf.* Eq. 7.1a to Eq. 7.1b and Figures 7.1a to 7.1b).

Similar median drift demands were obtained for the six-story frame under both Wen-Wu and Rix-Fernandez ensembles — albeit slightly higher for the Rix-Fernandez ground motions beyond approximately $S_a(T_1)$ values of 0.4 g (*cf.* Eq. 7.1c to Eq. 7.1d and Figures 7.1c to 7.1d). The fundamental period of the softened six-story frame fell into the range of 2–3 s (see Figure 7.5b), a range over which the differences between the spectral amplitudes of the Wen-Wu and Rix-Fernandez ground motions are smaller than at other periods greater than 1.2 s (see Figure 7.3). Hence, the median drift demands were similar. However, the number of collapses when the frame was subjected to the Rix-Fernandez ground motions was again higher (six vs. one for the Wen-Wu ensemble). In this case, it is because the median $S_a(T_1)$ values are significantly higher for the Rix-Fernandez ground motions for the six-story frame (see Table 7.2; 0.48 g vs. 0.30 g), unlike for the three-story frame.
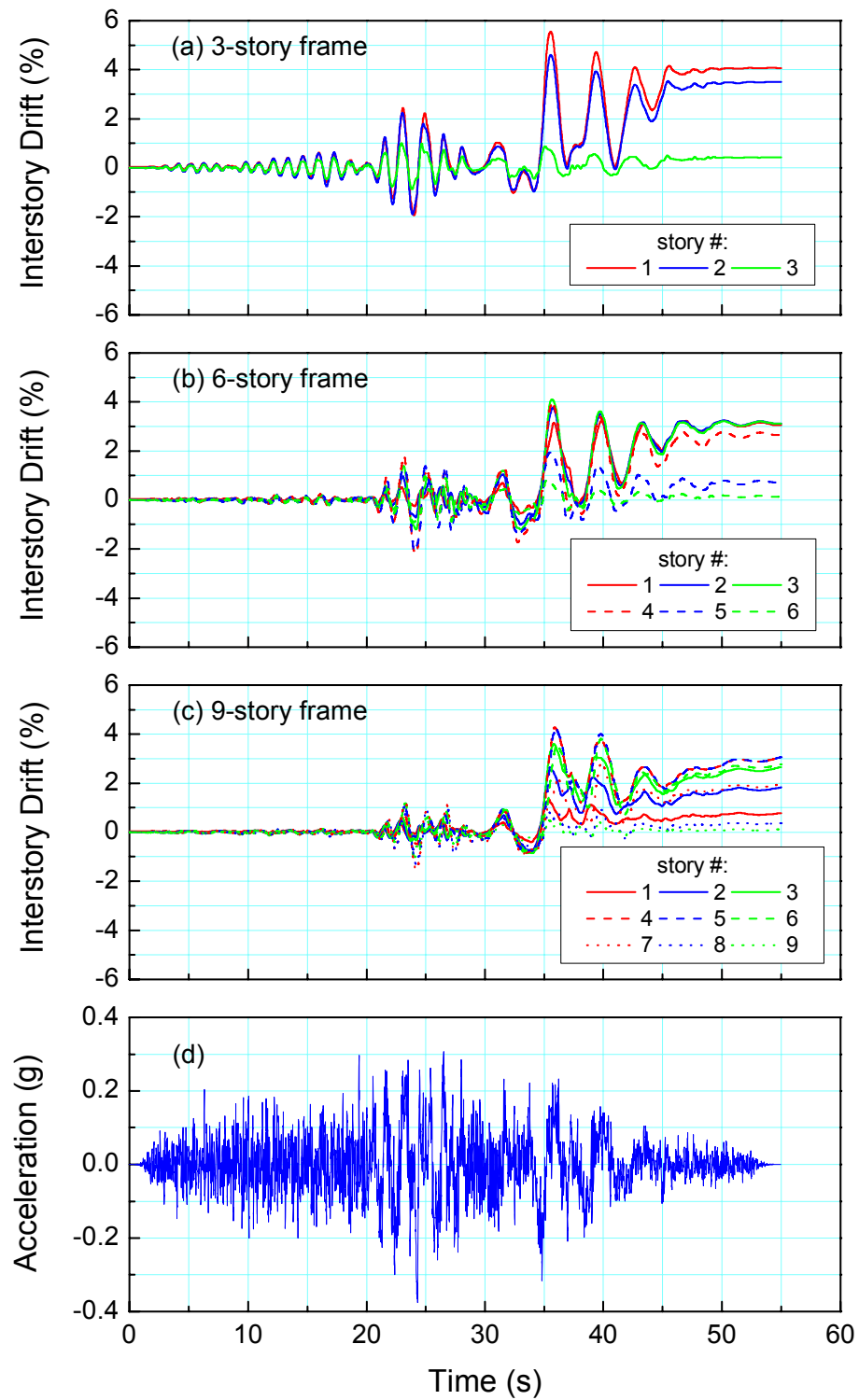
Figure 7.4 Interstory drifts from the NTHAs of the: (a) three-, (b) six-, and (c) nine-story frames subjected to the scaled (d) Rix-Fernandez accelerogram #1 from the 2% PE in 50 yr ensemble.
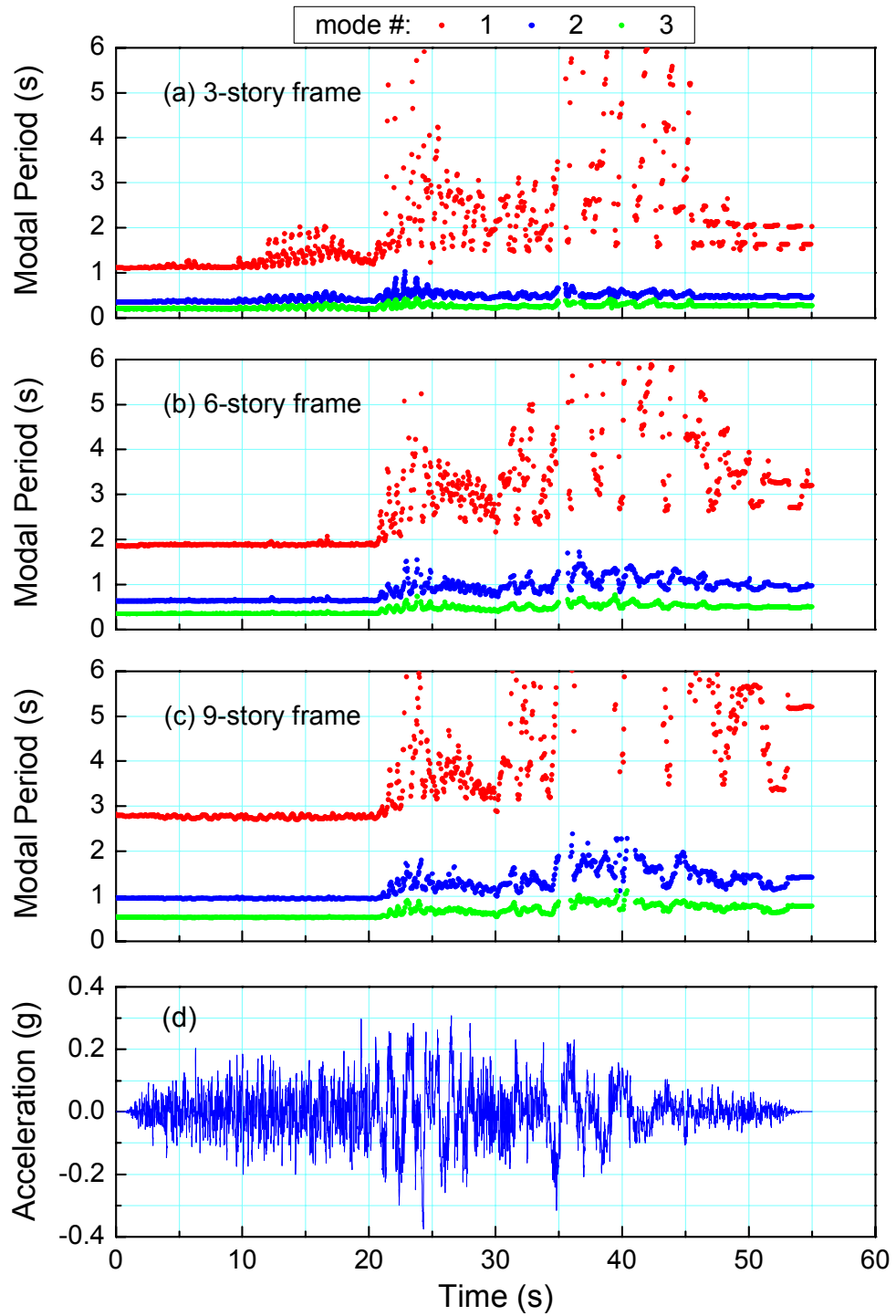
Figure 7.5 Instantaneous monitoring of the first three modal periods of the: (a) three-, (b) six-, and (c) nine-story frames under the scaled (d) Rix-Fernandez accelerogram #1 from the 2% PE in 50 yr ensemble.

Although the median $S_a(T_1)$ values for the nine-story frame are similar for both Wen-Wu and Rix-Fernandez ensembles (see Table 7.2; 0.25 g vs. 0.29 g), the Rix-Fernandez ground motions yielded higher median drift demands (*cf.* Eq. 7.1e to Eq. 7.1f and Figures 7.1e to 7.1f), as was the case for the three-story frame. Figure 7.5c shows that the fundamental period of the nine-story frame increased to well beyond 3 s due to softening, a range where the Rix-Fernandez ground motions have much higher spectral intensity than the Wen-Wu ground motions (see Figure 7.3). Accordingly, the number of collapse cases was again higher under the Rix-Fernandez ground motions (four vs. one).

The structural response analysis of the nine-story frame to the Rix-Fernandez accelerogram #1 from the 2% PE in 50 yr ensemble, which was depicted in Figure 7.4c, is chosen to demonstrate the impact of strong ground motion records with high spectral intensities at long periods on the structural frame responses. Figure 7.6a shows the Fourier amplitude spectrum of the strong motion record, which depicts the strength of the ground motion at different frequencies. High intensities at periods beyond 3 s are typical for the Rix-Fernandez ground motion ensembles that were generated for soil sites in Memphis, TN. The low-pass filtered ground motion record with a filter that allows the pass of frequencies lower than 0.36 Hz (or periods higher than 2.82 s — *i.e.,* the fundamental period of the nine-story frame) is compared with the original record in Figure 7.6b. The interstory drift of about 1% attained after the first 30 s of the ground motion record (see Figure 7.6c) softens the frame and increases the fundamental period of the frame to 3–4 s (see Figure 7.6d). Thereafter, the high spectral intensity component of the record with periods 3–5 s, which was not present prior to 30 s (see Figure 7.6b), significantly amplifies the drifts, as the fundamental period of the frame matches that of

the ground motion (*i.e.*, structural resonance), and results in interstory drifts in excess of 4% (see Figure 7.6c). The response characteristics summarized in Figure 7.6 are typical of the structural responses of the frames subjected to the Rix-Fernandez 2% PE in 50 yr ensembles (as can be deduced from Figure 7.4 for the other frames). These analyses emphasize the importance of the frequency content of the ground motions in the spectra that are used to synthesize acceleration records for seismic performance assessment in the CEUS.

(a) Fourier amplitude spectrum

(b) Rix-Fernandez accelerogram

(c) 9-story frame response

(d) Instantaneous modal periods
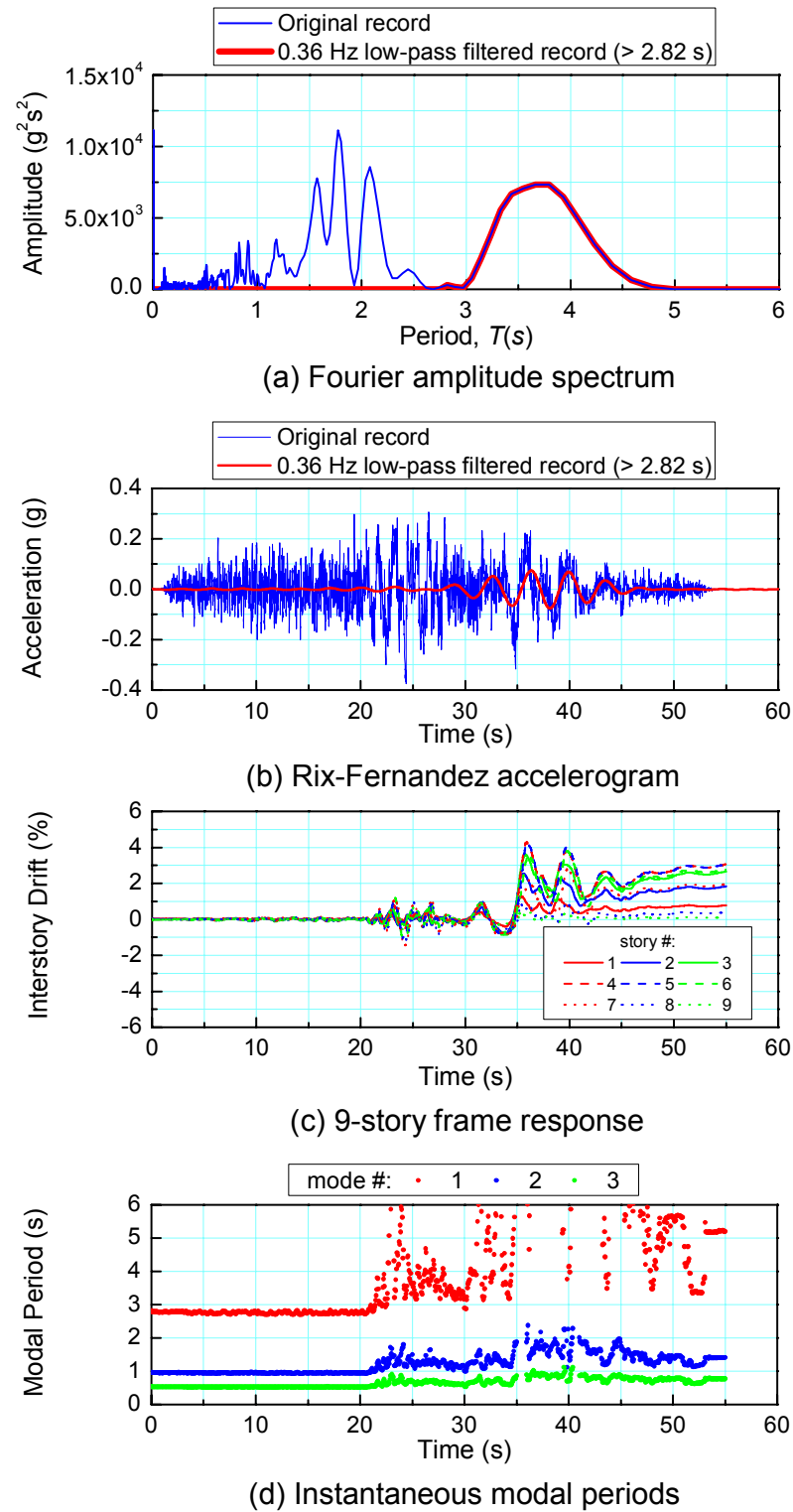
Figure 7.6 Response characteristics of the nine-story frame when subjected to the Rix-Fernandez accelerogram #1 from the 2% PE in 50 yr ensemble.

7.3 Seismic Fragilities for GLD RC Frames

The seismic fragilities for the three-, six-, and nine-story GLD RC frames were derived using the above probabilistic demand models in the seismic risk assessment framework presented in Chapter 5. These fragility estimates were provided for the Wen-Wu and Rix-Fernandez ground motions separately, where the differences display the impact of the choice of ground motion ensembles on seismic fragilities. The HAZUS fragilities for the same frames were also reproduced to provide additional perspective on fragility assessment of GLD RC frames in the CEUS.

7.3.1 Mean Fragilities

NSP analyses showed that the three-story frame remains elastic until 0.2% while the six- and nine-story frames remain elastic until 0.3% maximum interstory drifts, and that the ultimate base shear coefficients (V_u/W) are 10%, 5%, and 4%, respectively. Subsequent IDAs of the frames using the 2% PE in 50 yr soil ensembles produced a set of collapse drift limits θ_{max}^{CP} (defined previously as maximum interstory drifts prior to failure to converge) for each frame-ensemble pair. Statistical analyses of these IDA results using the rank-ordering method (with the assumption that the θ_{max}^{CP} are lognormally distributed — consistent with the fragility formulation) yielded the medians and logarithmic standard deviations of the maximum interstory drifts at incipient collapse. Figure 7.7 illustrates such an analysis of the collapse drift limit data obtained from the IDA of the three-story frame using the Wen-Wu ensemble, where $\Phi^{-1}[i/N+1]$ is the inverse standard normal CDF evaluated at the cumulative probability of the i th ranked collapse drift limit out of N such drift limits. The ordinate of the linear regression line when the inverse CDF is
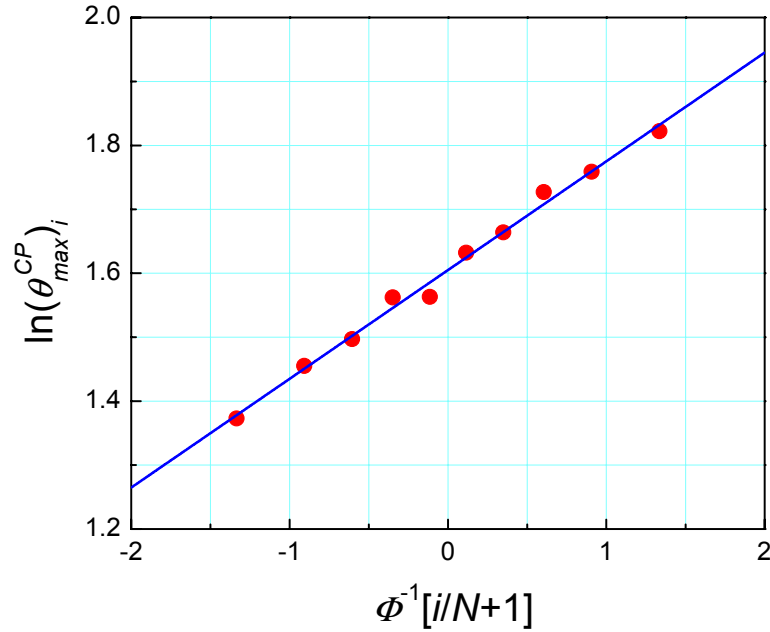
Figure 7.7 Rank-ordering method.

zero denotes the natural logarithm of the median of θ_{max}^{CP}, while the slope denotes its logarithmic standard deviation.

Table 7.3 summarizes all parameters used in the fragility formulation given by Eq. 5.12 for each frame for both the Wen-Wu and Rix-Fernandez ground motions. At the CP level, the differences in d and β_C are due to the use of different ensembles in the IDAs. The seismic fragility curves of the frames for the three performance levels identified in Chapter 5 — IO, SD, and CP — are illustrated in Figure 7.8. The fragilities that were obtained using the Rix-Fernandez ground motions are significantly higher for the three- and nine-story frames than those obtained using the Wen-Wu ground motions, while they are similar for the six-story frame. The differences between the fragilities due to the choice of ground motions will be examined further at various earthquake hazard levels for Memphis, TN subsequently.

Table 7.3 Summary of the parameters used in the fragility formulation.

		3-story		6-story		9-story	
		W-W[*]	R-F[*]	W-W	R-F	W-W	R-F
Demand							
a		4.8	15	8.1	11	8.1	21
b		1.02	1.61	0.99	1.20	0.93	1.21
$\beta_{D|S_a}$		0.30	0.44	0.32	0.34	0.26	0.31
Capacity							
	IO	0.2		0.3		0.3	
d	SD	2		2		2	
	CP	5.0	5.0	3.9	4.0	3.6	4.2
	IO	0.25		0.25		0.25	
β_C	SD	0.25		0.25		0.25	
	CP	0.17	0.20	0.08	0.15	0.13	0.15
Modeling							
β_M		0.20		0.20		0.20	

[*] W-W: Wen-Wu; R-F: Rix-Fernandez.
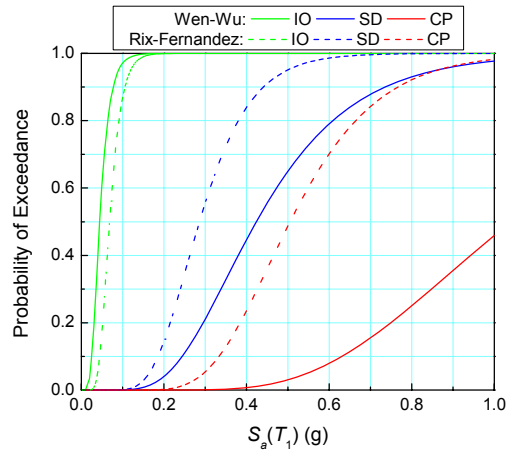
(a) 3-story
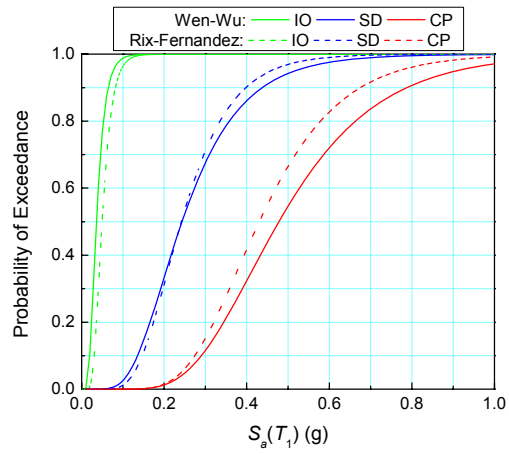
(b) 6-story
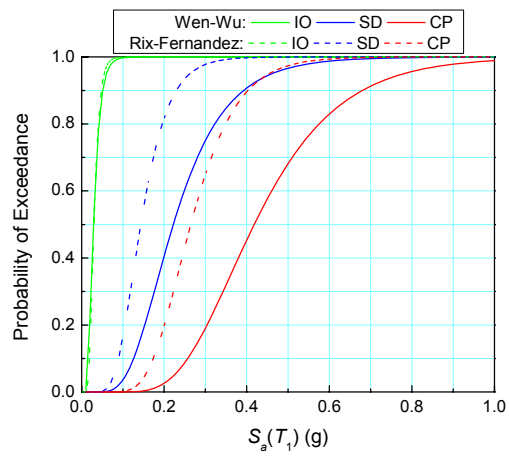
(c) 9-story

Figure 7.8 Seismic fragility curves for the three-, six-, and nine-story GLD RC frames.

114
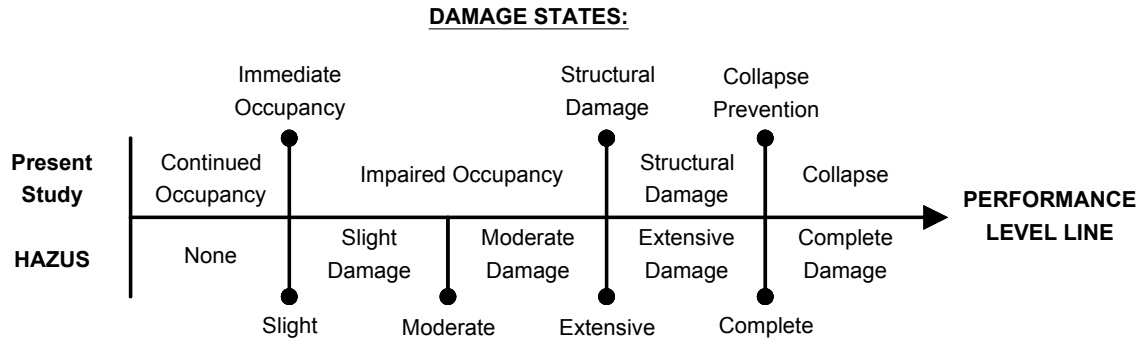
DAMAGE STATES:

Figure 7.9 Mapping between damage states in HAZUS and performance levels in this study.

7.3.2 HAZUS Fragilities

The fragilities in HAZUS are modeled by lognormal distributions, defined by the median building capacity and a logarithmic standard deviation, β, in which the aleatoric and epistemic uncertainties are combined (*cf.* Eq. 5.4). Beyond this similarity, they are based on different formulations than those used in this study, and these differences must be reconciled to make a consistent comparison between them. HAZUS uses the capacity spectrum method, which is based on a NSP analysis, to define the building response [Freeman, 1998]. The fragilities are functions of peak building response defined by spectral displacement, S_d, at a period T_c, which is determined by the point of intersection of the pushover curve and the demand spectrum [Porter *et al.*, 2002; Erberik and Elnashai, 2006]. This period is higher than the initial fundamental period when the frame responds inelastically. Furthermore, the damage limits in HAZUS (slight, moderate, extensive, and complete) do not correspond directly to the IO, SD, and CP performance levels. Figure 7.9 provides a mapping between the damage states in HAZUS and the performance levels in this study.
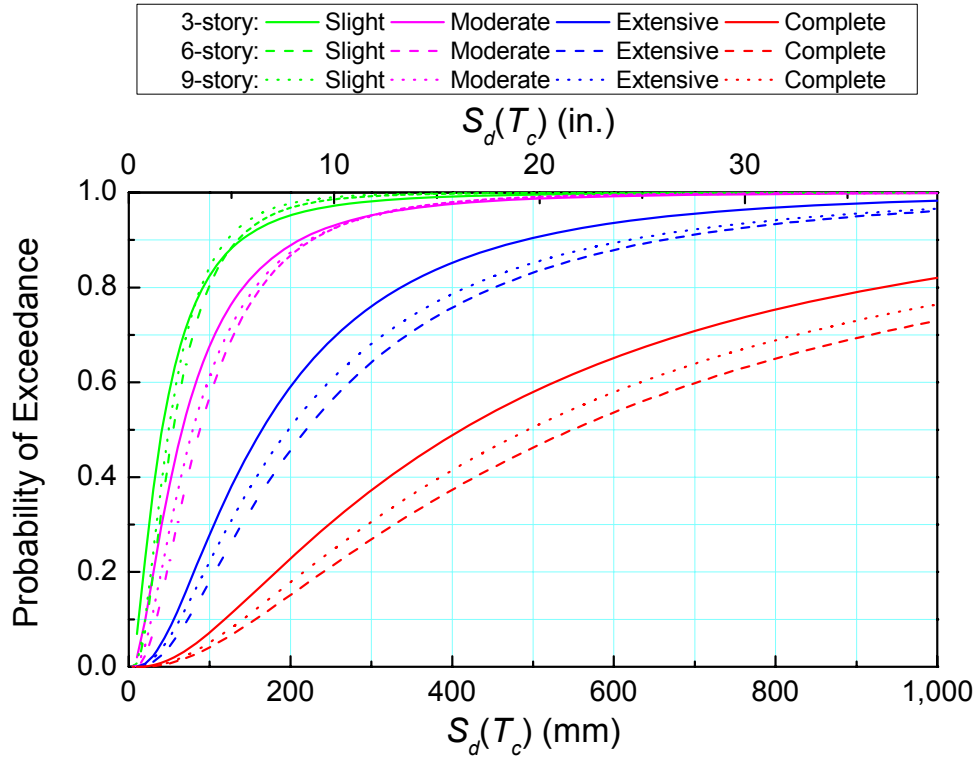
Figure 7.10 HAZUS fragility curves for the three-, six-, and nine-story GLD RC frames.

The HAZUS fragilities for the same three-, six-, and nine-story GLD RC frames were reproduced using the medians and logarithmic standard deviations in Table 5.9c of the HAZUS manual [FEMA, 2003a] (adjusted for building height)[e] for building types C1L, C1M, and C1H (denoting low-, mid-, and high-rise concrete moment frames). Although the fragilities for the pre-code seismic design level in HAZUS are intended for buildings that were not designed for earthquake effects, HAZUS does not consider the additional lateral strength that such buildings might have if they were designed for wind effects. Hence, the fragilities for the low code rather than the pre-code seismic design level were reproduced for the frames in this study. These fragility curves are illustrated in Figure 7.10 and delineate the four distinct HAZUS damage states.

---

[e] The medians are multiplied by the ratio of the actual height of the frame to the typical height assigned in HAZUS in accordance with the Eq. 5-4 in the HAZUS manual.

A simple relation between S_a in this study and S_d in HAZUS does not exist, as they are defined at different periods — T_1 vs. T_c — making it difficult to compare the fragilities from the two approaches directly in one figure. Although it is possible to convert S_a to S_d at the expense of computations that involve the application of the capacity spectrum method for each frame-accelerogram pair utilized for the derivation of fragilities in this study, this would preclude the convolution of these fragilities with seismic hazard curves which are customarily presented in terms of S_a. Rather than to compare the fragilities directly, then, the damage state probabilities from the two methods are compared at various earthquake hazard levels for Memphis, TN in the following section.

7.4 Seismic Vulnerability of GLD RC Frames

Buildings are expected to meet distinct performance levels when subjected to earthquake ground motions of various intensities, as illustrated in Figure 7.11 [SEAOC, 1995]. The seismic vulnerability of the RC frame inventory in Memphis, TN was appraised with regard to these performance-based design objectives, defined in terms of performance levels associated with reference earthquake hazard levels. Seismic fragilities derived above for the three-, six-, and nine-story GLD RC frames were utilized in determining the damage state probabilities at the specified earthquake hazard levels.

7.4.1   USGS Seismic Hazard

The UHRS were constructed for the earthquake hazard levels specified in the SEAOC Vision 2000 for Memphis, TN (35.117°N, 90.083°W) [FEMA, 2003a]. The USGS

Figure 7.11 SEAOC Vision 2000 performance objectives.

[2002c][f] provides the 5% damped S_a values on a firm rock site (FEMA 273 Site Class B). Local site conditions (Site Class D — based on shear wave velocity profiles for Memphis, TN [Wen and Wu, 2001; Fernandez and Rix, 2006]) were taken into account by amplifying the ground shaking demands by the soil factors in FEMA 273. Figure 7.12 illustrates the UHRS for Memphis, TN.[g]

7.4.2 Damage State Probabilities

Damage state probabilities were determined from the fragility curves that were derived separately using the Wen-Wu and Rix-Fernandez ground motions (see Figure 7.8). The

---

[f] The data for constructing the 50% PE in 50 yr UHRS were gathered from http://earthquake.usgs.gov/ research/hazmaps/design/index.php.
[g] The 5% PE in 50 yr UHRS are also presented here (as they will be referred to subsequently).
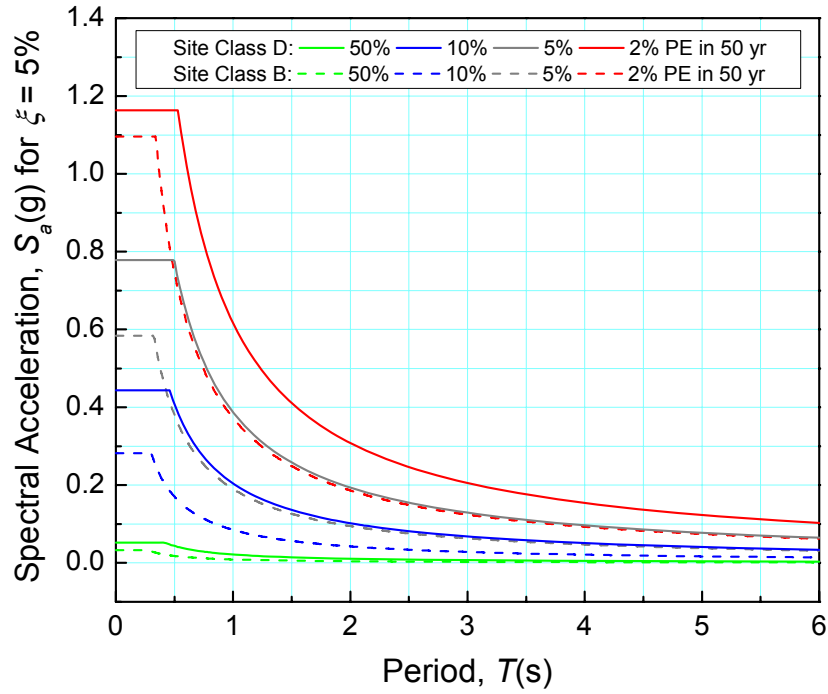
Figure 7.12 UHRS for Memphis, TN.

Table 7.4 $S_a(T_1)$ values from the 50%, 10%, 5%, and 2% PE in 50 yr UHRS for Memphis, TN (Site Class D).

PE in 50 yr	$S_a(T_1)$ (g)		
	3-story	6-story	9-story
50%	0.02	0.01	0.01
10%	0.18	0.11	0.07
5%	0.35	0.21	0.14
2%	0.55	0.33	0.22

$S_a(T_1)$ values from the 50%, 10%, and 2% PE in 50 yr UHRS[h], which are listed in Table 7.4 for each frame, were entered into the fragility curves. These damage state probabilities were subsequently compared to those from HAZUS in the same figure for each frame.

---

[h] Note that the seismic intensities are within the range that was covered by the seismic demand analyses and for which the seismic fragilities were derived.

HAZUS building responses were determined from the intersection of the inelastic demand spectra (constructed using the elastic response spectra in Figure 7.12) with the corresponding pushover curves, as described in FEMA [2003a]. Each of these intersection points was determined by adjusting the hysteretic damping (used for constructing the inelastic spectrum) until the area enclosed by the hysteresis loop in consequence of a building response given by the intersection point resulted in the same hysteretic damping. Figure 7.13 illustrates the final iteration steps of the procedure and Table 7.5 lists the $S_d(T_c)$ values determined for all frames. HAZUS damage state probabilities were then determined using the above $S_d(T_c)$ values in the HAZUS fragility curves reproduced in Figure 7.10; these probabilities were compared to those obtained in this study using the Wen-Wu and Rix-Fernandez ground motions separately. Figures 7.14 to 7.16 illustrate the comparisons for the three-, six-, and nine-story frames, respectively, where the slight and moderate damage states in HAZUS are mapped to the impaired occupancy damage state in this study (see Figure 7.9).
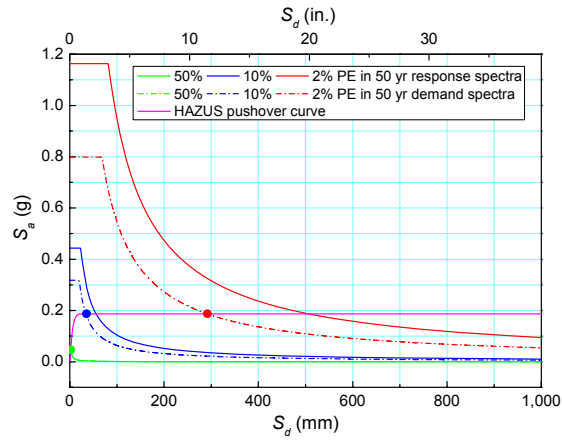
(a) 3-story
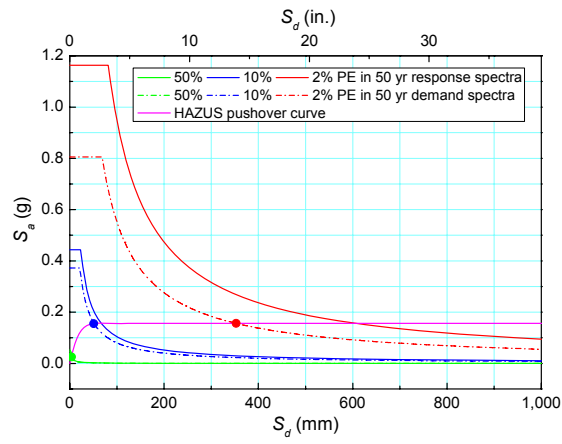
(b) 6-story
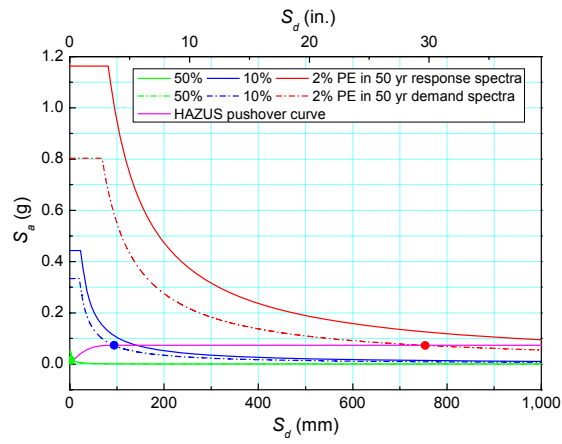
(c) 9-story

Figure 7.13 Capacity spectrum method in HAZUS.

Table 7.5 $S_d(T_c)$ values at the 50%, 10%, and 2% PE in 50 yr earthquake hazard levels for Memphis, TN (1 in. = 25.4 mm).

	$S_d(T_c)$ (mm)		
PE in 50 yr	3-story	6-story	9-story
50%	2	4	7
10%	36	51	94
2%	292	353	754
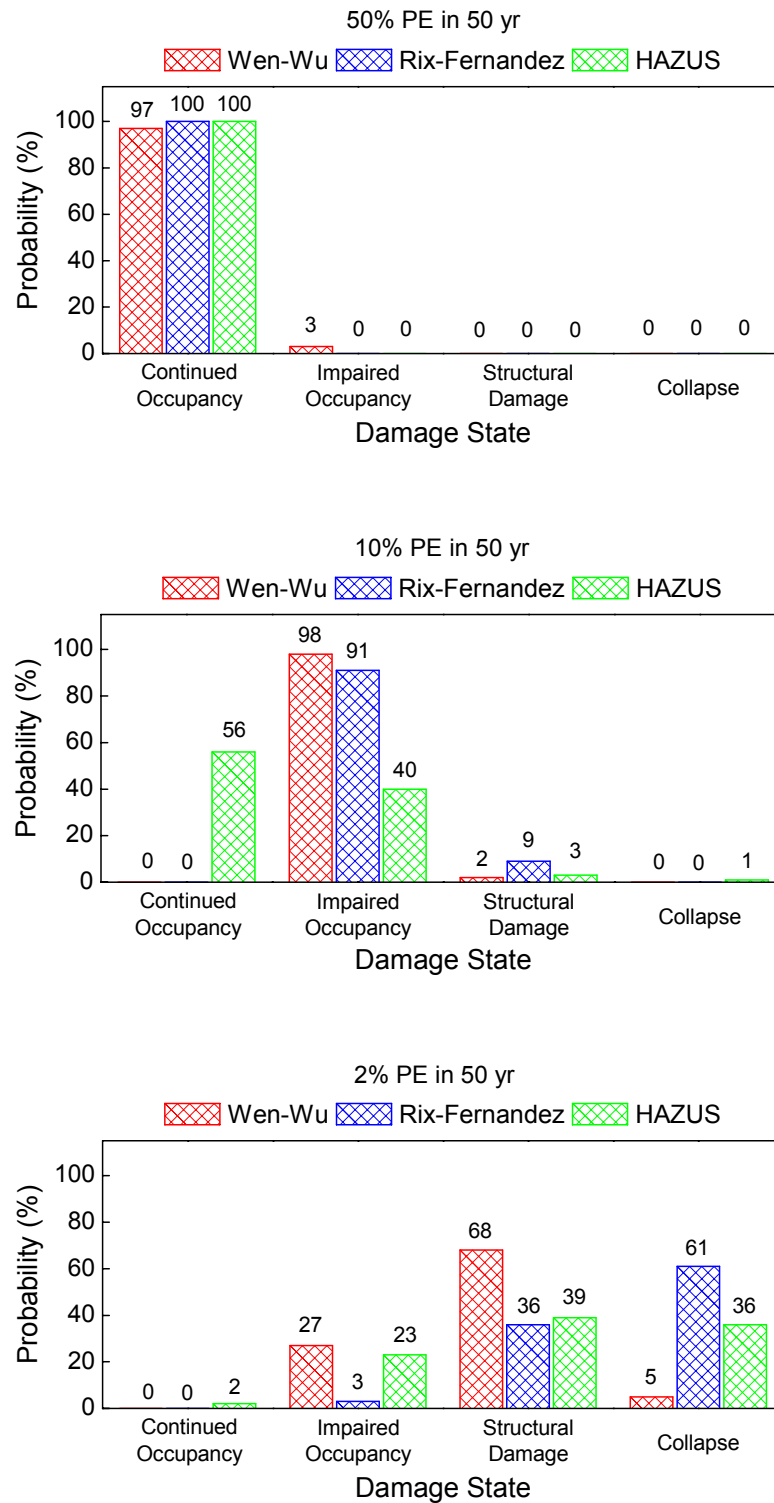
Figure 7.14 Damage state probabilities for the three-story frame at 50%, 10%, and 2% PE in 50 yr earthquake hazard levels for Memphis, TN.
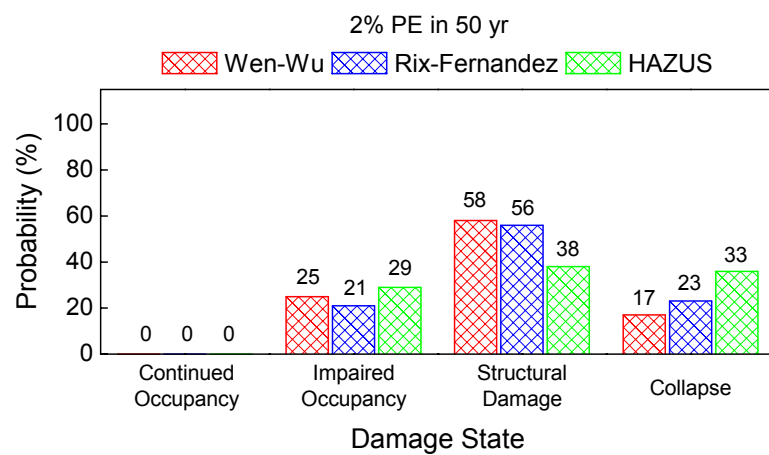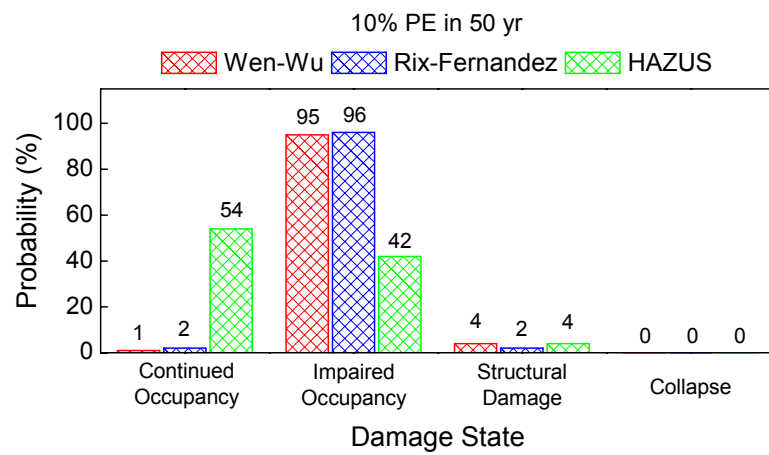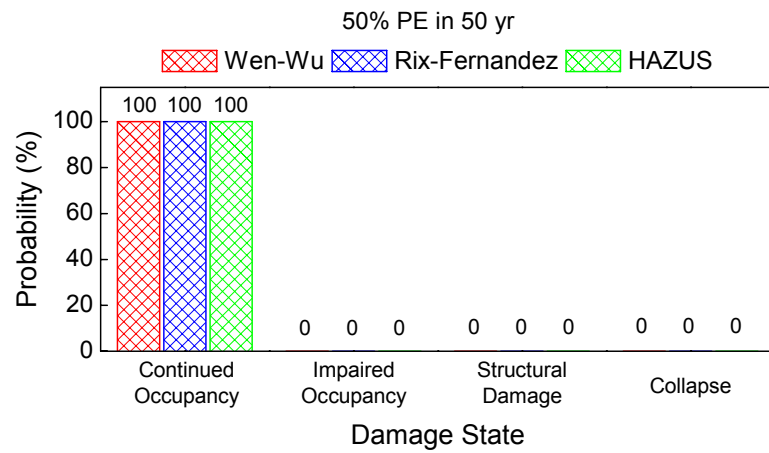
Figure 7.15 Damage state probabilities for the six-story frame at 50%, 10%, and 2% PE in 50 yr earthquake hazard levels for Memphis, TN.

124
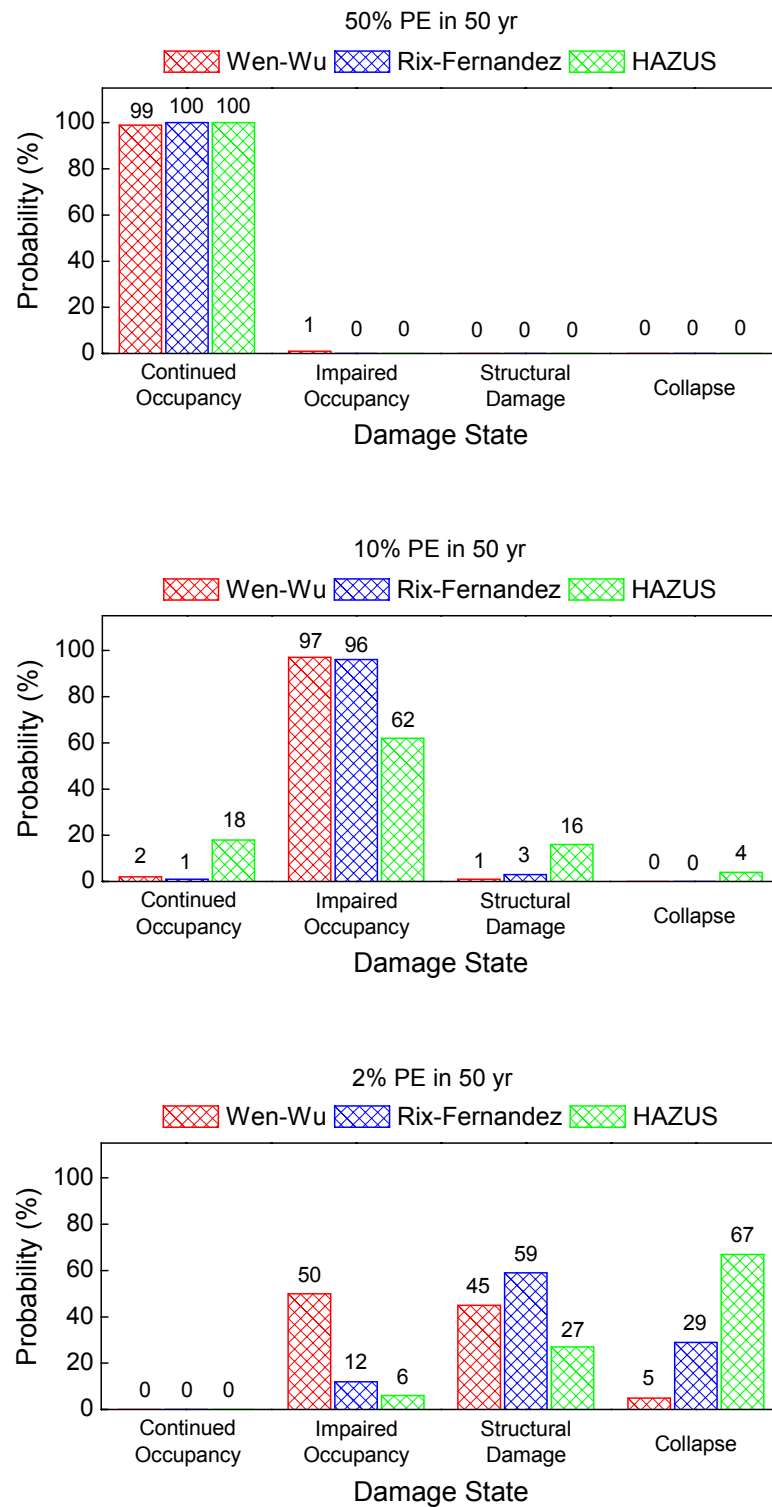
Figure 7.16 Damage state probabilities for the nine-story frame at 50%, 10%, and 2% PE in 50 yr earthquake hazard levels for Memphis, TN.

Damage state probabilities based on the Wen-Wu and Rix-Fernandez ground motions are both similar except for the 2% PE in 50 yr earthquake hazard level. For that particular hazard level, the fragilities that are based on the Rix-Fernandez ground motions predict significantly higher collapse probabilities for the three- and nine-story frames while those for the six-story frame are similar. When considered at the same hazard level, the HAZUS fragilities tend to be quite conservative in predicting collapse in comparison with those computed through a more sophisticated NTHA-based assessment, particularly for the nine-story frame. Note that the HAZUS fragility predicts a collapse probability that is in between those predicted by the NTHA-based fragilities for the three-story frame. In contrast, for the 10% PE in 50 yr hazard level, the HAZUS fragilities are not conservative and predict less damage for the three- and six-story frames; while HAZUS predicts higher damage state probabilities at the other end of the damage state spectrum (*i.e.*, structural damage and collapse damage states) for the nine-story frame. Finally, all three fragility analyses indicate that following an earthquake with an intensity level of 50% PE in 50 yr, all frames would remain safe to occupy without a need for significant structural repair.

The differences between the HAZUS-based and NTHA-based fragilities in this study are attributed to the fact that the deformation limits in the HAZUS fragilities are conservative (particularly for the six- and nine-story frames as shown in Table 7.6), and the logarithmic standard deviations are substantially higher, often exceeding 90%, while those in this study are on the order of 50% or less. It should be noted that HAZUS is aimed at regional loss estimation rather than individual building assessment, and the large logarithmic standard deviations reflect the considerable variation in construction that

126

Table 7.6 Comparison of performance limits in this study and in HAZUS in terms of θ_{max} (%).

Frame	Present Study			HAZUS		
	IO	SD	CP[*]	Slight	Extensive	Complete
3-story	0.2	2	5.0	0.5	2.0	5.0
6-story	0.3	2	4.0	0.33	1.33	3.33
9-story	0.3	2	3.8	0.25	1.0	2.5

[*] Average of those determined using the Wen-Wu and Rix-Fernandez ground motions.

exists within each building category. Thus, it is not surprising that a HAZUS analysis may lead to an erroneous appraisal of individual building performance, as it was not developed for that purpose.

7.4.3 Performance Appraisal of GLD RC Frames

Historically, ordinary buildings have been designed to achieve the *life safety* performance level when subjected to a design level earthquake ground motion, which was associated with a 10% PE in 50 yr [Leyendecker *et al.*, 2000]. At the life safety level, the building has experienced significant structural and non-structural damage with substantial reduction in its lateral stiffness and strength but still retains a significant margin against collapse. When the 10% PE in 50 yr level was selected over two decades ago as a basis for earthquake-resistant structural design, the factor of safety against collapse for a properly detailed structure was believed to be approximately 1.5.

In the development of *the 1997 NEHRP[i] recommended provisions for seismic regulations for new buildings and other structures* [FEMA 302/303, 1997b], the concept of a design basis earthquake ground motion with uniform PE throughout the U.S. was abandoned [Hamburger, 1997]. Instead, FEMA 302/303 and the current version FEMA

---

[i] National Earthquake Hazards Reduction Program.

450 [2003b] have aimed at providing a uniform margin against collapse throughout the U.S. It was judged that buildings should not collapse when subjected to a maximum considered earthquake (MCE) ground motion, which is associated with a 2% PE in 50 yr probability level, a level that was stated [Hamburger, 1997] as being consistent with the level of risk adopted by society with regard to other hazards. At the collapse prevention level, the building has sustained nearly complete damage and little margin remains against collapse. The seismic margin, defined quantitatively as the ratio of the ground motion intensity of an earthquake that could cause the collapse of the building to that of a design earthquake, was judged to be at least 1.5 for buildings designed in accordance with FEMA 302/303 due to the intentional conservatism in the provisions [Leyendecker *et al.*, 2000]. Hence, the design level earthquake ground motion, under which buildings are expected to provide life safety performance level, was associated with an intensity that corresponds to 2/3 of the MCE ground motion.

The consequence of the above changes in the seismic design provisions is that the intensity of the *design level* earthquake ground motion is no longer associated with a uniform probability of being exceeded throughout the U.S. The return period (or the PE) of the design ground motion varies depending on the regional seismicity. A design ground motion equal to 2/3 of the MCE ground motion corresponds approximately to the traditional 10% PE in 50 yr level at WUS sites (except those within 10 km (6 miles) of active faults); in contrast, that design ground motion corresponds to approximately 5% PE in 50 yr level at many CEUS sites (*cf.* Table 7.4). These differences are illustrated for San Francisco, CA (37.767°N, 122.433°W) and Memphis, TN in Figure 7.17. Note that the slopes of the seismic hazard curves are flatter in the CEUS than in the WUS. The
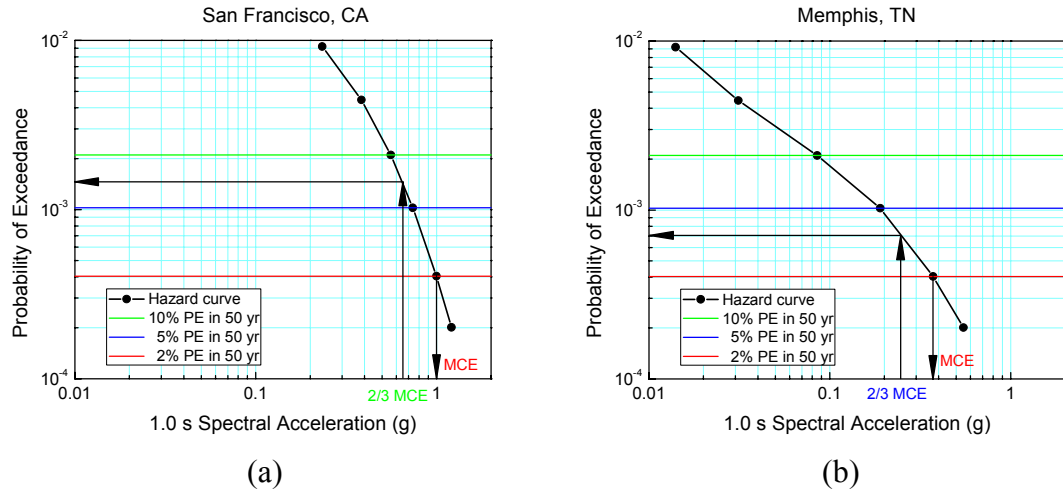
Figure 7.17 Seismic hazard curves for: (a) San-Francisco, CA and (b) Memphis, TN (Site Class B).

result is a uniform seismic margin (reliability) against collapse but not a uniform hazard (probability of exceeding the ground motion) [Leyendecker *et al.*, 2000].

According to Figure 7.11, ordinary buildings are expected to remain safe to occupy, with only slight structural damage, retaining their lateral stiffness and strength when subjected to frequent earthquakes associated with a 50% PE in 50 yr probability level. Significant non-structural repair may be required but the associated damage would not jeopardize life safety [FEMA 450, 2003b]. This performance objective was satisfied[j] for all GLD RC frames in this study; Figures 7.14 to 7.16 show that virtually all frames remain in the continued occupancy damage state under the 50% PE in 50 yr earthquake hazard.

At the traditional 10% PE in 50 yr earthquake hazard level that would have been deemed to be appropriate for ordinary buildings designed in the mid-1980s, all three

---

[j] The performance objective is assumed to be satisfied if the probability of being in damage states beyond the associated performance level is less than 10%. The regions of unsatisfactory performance are marked in figures that depict the damage state probabilities at distinct earthquake hazard levels.

frames met the life safety (SD in this study) performance level and the associated performance objective was satisfied. However, with the new provisions (FEMA 302/303 or FEMA 450), this performance objective has been tied to a design earthquake of 2/3 MCE, which is associated with approximately a 5% PE in 50 yr earthquake hazard in the CEUS, as explained above. The damage state probabilities at this 5% PE in 50 yr earthquake hazard level, which are illustrated in Figure 7.18 for all frames, reveal that the probabilities of structural damage and collapse damage states are high, and hence the risk to life safety during an earthquake with such intensity is significant. Therefore, this intermediate performance objective was not achieved for *any* of the three frames considered.

At the 2% PE in 50 yr earthquake hazard level, the collapse probabilities obtained for all frames were high, particularly when the Rix-Fernandez ground motions were utilized in the performance assessment (see Figures 7.14 to 7.16). Frames such as those considered in this study lack the seismic margin that would preclude their collapse under the 2% PE in 50 yr earthquake, notwithstanding their satisfactory performance under the 10% PE in 50 yr earthquake. The performance objective tied to the 2% PE in 50 yr earthquake hazard was not satisfied for any of the frames.

7.5 Summary

GLD RC frames are vulnerable to damage from joint shear failures (and deformations), beam bottom bar anchorage failures, significant P-Δ effects (due to the high flexibility of the frames), and weak column-strong beam effects leading to soft-story collapses under earthquake excitation.
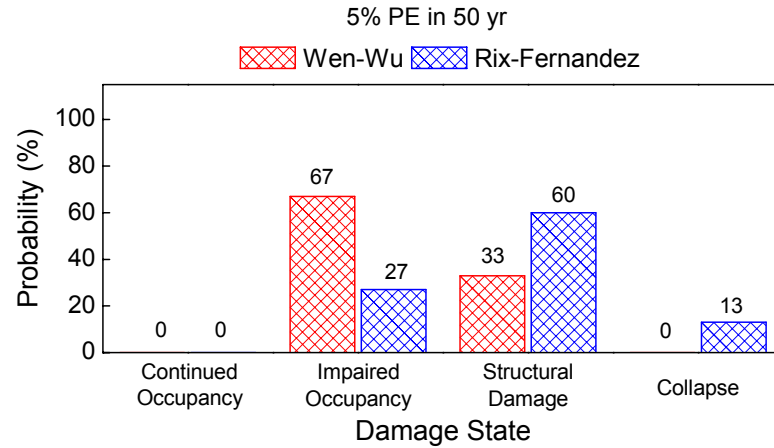
(a) 3-story
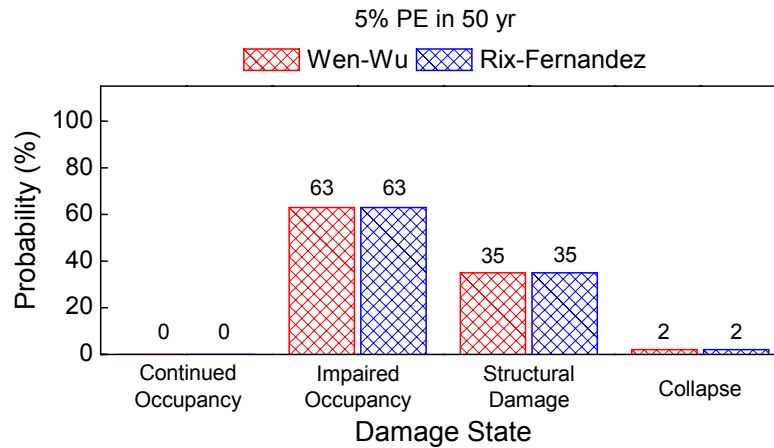
(b) 6-story
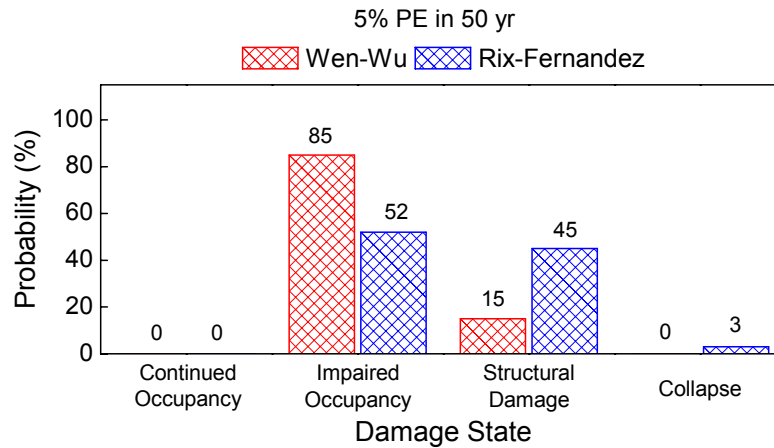
(c) 9-story

Figure 7.18 Damage state probabilities for the three-, six-, and nine-story frames at 5% PE in 50 yr earthquake hazard levels for Memphis, TN.

Seismic demands on such frames using different synthetic ground motion ensembles were strongly dependent on the frequency content of the ground motions. Significantly higher nonlinear structural responses at similar ground motion intensity levels were obtained from ground motions with high spectral intensities at longer periods, where the fundamental periods of flexible GLD RC frames fall.

Seismic fragilities were derived for low-, mid-, and high-rise GLD RC frames and were compared to the fragilities that are embedded in HAZUS. The HAZUS fragilities were found to be quite conservative for the 2% PE in 50 yr earthquake hazard level; in contrast, the opposite was true for the 10% PE in 50 yr earthquake.

Finally, the seismic vulnerability of the RC frame inventory in Memphis, TN was evaluated based on the performance-based design objectives in FEMA 450. GLD RC frames such as those considered in this study, which are typical of design practices in the CEUS, do not meet the life safety and collapse prevention performance objectives that are found in recent building codes and guidelines for performance-based earthquake engineering.

CHAPTER 8

SENSITIVITY OF FRAGILITY ESTIMATES TO ALEATORIC AND
EPISTEMIC UNCERTAINTIES

8.1 Introduction

The CBRM paradigm of the MAE Center requires the quantitative treatment and propagation of all sources of uncertainty within a probabilistic framework in order to obtain reliable seismic risk assessments. It is well-known that the earthquake ground motion is the major source of uncertainty in seismic demand and response [*e.g.*, Kwon and Elnashai, 2006]. In Chapter 7, the structural parameters were set equal to their median values in the finite element models and the structural fragilities reflect solely the uncertainty in earthquake ground motion. Most previous studies have neglected the contributions of the uncertainties in structural strength and stiffness entirely. To determine whether these uncertainties might also be important in certain circumstances, the contribution of uncertainties in material and structural properties and in beam-column joint model parameters to the overall seismic response and performance of the GLD RC frames are considered in this chapter.

In this chapter, structural parameters are modeled probabilistically in the finite element structural analyses of the GLD RC frames, and the sensitivity of frame response statistics to the uncertainties in beam-column joint model parameters, as well as material and structural properties, is investigated at various levels of earthquake hazard for Memphis, TN. Seismic fragilities that incorporate all sources of uncertainty are then derived and compared with those in Chapter 7. Finally, confidence bounds on the

133

fragilities are developed to provide a sense of their uncertainty and credibility for decision- and policy-makers in prioritizing risk mitigation efforts and developing post-earthquake response and recovery strategies [Wen and Ellingwood, 2005].

8.2 Uncertain Parameters

The following parameters were treated as random variables:

(1) Material properties: concrete compressive strength, f_c, and steel yield strength, f_y;

(2) Structural property: viscous damping, ξ; and

(3) Beam-column joint model parameters: bond-slip factor, α, (normalized) joint shear strength, $\left(\bar{\tau}_{jh}\right)_{max}$, and joint shear strains, $\left(\gamma_j\right)_{cr}$, $\left(\gamma_j\right)_y$, $\left(\gamma_j\right)_{max}$, $\left(\gamma_j\right)_{res}$ (see Section 6.5.1).

Concrete compressive strength and steel yield strength were assumed to follow normal and lognormal probability distributions, respectively [Healey *et al.*, 1980; MacGregor *et al.*, 1983]. The mean values (μ) were already defined in Chapter 4 as 1.25 times the nominal values. The COV of the concrete compressive strength was assumed to be 0.18 (reflective of *in situ* conditions, which include effects of placement and field curing) and that of the steel yield strength was assumed to be 0.11 [Healey *et al.*, 1980].

Structural damping is another important parameter that affects the dynamic responses of the frames. In nonlinear analyses, hysteretic damping is simulated through hysteresis models of materials. Viscous damping, therefore, should only reflect the damping present when the frame responds elastically. Healey *et al.* [1980] reported such damping data gathered from a review of small-amplitude vibrations of RC buildings and

Table 8.1 Uncertain parameters (1 MPa = 145 psi, $10\sqrt{\text{psi}} = 0.83\sqrt{\text{MPa}}$).

Parameter		Probability Distribution[*]	10th	50th	90th
			Percentile Value		
Material properties [Healey *et al.*, 1980]					
f_c (MPa)		LN(μ = 34.5, COV = 18%)	26.5	34.5	42.5
f_y (MPa)		LN(μ = 345, COV = 11%)	298	343	395
Structural property [Healey *et al.*, 1980]					
ξ (%)		LN(μ = 4.3, COV = 76%)	1.4	3.4	8.1
Beam-column joint model parameters [Celik and Ellingwood, 2007]					
α		U(0.4,0.7)	0.43	0.55	0.67
$\left(\bar{\tau}_{jh}\right)_{max}$	Exterior joints (+)	U(5.0,7.5)	5.25	6.25	7.25
$\left(\sqrt{\text{psi}}\right)$	Exterior joints (+)	U(10.0,12.0)	10.2	11.0	11.8
	Interior joints	U(9.0,12.0)	9.3	10.5	11.7
$\left(\gamma_j\right)_{cr}$ (10^{-3} rad)		U(0.1,1.3)	0.22	0.7	1.18
$\left(\gamma_j\right)_{y}$ (10^{-3} rad)		U(2,10)	2.8	6	9.2
$\left(\gamma_j\right)_{max}$ (10^{-3} rad)		U(10,30)	12	20	28
$\left(\gamma_j\right)_{res}$ (10^{-3} rad)		U(30,100)	37	65	93

[*] N = Normal, LN = lognormal, U = uniform; distributions.

showed that the data were fit reasonably well by a lognormal distribution with a mean value of 4.3% and a COV of 0.76.

Beam-column joint model parameters, on the other hand, described by the experimental database summarized in Table 6.2, were modeled by uniform probability distributions. The experimental database was insufficient to extract any statistical information other than lower and upper limits for the parameters, and the uniform distribution is the distribution of maximum uncertainty under those conditions. The probability distributions for each of the above parameters, together with its 10th percentile, median, and 90th percentile values, are summarized in Table 8.1. Note that the (normalized) shear strengths of interior and exterior beam-column joints were represented by different uniform distributions but all three were assumed to be linearly correlated.

Note also that this sampling procedure leads, as well, to correlated beam and column strengths and stiffnesses.

8.3 Sensitivity of Response Statistics to Parameter Uncertainties

Frame response statistics were monitored at three levels of earthquake hazard for Memphis, TN: 10%, 5%, and 2% PE in 50 yr. The values of $S_a(T_1)$[a] for these mean hazard events were previously given in Table 7.4 for all three frames, as obtained from data provided by the USGS. The procedure followed in investigating the sensitivity of response statistics to uncertain parameters is summarized below.

First, all parameters of the finite element model were set equal to their respective median values, and frame responses (in terms of θ_{max}) were determined using the Wen-Wu soil ground motions scaled to one of the mean hazard levels identified above (stripe analysis — *cf.* Figure 2.1). A lognormal probability distribution was fit to these responses and the median ($\hat{\theta}_{max}$) and logarithmic standard deviation (ζ) were determined using the maximum likelihood method. This first analysis located the mid-range of $\hat{\theta}_{max}$ and ζ for the sensitivity analysis that followed (*cf.* Figures 7.1a, c, and e). Next, this procedure was repeated one-parameter-at-a-time, setting each parameter to its 10th or 90th percentile while holding the remaining parameters at their median values. The variation in median response (*i.e.*, $\hat{\theta}_{max}$) and in logarithmic standard deviation (*i.e.*, ζ) of the response then can be displayed through a *tornado diagram*; the absolute difference between the two extremes is called the *swing* [Porter *et al.*, 2002].

---

[a] T_1 is the fundamental period of the median-valued frame model in here.

136

The NTHAs failed to converge for some of the accelerograms when they were

scaled to higher mean hazard events. For such cases, the likelihood function was defined

as,

$$L(\Theta) = P[X_1 = x_1|\Theta] \cdots P[X_k = x_k|\Theta] \cdot P[X_{k+1} > x_{k+1}|\Theta] \cdots P[X_n > x_n|\Theta] \quad (8.1a)$$

or

$$L(\Theta) = \prod_{i=1}^{k} f_X(x_i|\Theta) \cdot \prod_{i=k+1}^{n} [1 - F_X(x_i|\Theta)] \quad (8.1b)$$

and was maximized through numerical analysis to find the descriptive parameters Θ of

the lognormal probability distribution (the median and ζ). In Equations 8.1, $f_X(x)$ is the

probability density function (PDF), $F_X(x)$ is the CDF, k is the number of converged

solutions, and n (= 20) is the total number of NTHAs for each stripe analysis. The x_i

values for $i > k$, each of which depicts the θ_{max} at incipient collapse, $(\theta_{max}^{CP})_i$, were set

equal to the median θ_{max}^{CP} determined from the IDAs of the median-valued frame model in

Chapter 7 (see Table 7.3).[b] An alternative to the maximum likelihood method for

estimating the lognormal parameters would be the rank-ordering method (*cf.* Figure 7.6)

but the rank-ordering method would require more than half of the NTHAs to converge to

estimate the median and the logarithmic standard deviation with a reasonable sampling

error.

Tornado diagrams for the three-, six-, and nine-story GLD RC frames are

illustrated respectively in Figures 8.1 to 8.3 for the three earthquake hazard levels. These

figures show that damping, concrete strength, and joint cracking strain have the greatest

---

[b] The median θ_{max}^{CP} of the median-valued frame model was used to avoid the computational burden of IDAs
in computing $(\theta_{max}^{CP})_i$ of the frame model with one parameter set at one of the extremes.

impact on the response statistics (or uncertainty). In contrast, joint shear strains at peak and residual strengths have virtually no impact on response uncertainty.

8.4 Treatment of Uncertainty in Fragility Estimates

Seismic fragilities that incorporate all sources of uncertainty considered above can be derived efficiently using Latin hypercube sampling (LHS) [McKay *et al.*, 1979] coupled to the finite element structural models. LHS provides a stratified sampling scheme rather than the purely random sampling in naïve Monte Carlo analysis [Ayyub and Lai, 1989]. Sampling is performed without replacement, ensuring that the entire probability space is covered. The sampling plan is given by

$$\mathbf{S} = \frac{1}{N}(\mathbf{P} - \mathbf{R}) \tag{8.2}$$

where $\mathbf{P}$ is an $N \times K$ matrix, in which each of the K columns is a random permutation of 1, 2, …, N; $\mathbf{R}$ is an $N \times K$ matrix of independent random numbers from the uniform distribution U(0,1); and N (= 40) and K (= 9) are the numbers of hypercubes and uncertain parameters, respectively [Olsson *et al.*, 2003]. Each element of $\mathbf{S}$, s_{ij}, is then mapped according to

$$x_{ij} = F_{X_j}^{-1}(s_{ij}) \tag{8.3}$$

where $F_{X_j}^{-1}$ is the inverse CDF for parameter j. Each row of $\mathbf{x}$ contains different sets of sampled parameters, from which statistical samples of frames were obtained. Figure 8.4 illustrates this sampling plan. Note that each column of $\mathbf{x}$ contains a single value of parameter j from each of the equally probable N intervals, and that more samples are not required as the number of parameters increases in LHS.
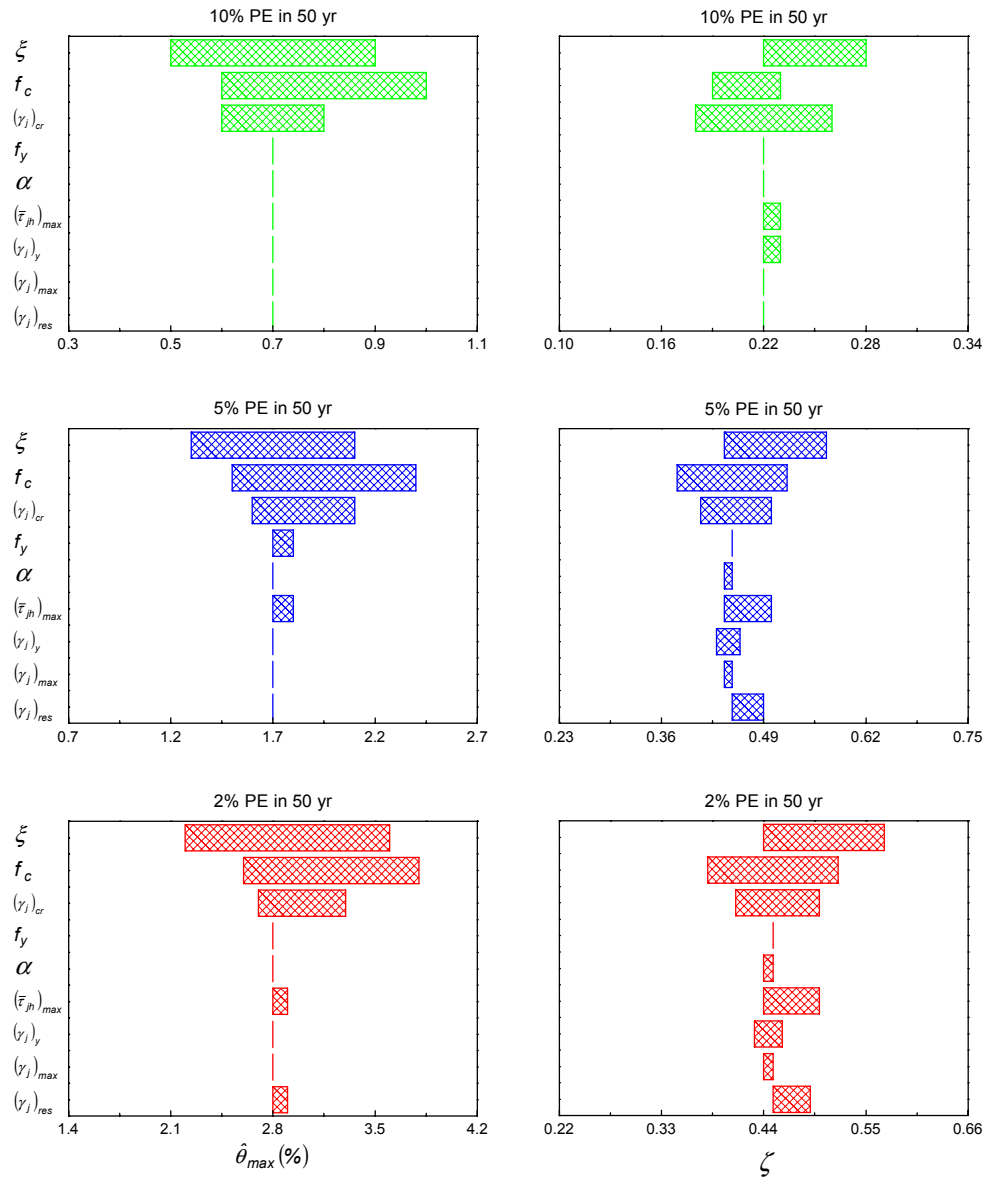
Figure 8.1 Tornado diagrams for the three-story frame.
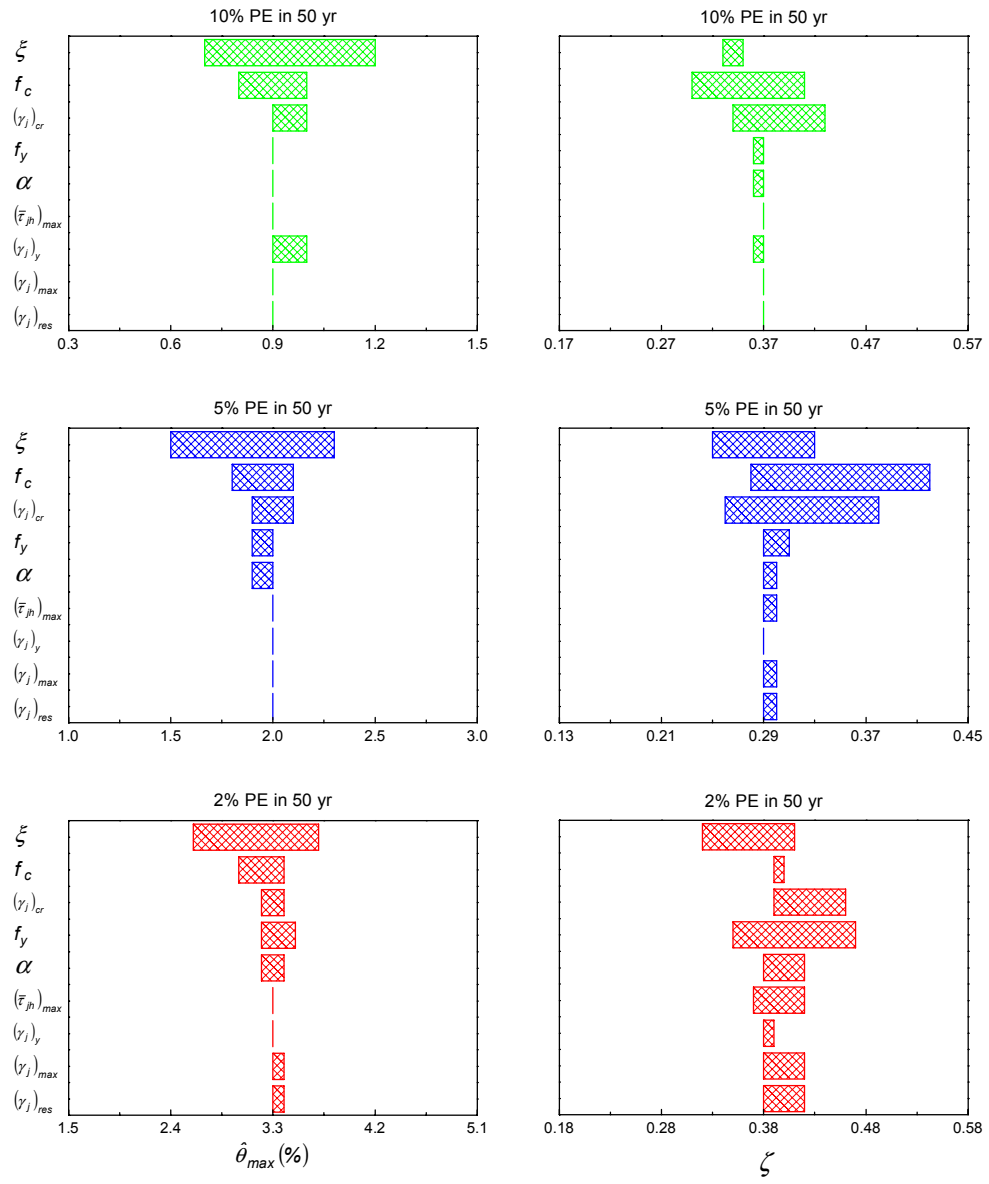
Figure 8.2 Tornado diagrams for the six-story frame.
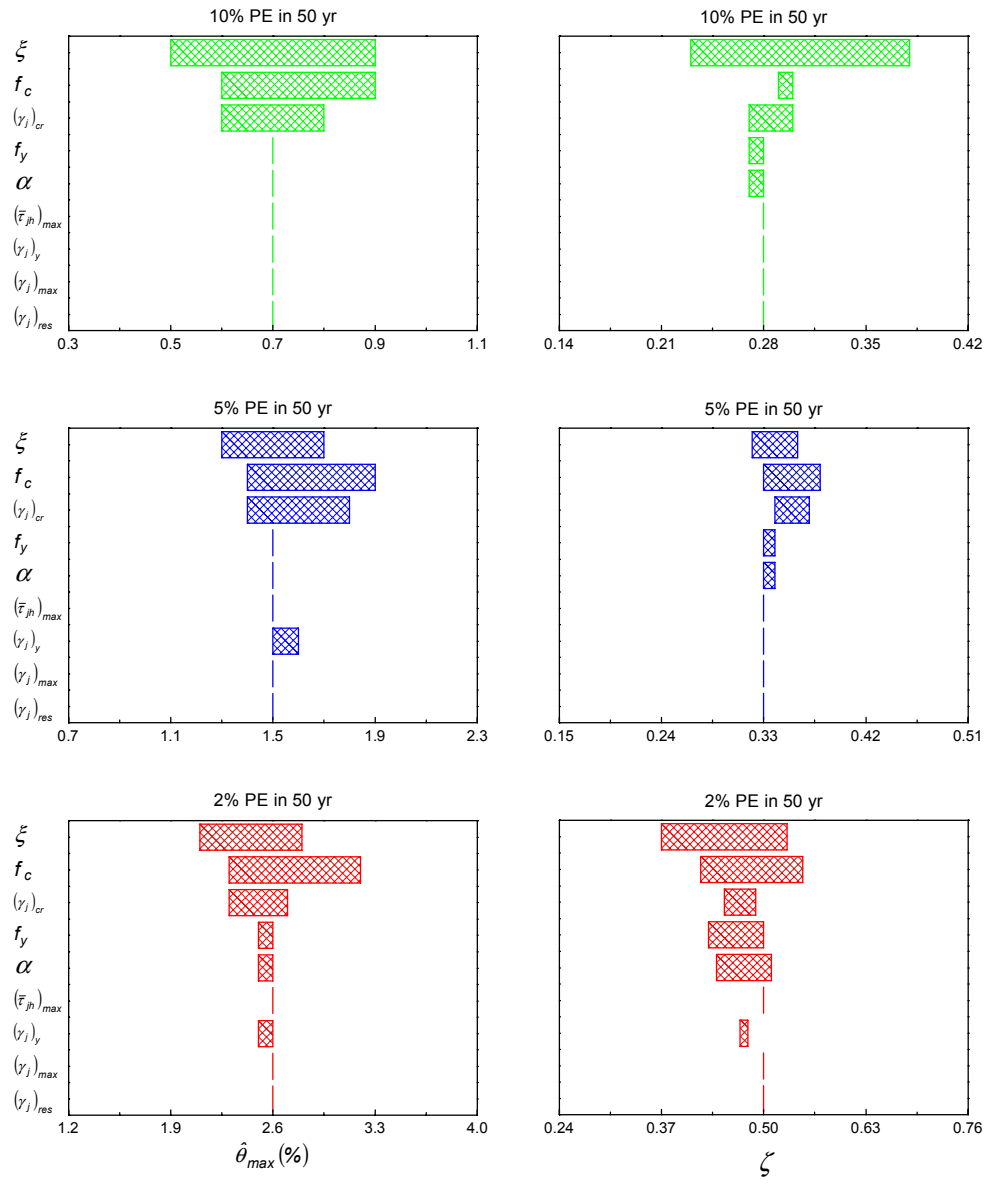
Figure 8.3 Tornado diagrams for the nine-story frame.
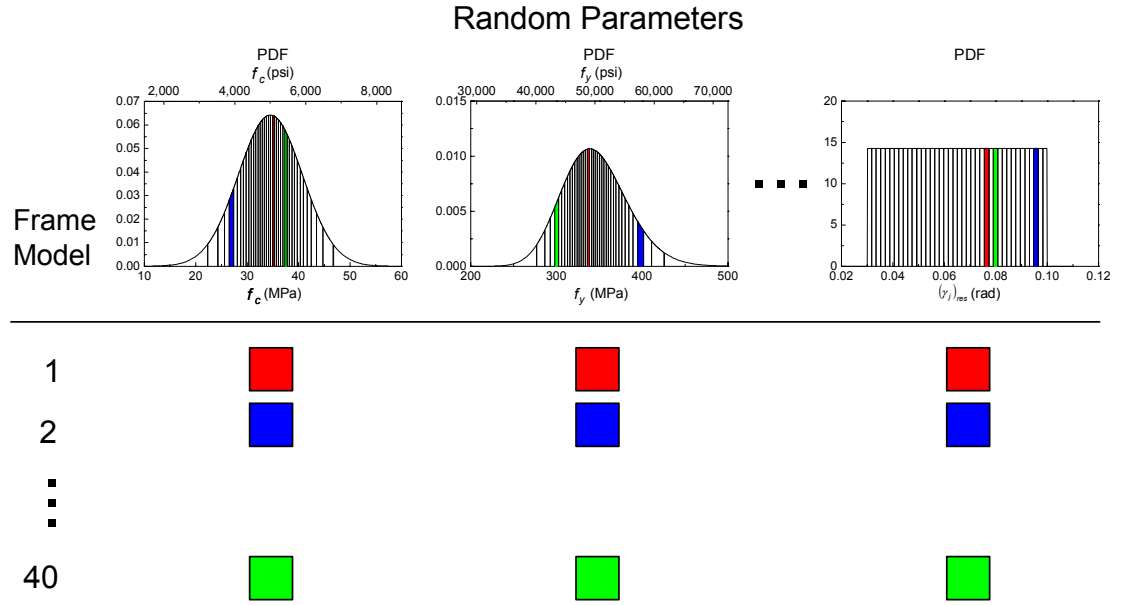
Figure 8.4 Sampling plan.

Sample frames were randomly matched with the 40 accelerograms from the Wen-Wu ensembles, and probabilistic seismic demand models were developed for the three-, six-, and nine-story GLD RC frames (cloud analysis — *cf.* Section 7.2.1). These demand models incorporated the uncertainties in structural parameters identified above in addition to the uncertainties in ground motion considered in Chapter 7. Seismic fragilities were derived using these demand models along with the limit state (capacity) parameters depicted in Table 7.3 for the median-valued frame models.

Each random matching of the sample frame models with the 40 Wen-Wu accelerograms constitutes a sample set for use in developing a probabilistic demand model and deriving a set of fragilities, as described above. The epistemic uncertainty associated with this sampling process must also be quantified in order to represent the overall uncertainty in the structural parameters. Hence, a database that allowed the

repetition of the process was generated. Figure 8.5 depicts this seismic demand database that comprises the responses of all sample frame models to all Wen-Wu accelerograms for each of the three GLD RC frames. Re-sampling 1,000 times by bootstrapping [Efron, 1979], the median (of the mean) fragility estimates were determined for each of the three GLD RC frames.[c] The comparisons of the medians of the fragilities with the fragilities of the median-valued frame models in Chapter 7, given in Figure 8.6, indicates fragilities for the three-story frame that are slightly higher and fragilities for the six- and nine-story frames that are slightly lower when the uncertainties in structural system parameters are incorporated along with the uncertainty in ground motion. In all cases, however, the contribution of the structural parameter uncertainties is relatively small in comparison with the uncertainty from the ground motion.

---

[c] The median was evaluated at each S_a increment of 0.01 g.
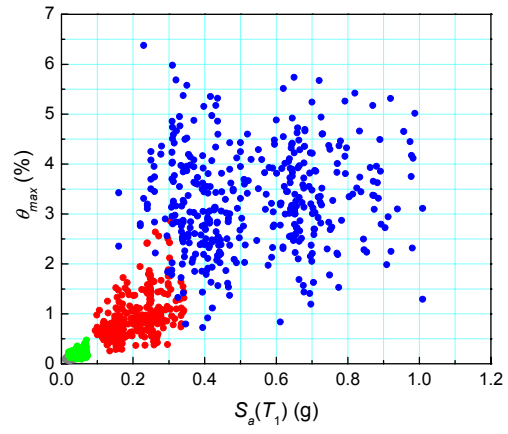
(a) 3-story
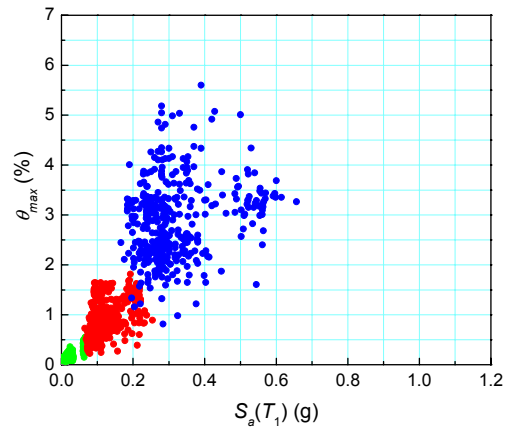
(b) 6-story
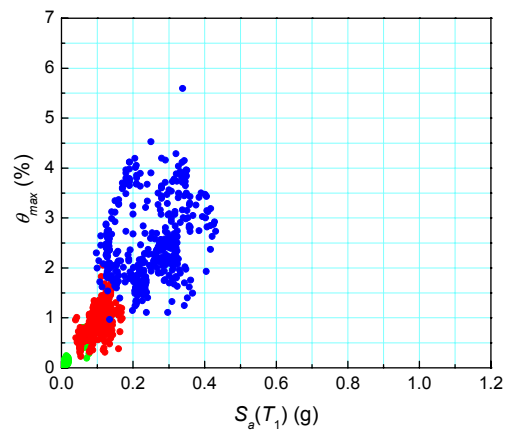
(c) 9-story

Figure 8.5 Seismic demand database (color code defined in Figure 3.6a).
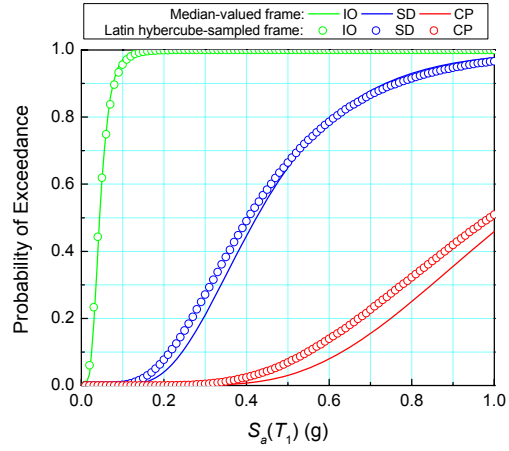
(a) 3-story
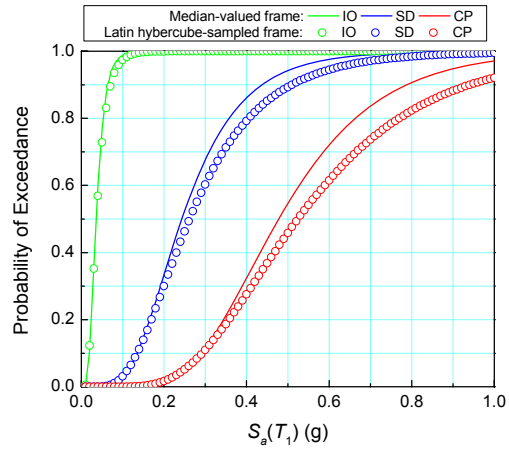
(b) 6-story
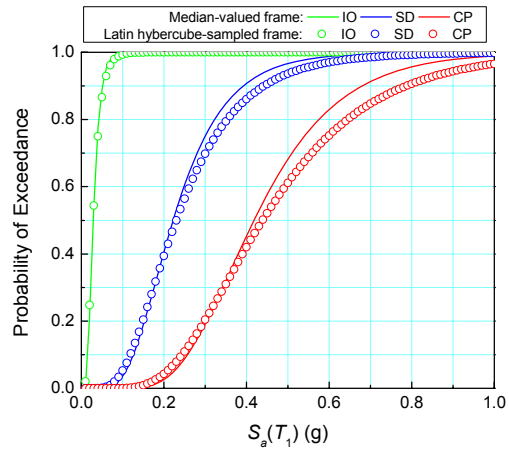
(c) 9-story

Figure 8.6 Comparisons of the medians of the Latin hypercube-sampled frame fragilities with the fragilities of the median-valued frame models in Chapter 7.

8.5 Confidence Bounds on the Fragility Estimates

Re-sampling by bootstrapping allows the quantification and display of epistemic uncertainty due to the sampling process through confidence bounds on the damage state probabilities or on the fragilities. For example, damage state probability histograms that are illustrated in Figures 8.7 to 8.9 for the three-, six-, and nine-story GLD RC frames, respectively, show the frequency diagrams from 1,000 bootstrap sets at 10%, 5%, and 2% PE in 50 yr earthquake hazard levels for Memphis, TN. These histograms can be used to estimate confidence bounds on the damage state probabilities. Confidence bounds on the fragilities are also useful in risk assessment and can be used to develop confidence bounds on the damage state probabilities for any earthquake hazard level. Figure 8.10 illustrates the 95% confidence bounds together with the median, and the lower and upper (prediction) bounds of the fragility estimates of all three frames.[d] Also illustrated in the figure are the 90th percentile fragilities that are commonly used in risk-informed decision-making [Wen and Ellingwood, 2005] and the lognormal probability distributions (*cf.* Eq. 5.3) that were fit to all fragility curves. Table 8.2 presents the parameters of lognormal distributions: the median ($\hat{S}_a$) and the logarithmic standard deviation (ζ), where the differences in the medians for the same limit states depict the epistemic uncertainty.

---

[d] All bounds were evaluated at each S_a increment of 0.01 g.
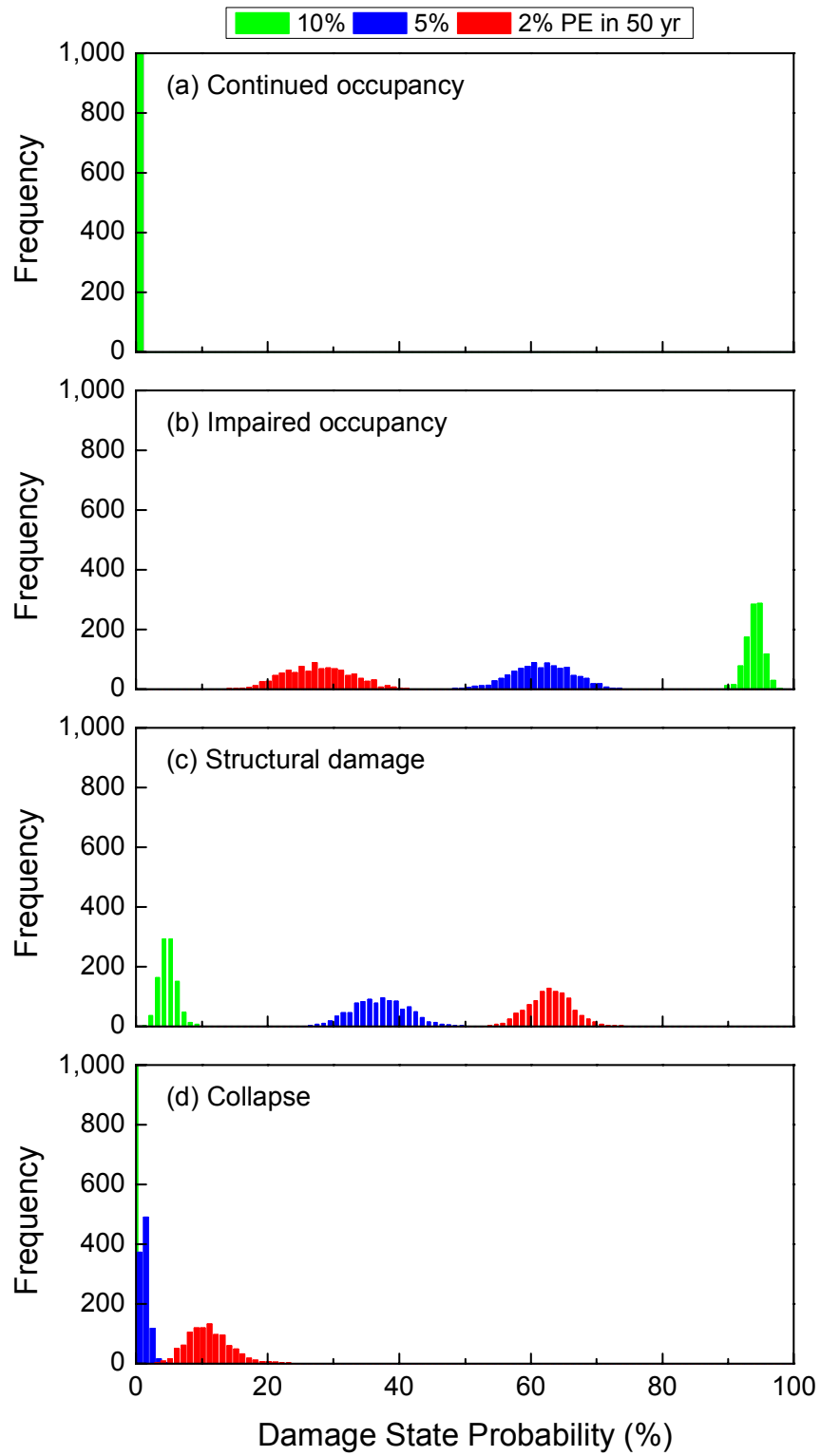
Figure 8.7 Damage state probability histograms for the three-story frame.
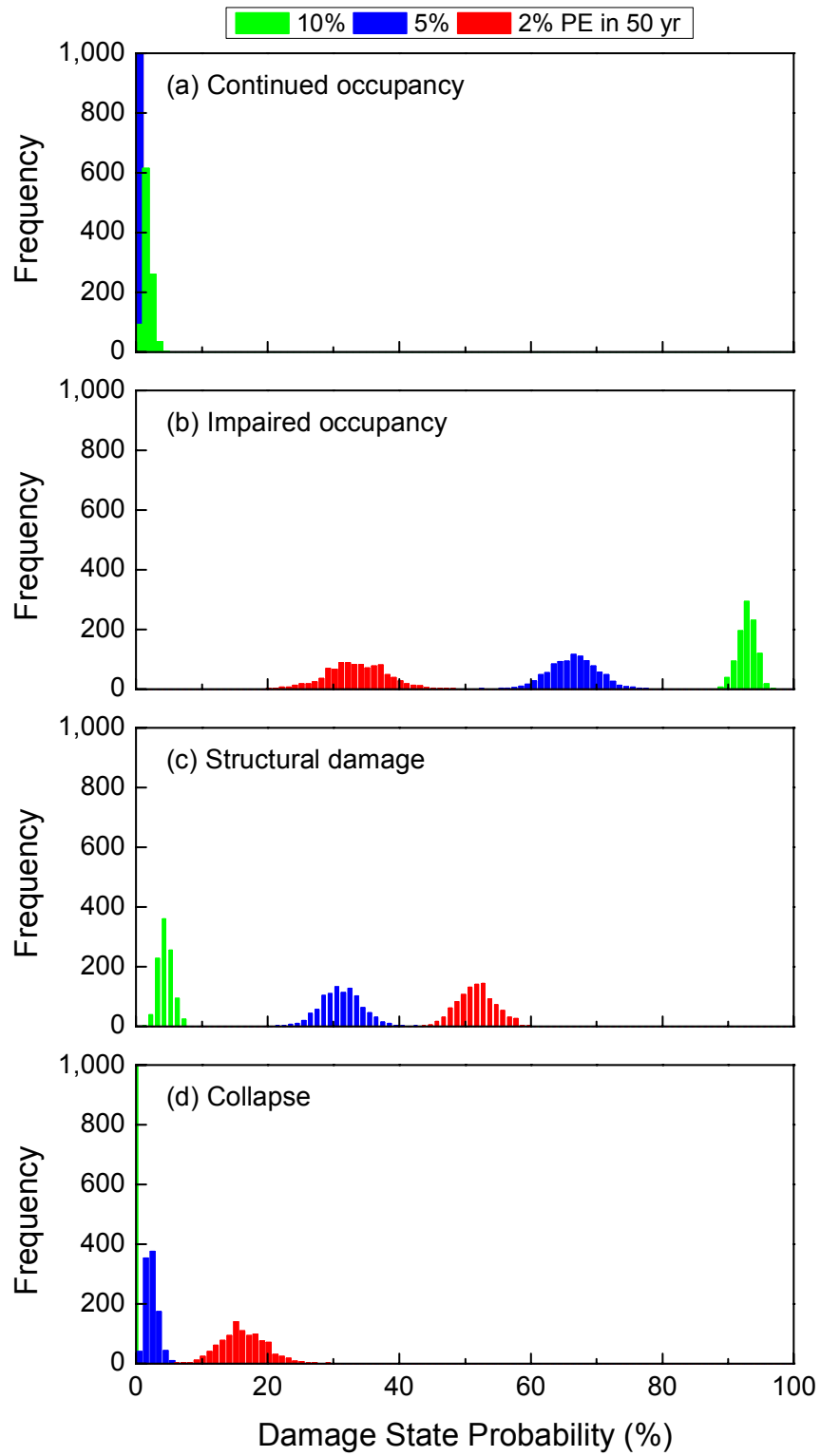
Figure 8.8 Damage state probability histograms for the six-story frame.
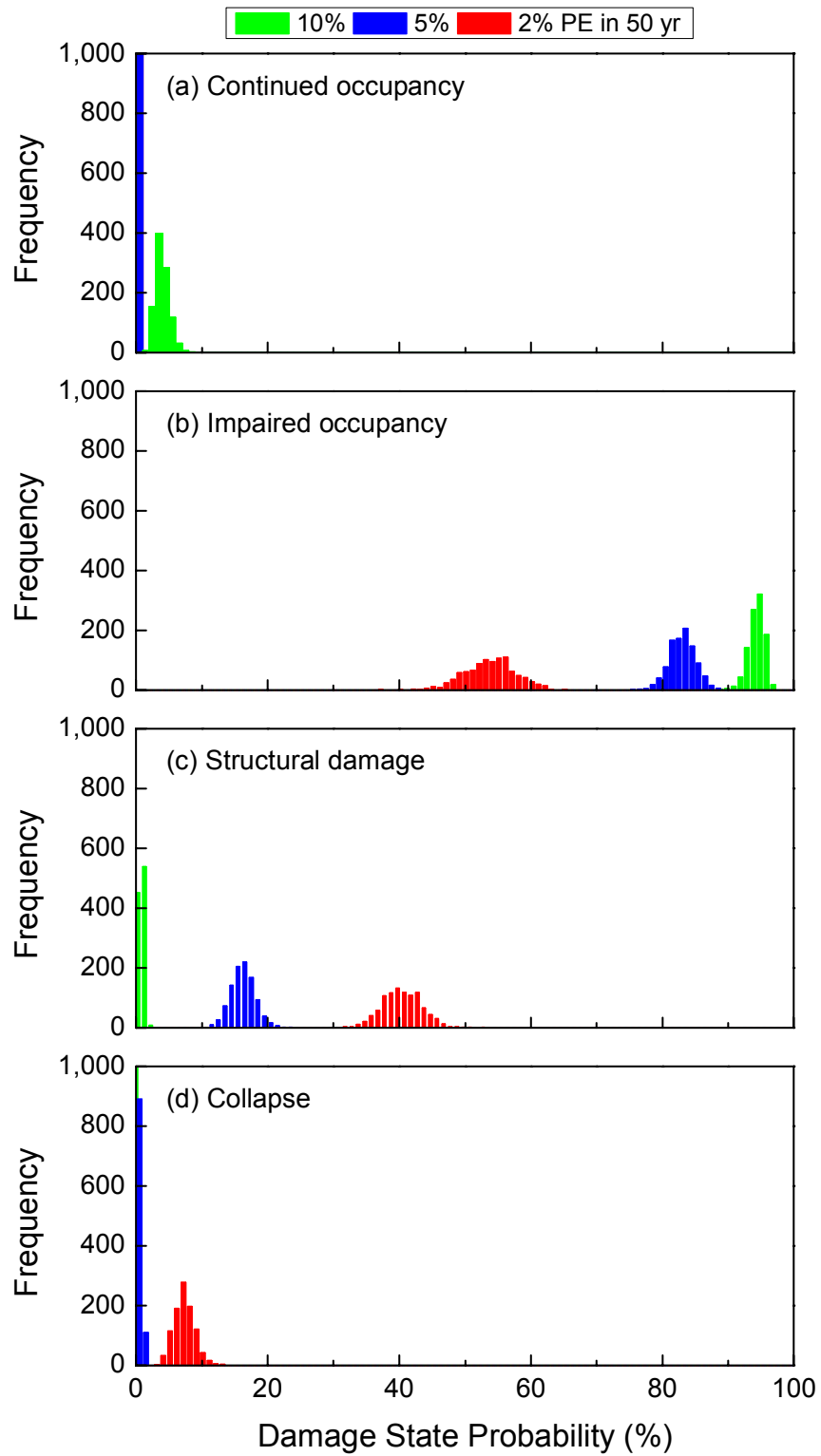
Figure 8.9 Damage state probability histograms for the nine-story frame.
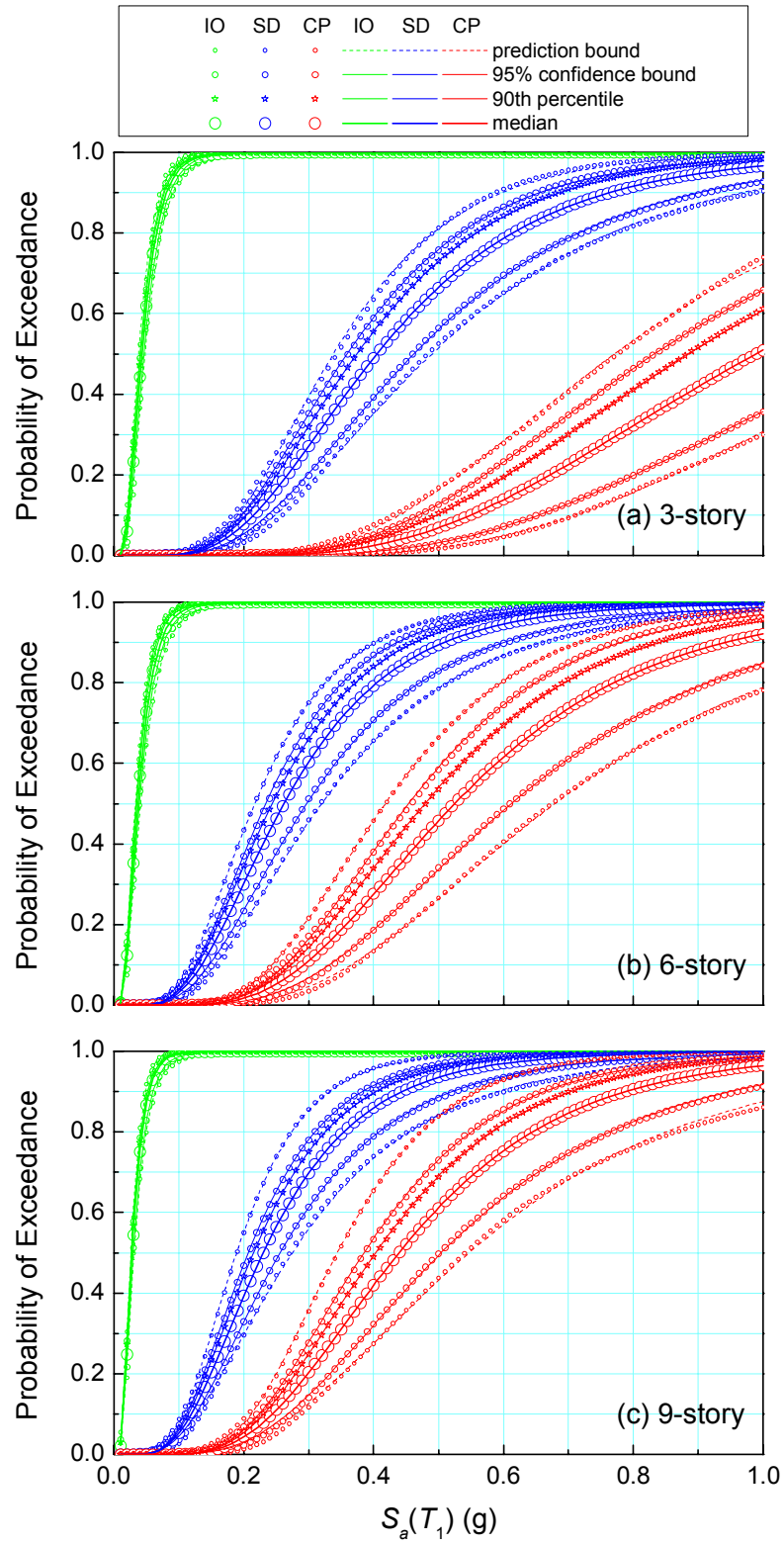
Figure 8.10 Confidence bounds on the seismic fragilities.

Table 8.2 Fragility parameters.

Percentile	$\hat{S}_a$ (g)			ζ		
	IO	SD	CP	IO	SD	CP
			3-story			
0%	0.048	0.490	1.250	0.495	0.531	0.442
2.5%	0.046	0.462	1.185	0.491	0.521	0.464
50%	0.043	0.405	0.989	0.494	0.494	0.459
90%	0.041	0.374	0.884	0.497	0.474	0.450
97.5%	0.040	0.359	0.833	0.498	0.470	0.448
100%	0.038	0.338	0.771	0.504	0.445	0.439
			6-story			
0%	0.041	0.320	0.679	0.556	0.562	0.484
2.5%	0.039	0.297	0.612	0.533	0.549	0.478
50%	0.037	0.262	0.525	0.518	0.518	0.456
90%	0.035	0.244	0.479	0.508	0.500	0.439
97.5%	0.034	0.234	0.454	0.504	0.485	0.423
100%	0.033	0.217	0.418	0.503	0.482	0.421
			9-story			
0%	0.031	0.275	0.547	0.559	0.597	0.525
2.5%	0.030	0.256	0.504	0.539	0.555	0.494
50%	0.028	0.230	0.439	0.512	0.513	0.457
90%	0.027	0.215	0.403	0.506	0.492	0.435
97.5%	0.027	0.207	0.385	0.503	0.480	0.424
100%	0.026	0.189	0.344	0.497	0.440	0.379

Table 8.3 Confidence statements.

	Performance-Based Design Objectives					
	Immediate Occupancy		Life Safety		Collapse Prevention	
	90%	95%	90%	95%	90%	95%
	confidence		confidence		confidence	
3-story	92%	91–97%	56%	52–70%	85%	82–95%
6-story	99%	99–100%	62%	59–74%	80%	77–91%
9-story	97%	96–99%	81%	79–87%	91%	90–96%

Confidence bounds on the seismic fragilities such as those in Figure 8.10 provide additional perspectives on decisions regarding pre- and post-earthquake planning. For example, the following confidence statements can be derived from Figure 8.10:

- With 90% confidence, the probabilities are 92%, 56%, and 85%, respectively, that the immediate occupancy, life safety, and collapse prevention performance-based design objectives in FEMA 450 (respectively associated with 50%, 5%, and 2% PE in 50 yr earthquake hazards in the CEUS — see Section 7.4.3) will be satisfied for the three-story GLD RC frame.

- With 95% confidence, the probabilities are 91–97%, 52–70%, and 82–95%, respectively, that the immediate occupancy, life safety, and collapse prevention design objectives will be satisfied.

Such confidence statements, which are tabulated in Table 8.3 for all the frames, provide a sense of the credibility that may be attached to the seismic fragilities based on analyses and databases comparable to those described in this dissertation.

8.6 Summary

The sensitivity of frame response statistics to the uncertainties in material and structural properties and modeling parameters was investigated at various levels of earthquake

hazard for Memphis, TN. Damping, concrete strength, and joint cracking strain were found to have the greatest impact on the response statistics. However, the uncertainty in ground motion dominated the overall uncertainty in structural response; this finding is consistent with the results of other studies [*e.g.*, Kwon and Elnashai, 2006].

Seismic fragilities that incorporate all sources of uncertainty considered above were derived and confidence bounds were developed on the fragilities. These fragilities and the associated confidence bounds provided alternative risk depictions for the seismic vulnerability of the RC frame inventory in Memphis, TN, which were based on the performance-based design objectives in FEMA 450.

CHAPTER 9

SUMMARY, CONCLUSIONS, AND FUTURE RESEARCH

9.1 Summary

The infrequent nature of earthquakes in the CEUS (Central and Eastern United States), and the fact that none with intensity comparable to the New Madrid sequence of 1811–12 or the Charleston earthquake of 1886 has occurred in the past century, have caused the earthquake hazard in the region to be neglected in most building design and construction. Only recently has there been an increased concern regarding the seismic performance of the built environment in the case of a repeat of such earthquakes. RC (reinforced concrete) frames in the CEUS, which have primarily been designed for gravity load effects, are expected to perform poorly when subjected to earthquakes that are judged, in recent seismological research, as being plausible in the NMSZ (New Madrid Seismic Zone). The objective of this study is to develop a set of probability-based tools for efficient uncertainty analysis and seismic vulnerability and risk assessment of such GLD (gravity load designed) RC frames and to use these tools in evaluating the vulnerability of RC frames that are representative of the building inventory in Memphis, TN — the largest population center close to the NMSZ in the CEUS.

Natural ground motion records in the relevant magnitude and distance ranges are practically non-existent in the CEUS. Hence, synthetic earthquake ground motions that are available from two different MAE (Mid-America Earthquake) Center projects were used in the finite element-based simulations for determining the seismic demand on the GLD RC frames by NTHA (nonlinear time history analysis).

154

GLD RC frames in the CEUS have limited lateral load resistance and are susceptible to column-sidesway or soft-story mechanisms under earthquake effects due to the non-ductile reinforcing details that are typical in this type of construction. Samples of such low-, mid-, and high-rise GLD RC frames designed using codes in use in the late 1980s were identified that represent the RC frame inventory in the CEUS compiled as part of the Memphis Test Bed project. Finite element structural models of these frames were developed using OpenSees, which facilitated the modeling of the non-ductile reinforcing details including those at the beam-column joints.

A beam-column joint model was developed to capture deficiencies in the joints of GLD RC frames, including excessive joint shear deformations and the inadequate joint shear capacity that result from a lack of transverse shear reinforcement within the joints, and the bond-slip due to insufficient beam bottom bar anchorage. The experimental determination of joint shear stress and strain formed the basis for the modeling approach. The envelope to the panel zone shear stress-strain relationship was defined through a quad-linear curve that replicates the experimental backbone, whereas the cyclic response was captured through a pinched hysteresis model. Bond-slip was taken into account through a reduced envelope describing the joint shear stress-strain relationship. This joint model was validated using experimental data from full-scale RC interior and exterior joint tests that lack earthquake-resistant details. The proposed beam-column joint model was incorporated in the finite element structural models of GLD RC frames, with the use of the formulation for defining the backbone of the panel zone for general configurations of GLD frame joints. Seismic demand analyses incorporating the proposed beam-column

joint model demonstrated the importance of modeling shear and bond-slip behavior in joints when assessing seismic performance of GLD RC frames.

Seismic fragility, which is defined as the probability of reaching stipulated damage states (performance levels) as a function of a specified measure of earthquake ground motion intensity, was formulated using the simulation-based reliability analysis in this study. The maximum interstory drift angle was selected as the structural demand measure (DM) due to its capability to provide insight about the potential for structural or local collapse, while the spectral acceleration at the fundamental period of the frame for 5% damping was adopted as the seismic intensity measure (IM), consistent with previous studies. The structural capacities are defined by the limit states (LSs) (defined in terms of interstory drift angle) that correspond to three widely used performance levels (immediate occupancy, life safety, and collapse prevention) in the earthquake community. The uncertainties in IM, DM, and LS were propagated through the fragility analysis.

Seismic fragilities were derived for low-, mid-, and high-rise GLD RC frames. The HAZUS fragilities for the same frames were also reproduced to provide additional perspective on fragility assessment of GLD RC frames in the CEUS. The fragilities in this study were developed using the Wen-Wu and Rix-Fernandez ground motions separately, where the differences displayed the impact of the choice of ground motion ensembles on seismic fragilities. These fragilities were used to evaluate the seismic vulnerability of the RC frame inventory in Memphis, TN, defined in terms of performance levels associated with reference earthquake hazard levels. This performance appraisal indicated that it is unlikely that the majority of existing GLD RC frames would

meet the life safety and collapse prevention performance objectives that are found in recent building codes and guidelines for performance-based earthquake engineering.

The sensitivity of frame response statistics to the uncertainties in various material and structural properties and beam-column joint model parameters was examined through *tornado diagrams* at various levels of earthquake hazard for Memphis, TN. Structural damping, concrete strength, and joint cracking strain were found to have the greatest impact on the response statistics. The fragilities that were derived using LHS (Latin hypercube sampling) and incorporated all sources of uncertainty considered above indicated only slight differences from those that reflect solely the uncertainty in earthquake ground motion intensity, suggesting that seismic fragilities that are developed under the assumption that the structural strength and stiffness parameters are deterministic and equal to their median (or mean) values are sufficient for purposes of damage and loss estimation. Confidence bounds that were developed on the fragilities provide a sense of the uncertainty and credibility in damage probability estimated for decision- and policy-makers for use in prioritizing risk mitigation efforts and developing post-earthquake response and recovery strategies.

9.2 Conclusions

Probabilistic risk assessment of GLD RC frames for the earthquake hazard in the CEUS using the seismic fragilities developed for such low-, mid-, and high-rise RC frames, as summarized above, leads to the following conclusions:

- GLD RC frames are vulnerable to damage from joint shear failures (and excessive joint deformations), beam bottom bar anchorage failures, significant P-Δ effects

(due to the high flexibility of the frames), and weak column-strong beam effects leading to soft-story collapses under earthquake excitation.

- The beam-column joint model that is proposed for finite element simulations of GLD RC frames is accurate in simulating the shear and bond-slip behavior in the joints of GLD frames, as the extensive comparisons with the experimental responses of such joints indicated. Such highly pinched experimental responses cannot be predicted by the conventional rigid joint assumption in the finite element structural models.

- Alternate ground motion models lead to accelerograms with frequency contents that are quite different, and these differences are a manifestation of epistemic uncertainty in the selection of the ground motion model. Significantly higher nonlinear structural responses at similar ground motion intensity levels were obtained from ground motions with high spectral intensities at longer periods, where the fundamental periods of flexible GLD RC frames fall. Hence, the choice of ground motion ensemble for seismic fragility assessment is important, especially in the case of flexible structures such as those present in the RC inventory in the CEUS. The ground motions utilized should reflect the seismo-tectonic features and the site conditions of the region of interest.

- Simple stochastic models of demand are sufficient to develop seismic fragilities.

- HAZUS fragilities are not appropriate for individual building assessment; they were found to be quite conservative.

- Frame response statistics were found to be sensitive to structural damping, concrete strength, and joint cracking strain. However, the uncertainty in ground motion is the factor that dominates uncertainties in fragility assessment.

- Confidence bounds on the seismic fragilities provide a sense of credibility for risk-informed decision making in prioritizing risk mitigation efforts and developing post-earthquake response and recovery strategies for communities in this area of the country.

- Existing GLD RC frames such as those considered in this study, which are typical of traditional design practices in the CEUS, are unlikely to meet the life safety and collapse prevention performance objectives found in recent building codes and guidelines for performance-based earthquake engineering.

9.3 Future Research

This study can be extended in the following areas:

- Three-dimensional effects and the presence of masonry infill walls should be incorporated in the finite element structural models of the frames, and their impact on seismic response of GLD RC frames should be assessed.

- Seismic fragilities should be derived for sample GLD RC frames with different number of bays and stories, and the significance of using a larger set of relatively more appropriate fragilities in vulnerability assessment of the RC inventory in the CEUS should be examined.

- The contribution of non-structural components to building performance was not considered in this study. Fragilities for non-structural components in a building should be developed to improve estimates of economic loss. These fragilities can

be derived from the already determined floor acceleration data for the low-, mid-, and high-rise GLD RC frames.

- A new seismic intensity measure that is representative of the frequency content of the ground motion and also the inelastic period of the structure should be developed. This measure should allow for period lengthening due to structural deterioration, and may reduce the differences in fragilities derived using different ground motion ensembles.

- Cost-benefit analysis should be performed first for deciding on whether or not to retrofit certain GLD RC frames in the CEUS. If retrofit appears to be feasible or cost-effective, the effectiveness of alternate strategies for classes of buildings can be judged using fragility assessments of the type described herein.

APPENDIX A

MOMENT-ROTATION RELATIONSHIP OF THE BEAM-COLUMN

JOINT PANEL ZONE

Table A.1 Formulations to convert joint shear stress into moment transferred through rotational spring.

Joint Model	Interior and Exterior Joints	Interior and Exterior Top Floor Joints
Scissors model with and without rigid end zones	$M_j = \tau_{jh} A_{jh} \dfrac{1}{\lambda}$ *	$M_j = \tau_{jh} A_{jh} \dfrac{1}{\lambda'}$ *
Joint2D[†]	$M_j = \tau_{jh} A_{jh} \dfrac{\eta}{\lambda}$ *	$M_j = \tau_{jh} A_{jh} \dfrac{\eta}{\lambda'}$ *

* $\lambda = \dfrac{1 - b_j / L_b}{jd} - \dfrac{1}{L_c}$, $\lambda = \dfrac{1 - b_j / L_b}{jd} - \dfrac{2}{L_c}$, $\eta = 1 - h_j / L_c - b_j / L_b$, where h_j is the height of the joint panel.

[†] The constraint equations that relate the external DOFs to the internal DOFs of the joint element based on the initial un-deformed configuration were utilized to derive the formulations.

APPENDIX B

OPENSEES PARAMETERS USED IN THE VALIDATION OF THE

BEAM-COLUMN JOINT MODEL

Table B.1 Concrete model parameters for the Walker [2001] specimens (1 MPa = 145 psi).

Specimen	Section	fpc^* (MPa)	$epsc0^*$	$fpcu^*$ (MPa)	$epsU^*$
	cover	-31.8	-0.002	0	-0.0048
PEER-14	beam core	-43.3	-0.0027	-8.7	-0.044
	column core	-45.9	-0.0029	-9.2	-0.053
	cover	-29.8	-0.002	0	-0.0050
CD15-14	beam core	-41.3	-0.0028	-8.3	-0.044
	column core	-43.9	-0.0029	-8.8	-0.053
	cover	-42.5	-0.002	0	-0.0039
CD30-14	beam core	-54.0	-0.0025	-10.8	-0.043
	column core	-56.6	-0.0027	-11.3	-0.053
	cover	-42.9	-0.002	0	-0.0039
PADH-14	beam core	-54.4	-0.0025	-10.9	-0.043
	column core	-57.0	-0.0027	-11.4	-0.052
	cover	-38.4	-0.002	0	-0.0042
PEER-22	beam core	-49.9	-0.0026	-10.0	-0.043
	column core	-52.5	-0.0027	-10.5	-0.053
	cover	-38.1	-0.002	0	-0.0042
CD30-22	beam core	-49.6	-0.0026	-9.9	-0.043
	column core	-52.2	-0.0027	-10.4	-0.053
	cover	-36.3	-0.002	0	-0.0043
PADH-22	beam core	-47.8	-0.0026	-9.6	-0.044
	column core	-50.4	-0.0028	-10.1	-0.053

* fpc is the concrete compressive strength, $epsc0$ is the concrete strain at maximum strength, $fpcu$ is the concrete crushing strength, and $epsU$ is the concrete strain at crushing strength. Note that compressive parameters are input as negative values.

Table B.2 Steel model parameters for the Walker [2001] specimens (1 in.^{2} = 645 mm^2, 1 MPa = 145 psi).

Bar	Area (mm^2)	f_y^* (MPa)	f_u^* (MPa)	ε_u^*	$\kappa^{*\dagger}$
Red #4	116	662	957	0.12	0.013
Red #5	200	503	820	0.08	0.020
Red #6	297	427	685	0.11	0.012
Red #7	394	423	696	0.12	0.012
Red #8	432	545	855	0.12	0.013
Green #7	348	516	800	0.12	0.012
Green #9	561	510	836	0.12	0.014
Silver #7	335	527	878	0.12	0.015
Silver #8	432	514	843	0.12	0.014
Silver #9	516	538	908	0.12	0.016

* f_y is the yield strength, f_u is the ultimate strength, ε_u is the ultimate strain, and κ is the strain hardening ratio; of the steel.

† $\kappa \cong \left[\left(f_u - f_y \right) / \left(\varepsilon_u - f_y / E \right) \right] / E$, where E (= 200,000 MPa) is the modulus of elasticity for steel.

Table B.3 Concrete model parameters for the Pantelides *et al.* [2002] specimens (1 MPa = 145 psi).

Specimen	Section*	fpc (MPa)	epsc0	fpcu (MPa)	epsU
	cover	-33.1	-0.002	0	-0.0046
	beam core (3 in.)	-40.6	-0.0025	-8.1	-0.048
Test Unit #1	column core (3 in.)	-41.1	-0.0025	-8.2	-0.050
	beam core (6 in.)	-36.9	-0.0022	-7.4	-0.019
	column core (6 in.)	-37.1	-0.0022	-7.4	-0.020
	cover	-30.2	-0.002	0	-0.0050
	beam core (3 in.)	-37.7	-0.0025	-7.5	-0.048
Test Unit #2	column core (3 in.)	-38.2	-0.0025	-7.6	-0.051
	beam core (6 in.)	-34.0	-0.0022	-6.8	-0.020
	column core (6 in.)	-34.2	-0.0023	-6.8	-0.021
	cover	-34.0	-0.002	0	-0.0045
	beam core (3 in.)	-41.5	-0.0024	-8.3	-0.048
Test Unit #3	column core (3 in.)	-42.0	-0.0025	-8.4	-0.050
	beam core (6 in.)	-37.8	-0.0022	-7.6	-0.019
	column core (6 in.)	-38.0	-0.0022	-7.6	-0.020
	cover	-31.6	-0.002	0	-0.0048
	beam core (3 in.)	-39.1	-0.0025	-7.8	-0.048
Test Unit #4	column core (3 in.)	-39.6	-0.0025	-7.9	-0.051
	beam core (6 in.)	-35.4	-0.0022	-7.1	-0.020
	column core (6 in.)	-35.6	-0.0023	-7.1	-0.021

* Spacing of the transverse shear reinforcement is indicated in parenthesis (3 in. = 76 mm; 6 in. = 150 mm).

Table B.4 Steel model parameters for the Pantelides *et al.* [2002] specimens (1 MPa = 145 psi).

Bar	Area (mm^2)	f_y (MPa)	f_u (MPa)	ε_u^*	κ
beam	641	459	761	0.12	0.013
column	507	470	742	0.12	0.012
ties	71	427	654	0.12	0.010

* The ultimate strain of the steel was assumed to be 0.12.

Table B.5 Joint shear stress and strain data used in defining the backbone of the panel zone for the Walker [2001] specimens.

Specimen	Damage State	$\dfrac{\bar{\tau}_{jh}^*}{\sqrt{\text{MPa}}}$ $\left(\sqrt{\text{psi}}\right)$	γ_j 10^{-3} rad
PEER-14	joint cracking	0.46 (5.6)	0.46
	beam yielding	0.72 (8.7)	3.4
	concrete spalling	0.85 (10.2)	22
	20% strength reduction	0.59 (7.1)	80†
CD15-14	joint cracking	0.42 (5.0)	0.26
	beam yielding	0.80 (9.6)	3.3
	concrete spalling	0.72 (8.7)	9.9
	20% strength reduction	0.69 (8.3)	76
CD30-14	joint cracking	0.34 (4.1)	0.25
	beam yielding	0.72 (8.7)	4.1
	concrete spalling	0.84 (10.1)	12
	20% strength reduction	0.59 (7.1)	60
PADH-14	joint cracking	0.42 (5.1)	0.31
	beam yielding	0.72 (8.7)	3.5
	concrete spalling	0.79 (9.5)	10†
	20% strength reduction	0.42 (5.1)	42
PEER-22	joint cracking	0.43 (5.2)	1.3
	beam yielding	0.81 (9.7)	6.3
	concrete spalling	1.10 (13.2)	17
	20% strength reduction	0.79 (9.5)	50
CD30-22	joint cracking	0.37 (4.4)	0.34
	beam yielding	1.16 (14.0)	5.6
	concrete spalling	1.23 (14.8)	18
	20% strength reduction	0.63 (7.6)	71
PADH-22	joint cracking	0.33 (4.0)	0.37
	beam yielding	1.17 (14.1)	6.0
	concrete spalling	1.14 (13.7)	20
	20% strength reduction	0.83 (10.0)	74

* *cf.* Eq. 6.5a.
† The value was assumed due to the lack of data.

Table B.6 Joint shear stress and strain data used in defining the backbone of the panel zone for the Pantelides *et al.* [2002] specimens.

Specimen	Positive Envelope $\bar{\tau}_{jh}^{*}$ $\sqrt{\text{MPa}}$ $\left(\sqrt{\text{psi}}\right)$		Positive Envelope γ_j $10^{-3}\,\text{rad}$	Negative Envelope $\bar{\tau}_{jh}^{*}$ $\sqrt{\text{MPa}}$ $\left(\sqrt{\text{psi}}\right)$		Negative Envelope γ_j $10^{-3}\,\text{rad}$
Test Unit #1	0.32	(3.8)	0.385	0.48	(5.8)	0.455
	0.38	(4.6)	0.824	0.73	(8.8)	1.12
	0.43	(5.2)	3.52	0.91	(10.9)	1.96
	0.12	(1.5)	80[†]	0.28	(3.4)	80[†]
Test Unit #2	0.54	(6.5)	0.4[†]	0.71	(8.5)	0.3[†]
	0.56	(6.8)[†]	0.8[†]	0.75	(9.0)[†]	0.8[†]
	0.58	(7.0)	4[†]	0.88	(10.6)	3[†]
	0.16	(1.9)	80[†]	0.17	(2.0)	80[†]
Test Unit #3	0.27	(3.2)	0.141	0.22	(2.6)	0.239
	0.42	(5.1)	0.272	0.52	(6.3)	0.948
	0.86	(10.4)	3.28	0.85	(10.2)	4.29
	0.22	(2.7)	80[†]	0.13	(1.6)	80[†]
Test Unit #4	0.39	(4.7)	0.329	0.42	(5.1)	0.326
	0.67	(8.1)	0.816	0.71	(8.6)	0.765
	0.92	(11.1)	3.13	0.97	(11.7)	2.25
	0.62	(7.5)	80[†]	0.48	(5.8)	80[†]

[*] *cf.* Eq. 6.5a.
[†] The value was assumed due to the lack of data.

APPENDIX C

COMPARISONS OF PREDICTIONS WITH EXPERIMENTAL

BEAM-COLUMN JOINT RESPONSES

Figure C.1 Comparisons of the simulated force-drift responses with the experimental response for the Walker [2001] Specimen CD15-14.
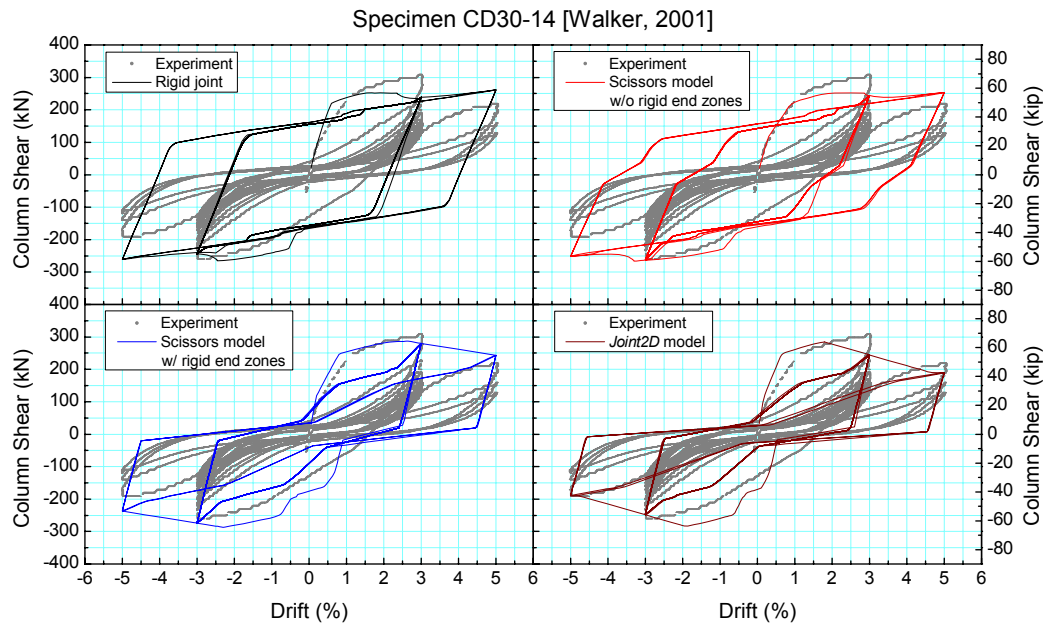
Figure C.2 Comparisons of the simulated force-drift responses with the experimental response for the Walker [2001] Specimen CD30-14.

Figure C.3 Comparisons of the simulated force-drift responses with the experimental response for the Walker [2001] Specimen PADH-14.
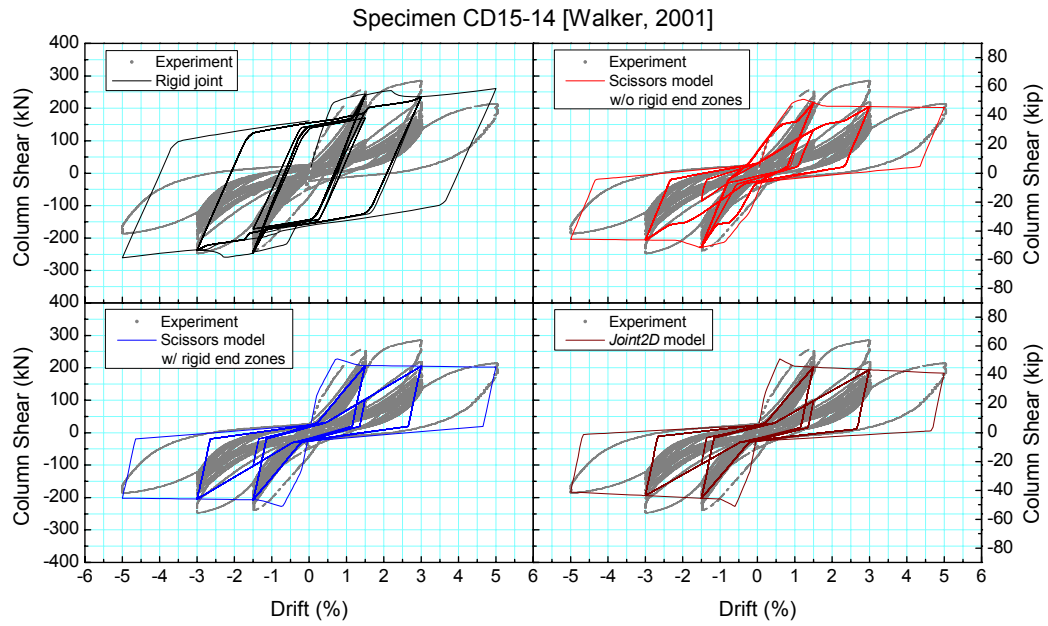
167
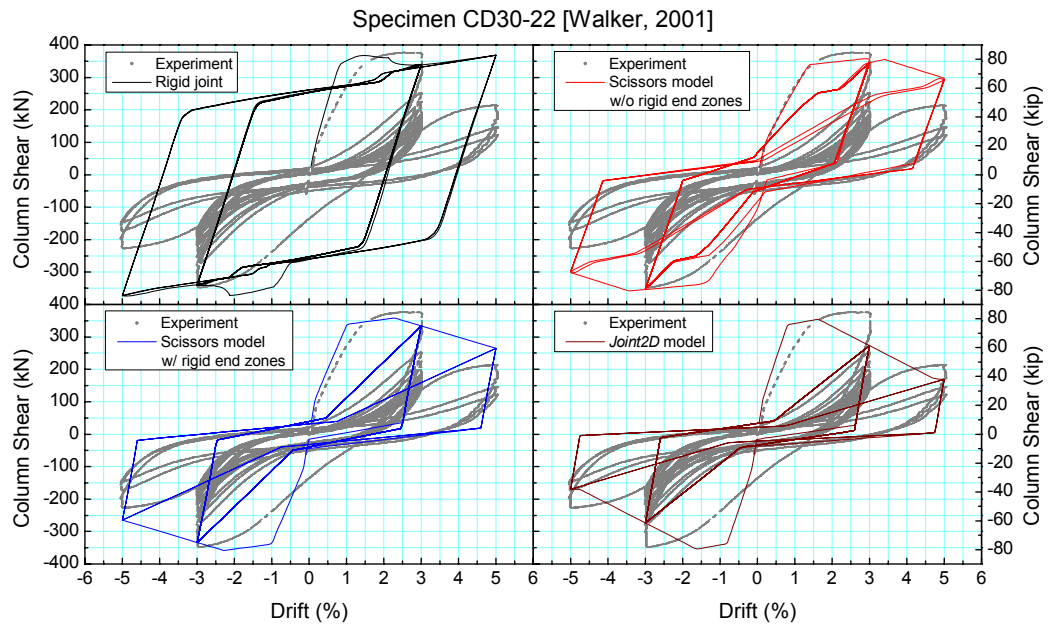
Figure C.4 Comparisons of the simulated force-drift responses with the experimental response for the Walker [2001] Specimen CD30-22.

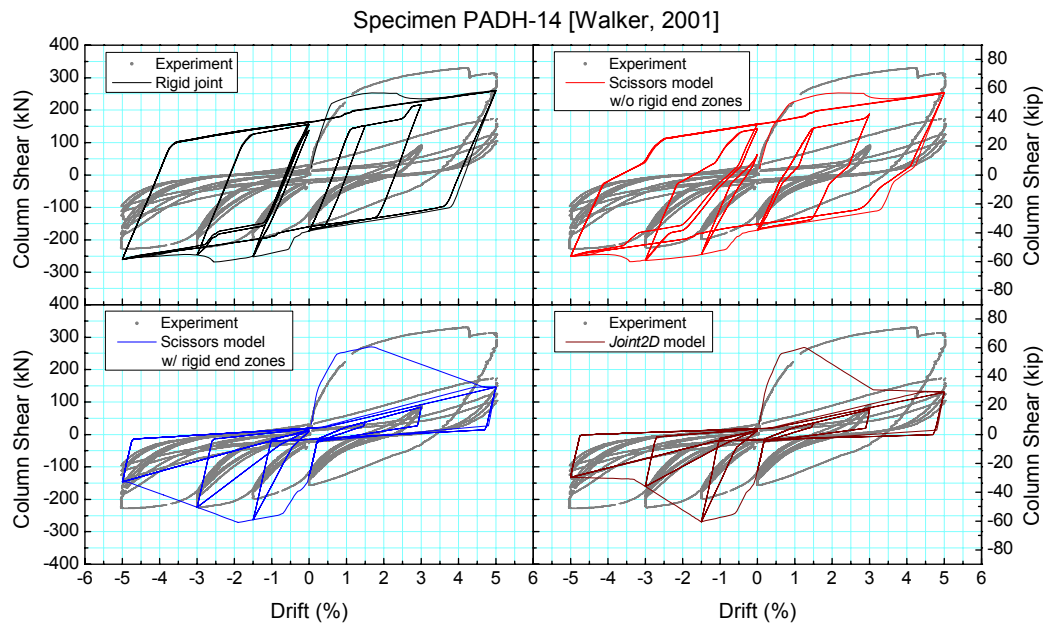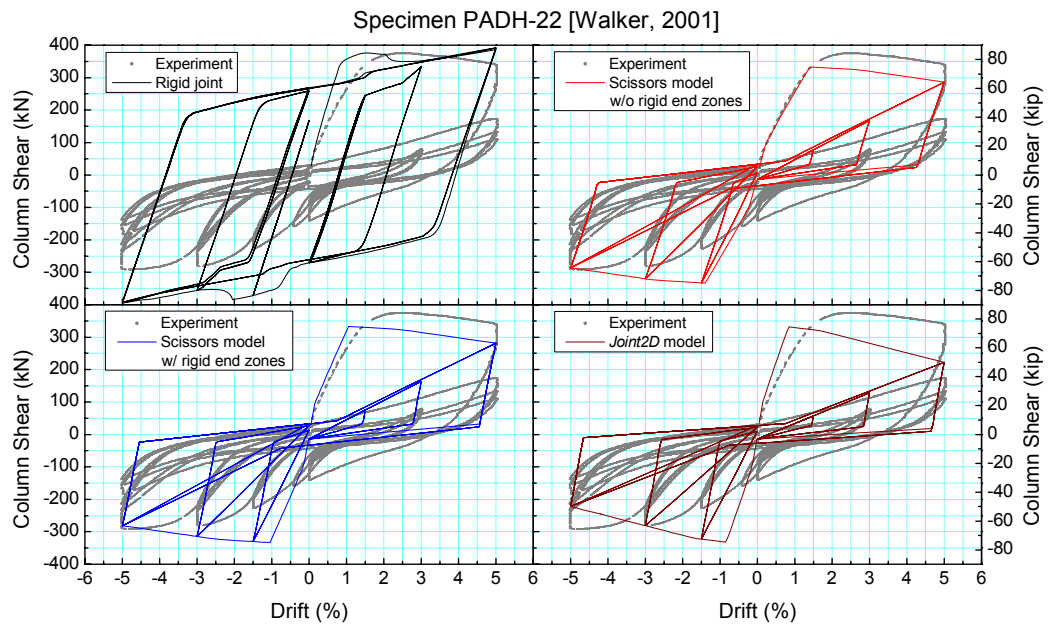**Figure C.5** Comparisons of the simulated force-drift responses with the experimental response for the Walker [2001] Specimen PADH-22.
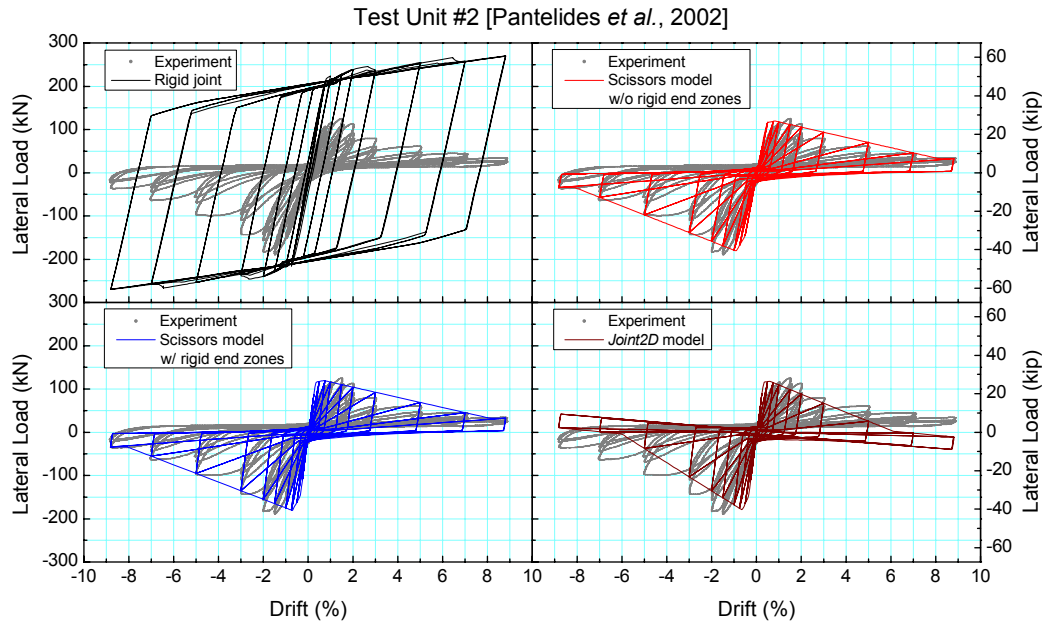
Figure C.6 Comparisons of the simulated force-drift responses with the experimental response for the Pantelides *et al.* [2002] Test Unit #2.
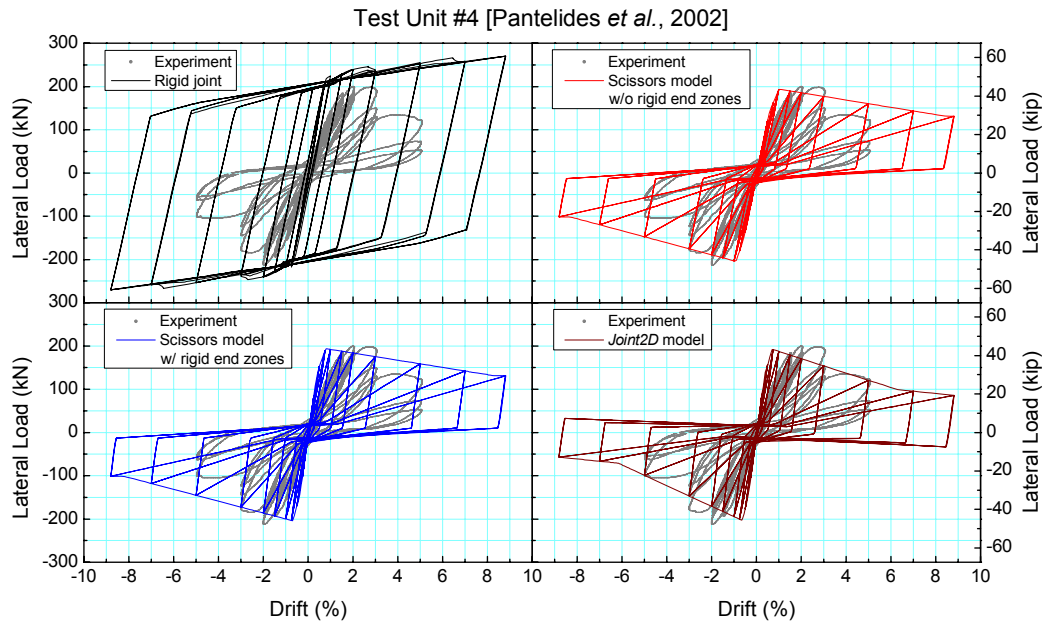
Figure C.7 Comparisons of the simulated force-drift responses with the experimental response for the Pantelides *et al.* [2002] Test Unit #4.

APPENDIX D

DEFINING THE BACKBONE OF THE BEAM-COLUMN JOINT

PANEL ZONE

The moments transferred through the joint (*i.e.*, the rotational spring) when the adjoining beams/columns reach their yield and ultimate capacities are given below for the scissors models:

$$\left(M_j^{+,-}\right)^{y,u} = \min\left[\frac{\left(M_C^B\right)^{y,u} + \left(M_C^T\right)^{y,u}}{\eta_C}, \frac{\alpha\left(M_{IB}^+\right)^y + \left(M_{IB}^-\right)^{y,u}}{\eta_B}\right] \tag{D.1}$$

for interior joints, and

$$\left(M_j^+\right)^{y,u} = \min\left[\frac{\left(M_C^B\right)^{y,u} + \left(M_C^T\right)^{y,u}}{\eta_C}, \frac{\alpha\left(M_{EB}^+\right)^y}{\eta_B}\right] \tag{D.2}$$

for the positive backbone, and

$$\left(M_j^-\right)^{y,u} = \min\left[\frac{\left(M_C^B\right)^{y,u} + \left(M_C^T\right)^{y,u}}{\eta_C}, \frac{\left(M_{EB}^-\right)^{y,u}}{\eta_B}\right] \tag{D.3}$$

for the negative backbone of exterior joints, where $\eta_C = 1 - h_j/L_c$ and $\eta_B = 1 - b_j/L_b$ (subscripts *C*, *IB*, and *EB* refer to column, interior beam, and exterior beam; and superscripts *y* and *u* refer to yield and ultimate, and *B* and *T* refer to bottom and top, respectively).

REFERENCES

Abrams DP [2002] "Consequence-based engineering approaches for reducing loss in Mid-America," *Linbeck Distinguished Lecture Series in Earthquake Engineering: Challenges for the New Millennium*, University of Notre Dame, Notre Dame, IN.

ACI Committee 318 [1989] *Building Code Requirements for Reinforced Concrete (ACI 318-89) and Commentary (ACI 318R-89)*, American Concrete Institute, Detroit, MI.

ACI Committee 318 [1999] *Building Code Requirements for Structural Concrete (318-99) and Commentary (318R-99)*, American Concrete Institute, Farmington Hills, MI.

ACI Committee 318 [2002] *Building Code Requirements for Structural Concrete (ACI 318-02) and Commentary (ACI 318R-02)*, American Concrete Institute, Farmington Hills, MI.

ACI Committee 318 [2005] *Building Code Requirements for Structural Concrete (ACI 318-05) and Commentary (ACI 318R-05)*, American Concrete Institute, Farmington Hills, MI.

ACI-ASCE Committee 352 [1991] *Recommendations for Design of Beam-Column Joints in Monolithic Reinforced Concrete Structures (ACI 352R-91)*, American Concrete Institute, Farmington Hills, MI.

Alath S, Kunnath SK [1995] "Modeling inelastic shear deformations in RC beam-column joints," in *Engineering Mechanics: Proceedings of Tenth Conference, May 21–24*, University of Colorado at Boulder, Boulder, CO, ed. Sture S, ASCE, New York, Vol. 2, pp. 822–825.

Alire DA [2002] "Seismic evaluation of existing unconfined reinforced concrete beam-column joints," M.Sc. Thesis, Department of Civil and Environmental Engineering, University of Washington, Seattle, WA.

Altoontash A [2004] "Simulation and damage models for performance assessment of reinforced concrete beam-column joints," Ph.D. Dissertation, Department of Civil and Environmental Engineering, Stanford University, Stanford, CA.

Arias A [1970] "A measure of earthquake intensity," in *Seismic Design for Nuclear Power Plants*, ed. Hansen RJ, MIT Press, Cambridge, MA, pp. 438–483.

Aslani H, Miranda E [2005] "Probability-based seismic response analysis," *Engineering Structures* **27**(8): 1151–1163.

ATC [1985] "Earthquake damage evaluation data for California," *Report ATC-13*, Applied Technology Council, Redwood City, CA.

Atkinson GM, Boore DM [1995] "Ground-motion relations for eastern North America," *Bulletin of the Seismological Society of America* **85**(1): 17–30.

Aycardi LE, Mander JB, Reinhorn AM [1992] "Seismic resistance of reinforced concrete frame structures designed only for gravity loads: Part II — Experimental performance of subassemblages," *Technical Report NCEER-92-0028*, National Center for Earthquake Engineering Research, State University of New York at Buffalo, Buffalo, NY.

Aycardi LE, Mander JB, Reinhorn AM [1994] "Seismic resistance of reinforced concrete frame structures designed only for gravity loads: Experimental performance of subassemblages," *ACI Structural Journal* **91**(5): 552–563.

Ayyub BM, Lai KL [1989] "Structural reliability assessment using Latin hypercube sampling," *Proceedings of the Fifth International Conference on Structural Safety and Reliability, August 7–11*, San Francisco, CA.

Baker JW, Cornell CA [2005] "A vector-valued ground motion intensity measure consisting of spectral acceleration and epsilon," *Earthquake Engineering and Structural Dynamics* **34**: 1193–1217.

Beres A, Pessiki SP, White RN, Gergerly P [1996] "Implications of experiments on the seismic behavior of gravity load designed RC beam-to-column connections," *Earthquake Spectra* (EERI) **12**(2): 185–198.

Beres A, White RN, Gergely P [1992] "Seismic behavior of reinforced concrete frame structures with nonductile details: Part I — Summary of experimental findings of full scale beam-column joint tests," *Technical Report NCEER-92-0024*, National Center for Earthquake Engineering Research, State University of New York at Buffalo, Buffalo, NY.

Bertero RD, Bertero VV [2002] "Performance-based seismic engineering: the need for a reliable conceptual comprehensive approach," *Earthquake Engineering and Structural Dynamics* **31**: 627–652.

Biddah A, Ghobarah A [1999] "Modelling of shear deformation and bond slip in reinforced concrete joints," *Structural Engineering and Mechanics* **7**(4): 413–432.

Boore DM [2003] "Simulation of ground motion using the stochastic method," *Pure and Applied Geophysics* **160**: 635–676.

Bracci JM, Reinhorn AM, Mander JB [1995] "Seismic resistance of reinforced concrete frame structures designed for gravity loads: Performance of structural system," *ACI Structural Journal* **92**(5): 597–609.

Celik OC, Ellingwood BR [2007] "Modeling beam-column joints in fragility assessment of gravity load designed reinforced concrete frames," *Journal of Earthquake Engineering*, in press.

Chandler AM, Lam NTK [2001] "Performance-based design in earthquake engineering: a multi-disciplinary review," *Engineering Structures* **23**(12): 1525–1543.

Chopra AK [1995] *Dynamics of Structures: Theory and Applications to Earthquake Engineering*, Prentice Hall, Upper Saddle River, NJ.

Conte JP, Pandit H, Stewart JP, Wallace JW [2003] "Ground motion intensity measures for performance-based earthquake engineering," *Proceedings of the Ninth International Conference on Applications of Statistics and Probability in Civil Engineering, 6–9 July*, San Francisco, CA.

Cordova PP, Deierlein GG, Mehanny SSF, Cornell CA [2000] "Development of a two-parameter seismic intensity measure and probabilistic assessment procedure," *The Second U.S.-Japan Workshop on Performance-Based Earthquake Engineering Methodology for Reinforced Concrete Building Structures, 11–13 September*, Sapporo, Japan.

Cornell CA [1968] "Engineering seismic risk analysis," *Bulletin of Seismological Society of America* **58**(5): 1583–1606.

Cornell CA, Jalayer F, Hamburger RO, Foutch DA [2002] "Probabilistic basis for 2000 SAC Federal Emergency Management Agency steel moment frame guidelines," *Journal of Structural Engineering* (ASCE) **128**(4): 526–533.

Efron B [1979] "Bootstrap methods: Another look at the jackknife," *The Annals of Statistics* **7**(1): 1–26.

El-Attar AG, White RN, Gergerly P [1997] "Behavior of gravity load designed reinforced concrete buildings subjected to earthquakes," *ACI Structural Journal* **94**(2): 133–145.

Elenas A, Meskouris K [2001] "Correlation study between seismic acceleration parameters and damage indices of structures," *Engineering Structures* **23**(6): 698–704.

Ellingwood B [1990] "Validation studies of seismic PRAs," *Nuclear Engineering and Design* **123**(2): 189–196.

Ellingwood B [1998] "Issues related to structural aging in probabilistic risk analysis of nuclear power plants," *Reliability Engineering and System Safety* **62**(3): 171–183.

Ellingwood BR, Celik OC, Kinali K [2007] "Fragility assessment of building structural systems in Mid-America," *Earthquake Engineering and Structural Dynamics* Special Issue on Seismic Reliability Analysis of Structures, in press.

Erberik MA, Elnashai AS [2003] "Seismic vulnerability of flat-slab structures," *Project DS-9 Technical Report*, Mid-America Earthquake Center, University of Illinois at Urbana-Champaign, Urbana, IL, http://mae.cee.uiuc.edu [31 July 2006].

Erberik MA, Elnashai AS [2004] "Fragility analysis of flat-slab structures," *Engineering Structures* **26**(7): 937–948.

Erberik MA, Elnashai AS [2006] "Loss estimation analysis of flat-slab structures," *Natural Hazards Review* (ASCE) **7**(1): 26–37.

FEMA [1997a/2000b] *NEHRP Guidelines for the Seismic Rehabilitation of Buildings (FEMA 273/356)*, Federal Emergency Management Agency, Washington, D.C.

FEMA [1997b] *NEHRP Recommended Provisions for Seismic Regulations for New Buildings and Other Structures and Commentary (FEMA 302/303)*, Federal Emergency Management Agency, Washington, D.C.

FEMA [2000a] *Recommended Seismic Design Criteria for New Steel Moment-Frame Buildings (FEMA 350)*, Federal Emergency Management Agency, Washington, D.C.

FEMA [2003a] *Multi-Hazard Loss Estimation Methodology, Earthquake Model, HAZUS-MH MR1 Technical Manual*, Federal Emergency Management Agency, Washington, D.C.

FEMA [2003b] *NEHRP Recommended Provisions for Seismic Regulations for New Buildings and Other Structures and Commentary (FEMA 450)*, Federal Emergency Management Agency, Washington, D.C.

Fernandez JA, Rix GJ [2006] "Soil attenuation relationships and seismic hazard analyses in the Upper Mississippi Embayment," *Proceedings of the Eighth U.S. National Conference on Earthquake Engineering, April 18–22*, San Francisco, CA.

Frankel AD, Mueller CS, Barnhard TP, Perkins DM, Leyendecker EV, Dickman N, Hanson SL, Hopper MG [1996] "National seismic-hazard maps: Documentation," *Open-File Report 96-532*, U.S. Geological Survey, Denver, CO.

Freeman SA [1998] "The capacity spectrum method as a tool for seismic design," *Proceedings of the Eleventh European Conference on Earthquake Engineering, September 6–11*, Paris, France.

French S, Olshansky R [2001] "Inventory of essential facilities in Mid-America," *Project SE-1 Final Report*, Mid-America Earthquake Center, University of Illinois at Urbana-Champaign, Urbana, IL, http://mae.cee.uiuc.edu [31 July 2006].

Ghobarah A, Biddah A [1999] "Dynamic analysis of reinforced concrete frames including joint shear deformation," *Engineering Structures* **21**(11): 971–987.

Giovenale P, Cornell CA, Esteva L [2004] "Comparing the adequacy of alternative ground motion intensity measures for the estimation of structural responses," *Earthquake Engineering and Structural Dynamics* **33**(8): 951–979.

Glaister S, Pinho R [2003] "Development of a simplified deformation-based method for seismic vulnerability assessment," *Journal of Earthquake Engineering* **7**(SI1): 107–140.

Gulkan P, Sozen M [1999] "Procedure for determining seismic vulnerability of building structures," *ACI Structural Journal* **96**(3): 336–342.

Hamburger RO [1997] "A framework for performance-based earthquake resistive design," *EERC-CUREe Symposium in Honor of Vitelmo V. Bertero, January 31–February 1*, Berkeley, CA.

Healey JJ, Wu ST, Murga M [1980] "Structural building response review," *NUREG/CR-1423, Vol. I*, U.S. Nuclear Regulatory Commission, Washington, D.C.

Hoffmann GW, Kunnath SK, Reinhorn AM, Mander JB [1992] "Gravity-load-designed reinforced concrete buildings: Seismic evaluation of existing construction and detailing strategies for improved seismic resistance," *Technical Report NCEER-92-0016*, National Center for Earthquake Engineering Research, State University of New York at Buffalo, Buffalo, NY.

Hsu TTC [1988] "Softened truss model theory for shear and torsion," *ACI Structural Journal* **85**(6): 624–634.

Kennedy RP, Ravindra MK [1984] "Seismic fragilities for nuclear power plant risk studies," *Nuclear Engineering and Design* **79**(1): 47–68.

Kircher CA, Nassar AA, Kustu O, Holmes WT [1997] "Development of building damage functions for earthquake loss estimation," *Earthquake Spectra* (EERI) **13**(4): 663–682.

Kircher CA, Reitherman RK, Whitman RV, Arnold C [1997] "Estimation of earthquake losses to buildings," *Earthquake Spectra* (EERI) **13**(4): 703–720.

Krawinkler H, Medina R, Alavi B [2003] "Seismic drift and ductility demands and their dependence on ground motions," *Engineering Structures* **25**(5): 637–653.

Kunnath SK, Hoffmann G, Reinhorn AM, Mander JB [1995a] "Gravity-load-designed reinforced concrete buildings — Part I: Seismic evaluation of existing construction," *ACI Structural Journal* **92**(3): 343–354.

Kunnath SK, Hoffmann G, Reinhorn AM, Mander JB [1995b] "Gravity load-designed reinforced concrete buildings — Part II: Evaluation of detailing enhancements," *ACI Structural Journal* **92**(4): 470–478.

Kurama YC, Farrow KT [2003] "Ground motion scaling methods for different site conditions and structure characteristics," *Earthquake Engineering and Structural Dynamics* **32**: 2425–2450.

Kurose Y, Guimaraes GN, Zuhua L, Kreger ME, Jirsa JO [1991] "Evaluation of slab-beam-column connections subjected to bidirectional loading," in *Design of Beam-Column Joints for Seismic Resistance*, Publication SP-123, ed. Jirsa JO, American Concrete Institute, Detroit, MI, pp. 39–67.

Kwon OS, Elnashai A [2006] "The effect of material and ground motion uncertainty on the seismic vulnerability of RC structure," *Engineering Structures* **28**(2): 289–303.

LaFave JM, Shin M [2005] "Discussion of 'Modeling reinforced-concrete beam-column joints subjected to cyclic loading,' by Lowes LN, Altoontash A," *Journal of Structural Engineering* (ASCE) **131**(6): 992–993.

Leon RT [1989] "Interior joints with variable anchorage lengths," *Journal of Structural Engineering* (ASCE) **115**(9): 2261–2275.

Leon RT [1990] "Shear strength and hysteretic behavior of interior beam-column joints," *ACI Structural Journal* **87**(1): 3–11.

Leyendecker EV, Hunt RJ, Frankel AD, Rukstales KS [2000] "Development of maximum considered earthquake ground motion maps," *Earthquake Spectra* (EERI) **16**(1): 21–40.

Lowes LN, Altoontash A [2003] "Modeling reinforced-concrete beam-column joints subjected to cyclic loading," *Journal of Structural Engineering* (ASCE) **129**(12): 1686–1697.

Lowes LN, Mitra N, Altoontash A [2004] "A beam-column joint model for simulating the earthquake response of reinforced concrete frames," *PEER 2003/10*, Pacific Earthquake Engineering Research Center, University of California, Berkeley, CA.

Luco N, Cornell CA [2007] "Structure-specific scalar intensity measures for near-source and ordinary earthquake ground motions," *Earthquake Spectra* (EERI) **23**(2): 357–392.

MacGregor JG, Mirza SA, Ellingwood BR [1983] "Statistical analysis of resistance of reinforced and prestressed concrete members," *Journal of the American Concrete Institute* **80**(3): 165–276.

McKay MD, Conover WJ, Beckman RJ [1979] "A comparison of three methods for selecting values of input variables in the analysis of output from a computer code," *Technometrics* **21**: 239–245.

McKenna F, Fenves GL [2006] *Open System for Earthquake Engineering Simulation (OpenSees) User Manual*, http://opensees.berkeley.edu [31 July 2006], University of California, Berkeley, CA.

Mitra N, Lowes LN [2004] "Evaluation and advancement of a reinforced concrete beam-column joint model," *Proceedings of the Thirteenth World Conference on Earthquake Engineering, August 1–6,* Vancouver, B.C., Canada, Paper No. 1001.

Mosalam KM, Ayala G, White RW, Roth C [1997] "Seismic fragility of LRC frames with and without masonry infill walls," *Journal of Earthquake Engineering* **1**(4): 693–720.

Olsson A, Sandberg G, Dahlblom O [2003] "On Latin hypercube sampling for structural reliability analysis," *Structural Safety* **25**(1): 47–68.

Pantelides CP, Hansen J, Nadauld J, Reaveley LD [2002] "Assessment of reinforced concrete building exterior joints with substandard details," *PEER 2002/18*, Pacific Earthquake Engineering Research Center, University of California, Berkeley, CA.

Park R, Priestley MJN, Gill WD [1982] "Ductility of square-confined concrete columns," *Journal of the Structural* Division (ASCE) **108**(ST4): 929–950.

Park Y, Ang AHS [1985] "Mechanistic seismic damage model for reinforced concrete," *Journal of Structural Engineering* (ASCE) **111**(4): 722–739.

Pessiki SP, Conley CH, Gergely P, White RN [1990] "Seismic behavior of lightly-reinforced concrete column and beam-column joint details," *Technical Report*

NCEER-90-0014, National Center for Earthquake Engineering Research, State University of New York at Buffalo, Buffalo, NY.

Porter KA, Beck JL, Shaikhutdinov RV [2002] "Sensitivity of building loss estimates to major uncertain variables," *Earthquake Spectra* (EERI) **18**(4): 719–743.

Porter KA, Kiremidjian AS, LeGrue JS [2001] "Assembly-based vulnerability of buildings and its use in performance evaluation," *Earthquake Spectra* (EERI) **17**(2): 291–312.

Ramamoorthy SK, Gardoni P, Bracci JM [2006] "Probabilistic demand models and fragility curves for reinforced concrete frames," *Journal of Structural Engineering* (ASCE) **132**(10): 1563–1572.

Rix GJ, Fernandez JA [2006] *Probabilistic Ground Motions for Selected Cities in the Upper Mississippi Embayment*, http://www.ce.gatech.edu/~geosys/soil_dynamics/ research/groundmotionsembay/ [31 July 2006], Georgia Institute of Technology, Atlanta, GA.

Rossetto T, Elnashai A [2005] "A new analytical procedure for the derivation of displacement-based vulnerability curves for populations of RC structures," *Engineering Structures* **27**(3): 397–409.

Rossetto T, Elnashai AS [2003] "Derivation of vulnerability functions for European-type RC structures based on observational data," *Engineering Structures* **25**(10): 1241–1263.

SEAOC [1995] "Vision 2000: Performance-based seismic engineering of buildings," Structural Engineers Association of California, Sacramento, CA.

Shin M, LaFave JM [2004] "Testing and modeling for cyclic joint shear deformations in RC beam-column connections," *Proceedings of the Thirteenth World Conference on Earthquake Engineering, August 1–6*, Vancouver, B.C., Canada, Paper No. 0301.

Shinozuka M, Feng MQ, Lee J, Naganuma T [2000] "Statistical analysis of fragility curves," *Journal of Engineering Mechanics* (ASCE) **126**(12): 1224–1231.

Shiohara H [2001] "New model for shear failure of RC interior beam-column connections," *Journal of Structural Engineering* (ASCE) **127**(2): 152–160.

Shome N, Cornell CA [1998] "Normalization and scaling accelerograms for nonlinear structural analysis," *Proceedings of the Sixth National Conference on Earthquake Engineering, May 31–June 4*, Seattle, WA.

Shome N, Cornell CA, Bazzurro P, Carballo JE [1998] "Earthquakes, records, and nonlinear responses," *Earthquake Spectra* (EERI) **14**(3): 469–500.

Silva W, Gregor N, Darragh R [2003] "Development of regional hard rock attenuation relations for Central and Eastern North America, Mid-Continent and Gulf Coast areas," Pacific Engineering and Analysis, El Cerrito, CA.

Singhal A, Kiremidjian AS [1996] "Method for probabilistic evaluation of seismic structural damage," *Journal of Structural Engineering* (ASCE) **122**(12): 1459–1467.

Singhal A, Kiremidjian AS [1998] "Bayesian updating of fragilities with application to RC frames," *Journal of Structural Engineering* (ASCE) **124**(8): 922–929.

Song J, Ellingwood BR [1999] "Probabilistic modeling of steel moment frames with welded connections," *Engineering Journal* (AISC) **36**(3): 129–137.

Stevens NJ, Uzumeri SM, Collins MP [1991] "Reinforced concrete subjected to reversed cyclic shear — Experiments and constitutive model," *ACI Structural Journal* **88**(2): 135–146.

USGS [2002a] "Earthquake hazard in the heart of the homeland," *USGS Fact Sheet FS-131-02*, U.S. Geological Survey.

USGS [2002b] *National & Regional Seismic Hazard Maps*, http://earthquake.usgs.gov/research/hazmaps/ [11 May 2007], U.S. Geological Survey.

USGS [2002c] *Interactive Deaggregations*, http://eqint.cr.usgs.gov/eq-men/html/deaggint2002-06.html [11 May 2007], U.S. Geological Survey.

USGS [2003] "The USGS earthquake hazards program in NEHRP—Investing in a safer future," *USGS Fact Sheet 017-03*, U.S. Geological Survey.

USGS [2007] *Largest Earthquakes in the United States*, http://earthquake.usgs.gov/ regional/states/10_largest_us.php [11 May 2007], U.S. Geological Survey.

Uzumeri SM [1977] "Strength and ductility of cast-in-place beam-column joints," in *Reinforced Concrete Structures in Seismic Zones*, Publication SP 53-12, American Concrete Institute, Detroit, MI, pp. 293–350.

Vamvatsikos D, Cornell CA [2002] "Incremental dynamic analysis," *Earthquake Engineering and Structural Dynamics* **31**(3): 491–514.

Vecchio FJ, Collins MP [1986] "The modified-compression field theory for reinforced-concrete elements subjected to shear," *Journal of the American Concrete Institute* **83**(2): 219–231.

Walker SG [2001] "Seismic performance of existing reinforced concrete beam-column joints," M.Sc. Thesis, Department of Civil and Environmental Engineering, University of Washington, Seattle, WA.

Wen YK, Ellingwood BR [2005] "The role of fragility assessment in consequence-based engineering," *Earthquake Spectra* (EERI) **21**(3): 861–877.

Wen YK, Ellingwood BR, Bracci J [2004] "Vulnerability function framework for consequence-based engineering," *Project DS-4 Report*, Mid-America Earthquake Center, University of Illinois at Urbana-Champaign, Urbana, IL, http://mae.cee .uiuc.edu [31 July 2006].

Wen YK, Ellingwood BR, Veneziano D, Bracci J [2003] "Uncertainty modeling in earthquake engineering (white paper)," *Project FD-2 Report*, Mid-America Earthquake Center, University of Illinois at Urbana-Champaign, Urbana, IL, http://mae.cee.uiuc.edu [31 July 2006].

Wen YK, Wu CL [2001] "Uniform hazard ground motions for Mid-America cities," *Earthquake Spectra* (EERI) **17**(2): 359–384.

Whitman RV, Anagnos T, Kircher CA, Lagorio HJ, Lawson RS, Schneider P [1997] "Development of a national earthquake loss estimation methodology," *Earthquake Spectra* (EERI) **13**(4): 643–661.

Williams MS, Sexsmith RG [1995] "Seismic damage indices for concrete structures: A state-of-the-art review." *Earthquake Spectra* (EERI) **11**(2): 319–349.

Youssef M, Ghobarah A [2001] "Modelling of RC beam-column joints and structural walls," *Journal of Earthquake Engineering* **5**(1): 93–111.

Yucemen MS, Ozcebe G, Pay AC [2004] "Prediction of potential damage due to severe earthquakes," *Structural Safety* **26**(3): 349–366.

VITA

Ozan Cem Celik was born on November 13, 1978 in Ankara, Turkey. He earned a B.S. degree in Civil Engineering and an M.S. degree in Structural Engineering from Middle East Technical University, Ankara, Turkey in 2000 and 2002, respectively. His M.S. thesis was on forced vibration testing of existing reinforced concrete buildings. He began pursuing a Ph.D. degree in Structural Engineering, Mechanics, and Materials at Georgia Institute of Technology in 2002, where his major concentration was in the area of earthquake engineering and seismic risk assessment of reinforced concrete buildings in the Central and Eastern United States, with a minor in Mathematical Methods of Reliability.